University of Liverpool

Department of Chemistry

Synthesis, Characterisation and Single Molecule Conductance Measurements of Organic Molecules

Thesis submitted in accordance with the requirements of the University of Liverpool for the degree of Doctor of Philosophy

By

Carly Brooke

2012

Abstract

The use of single molecules to construct electronic devices is an exciting prospect, and one that has long provided a driving force for research in the area of molecular scale electronics. In order for this emerging field to advance a deep understanding of the fundamental mechanisms that govern electron conduction at the molecular level is imperative. Recent developments in areas such as scanning tunnelling microscopy, have facilitated the determination of the electrical properties of single molecules tethered between two metallic contacts. The analysis and potentially tailoring of structure-property relationships is hugely important and could lead to new and unforeseen applications for this emerging field.

The work presented herein details two major studies. The first is an investigation of the transport properties of a series of analogous molecules, which consist of a single benzene ring sandwiched between two alkyl chains of varying length. Prior to the work in this thesis one such molecule, and various substituted analogues thereof, had shown behaviour similar to what would be expected of a molecular equivalent of a double tunnelling barrier. The data presented here demonstrates a remarkably low dependence of this system on molecular length; this result contradicts the behaviour expected of a coherent transport mechanism. Moreover, the study of the orbital energies and densities of these molecules provides further evidence of a mechanism of conduction that is very different to that previously suggested for this system.

The second study centres around the investigation of the conductance behaviour of 4,4'-bipyridine and some substituted analogues thereof; this study is presented in two parts. The first details attempts to synthesise planar analogues of 4,4'-bipyridine, as well the synthesis and reactivity of novel substituted bipyridines. The second part reports conductance data, electrochemical studies and theoretical calculations of properties of these molecules. The data presented provides new information regarding the relationship between electronic structure and conductance behaviour in this type of system.

Acknowledgements

Contents

Abbreviations

AFM	Atomic force microscope
BDA	1,4-Benzenediamine
BDMT	1,4-Benzenedimethanethiol
BDT	1,4-Benzenedithiol
BIPY	4,4'-Bipyridine
BJ	Break junction
Bn	Benzyl
^{n}BuLi	*n*-Butyllithium
^{t}BuLi	*tert*-Butyllithium
DBE	1,2-Dibromoethane
CV	Cyclic voltammtery
DCM	Dichloromethane
DFT	Density functional theory
DHP	Dihydropyran
DIAD	Di*iso*propylazodicarboxylate
DIPA	Di*iso*propylamine
DMAP	4-Dimethylaminopyridine
DMF	*N*, *N*-Dimethylformamide
DPPE	1,2-Bis(diphenylphosphino)ethane
EC STM	Electrochemical scanning tunnelling microscope
FTIR	Fourier transform infra red
HDT	Hexanedithiol
HMPA	Hexamethylphosphorotriamide
HOMO	Highest occupied molecular orbital
IC	Integrated circuit
I-V	Current-Voltage
LDA	Lithium di*iso*propylamine
LUMO	Lowest unoccupied molecular orbital
MBBIPY	*N,N*-Dimethyl-3,3',5,5'-tetrabromobipyridinium diiodide
MCBIPY	*N,N*-Dimethyl-3,3',5,5'-tetrachlorobipyridinium diiodide
NBS	*N*-Bromosuccinimide
NDR	Negative differential resistance
NDT	Nonanedithiol

ODT	Octanedithiol
OPE	Oligo(phenylene ethynylene)
OPI	Oligophenyleneimine
ONI	Oligonaphthalenefluoreneimine
Pd/C	Palladium on Carbon
PM-IRRAS	Polarisation modulation - infrared absorption spectroscopy
Ph	Phenyl
Pet. ether	Petroleum ether (40-60°C)
PPA	Polyphosphoric acid
PTTF	Pyrrolo-tetrathiafulvalene
QRE	Quasi reference electrode
SAM	Self assembled monolayer
SCE	Saturated calomel electrode
SMC	Single molecule conductance
STM	Scanning tunnelling microscope
STM BJ	Scanning tunnelling microscope Break Junction
TBAHFP	Tetrabutylammonium hexafluorophosphate
TBAI	Tetrabutylammonium iodide
TBBIPY	3,3',5,5'-Tetrabromo-4,4'-bipyridine
TBDPSCl	*tert*-Butyldiphenylsilylchloride
TCBIPY	3,3',5,5'-Tetrachloro-4,4'-bipyridine
TMBIPY	3,3',5,5'-Tetramethyl-4,4'-bipyridine
THF	Tetrahydrofuran
THP	Tetrahydropyran
TMS	Trimethylsilyl
TsCl	4-Toluenesulfonylchloride
UHV	Ultra high vacuum
V	Viologen
VL	Vacuum level
XPS	X-ray photoelectron spectroscopy
3Ph3	S,S'-(1,4-phenylenebis(propane-1,3-diyl))diethanethioate
4Ph4	S,S'-(1,4-phenylenebis(butane-1,4-diyl))diethanethioate
6Ph6	S,S'-(1,4-phenylenebis(hexane-1,6-diyl))diethanethioate
8Ph8	S,S'-(1,4-phenylenebis(octane-1,8-diyl))diethanethioate

Chapter 1

Introduction

1.1 General Introduction

The introduction of integrated circuits (ICs) in the mid-20th-century revolutionized the world of electronics. The first working example was demonstrated in 1958 by Jack Kilby, who would later win the 2000 Nobel Prize for his part in the invention. Early ICs contained only a few transistors per chip due to the large scale of the contemporary technology. In 1965 Dr. Gordon Moore published an article in *Electronics[1], in which he noted:

"The number of transistors that can be inexpensively placed on an integrated circuit is increasing exponentially, doubling approximately every two years"

He predicted that the trend would continue "for at least ten years". In fact his prediction held true for more than half a century, and is expected to continue until at least 2015. Each year chips become more and more powerful, and yet cheaper; in 2008 the well known Intel[©] Core[TM] 2 Duo processer contained 420 million transistors. In terms of size we are still a long way off the size of a single atom; this represents a fundamental barrier in the miniaturization of integrated circuits.

Modern day electronics commonly employs semiconductor devices fabricated in a "top down" approach. These devices exploit the properties of semiconducting materials in order to manipulate current flow. However, these properties may not necessarily hold true as sizes decrease to nanoscale dimensions. This has driven the development of a "bottom up" approach, in which molecular based materials have been investigated for use in electronic applications.

1.1.1 Nanotechnology and the Birth of Molecular Electronics

The field of nanotechnology was first alluded to in '*There's Plenty of Room at the Bottom'*, a now legendary lecture delivered in 1959 by Nobel laureate physicist Richard Feynman.[2] He considered the possibility of manipulating individual atoms and molecules using precise tools with nanometer precision. Whilst he did not use the phrase, this lecture created a vision of the field we now know as nanotechnology. Feynman's talk had little influence in the next few decades after its publication, perhaps due to the lack of the appropriate tools and technology to achieve such a feat. However, the invention of the scanning tunneling microscope in 1981 provided the first method of 'seeing' and 'manipulating' matter on the atomic scale, and changed the outlook for nanotechnology.

The potential development of electronic components consisting of organic molecules was first studied theoretically by Aviram and Ratner in 1974[3]. They noted that most common rectifiers are based on p-n type junctions. P-type semiconductors have an excess of positive charge carriers, whilst n-type semiconductors have an excess of negative charge carriers; p-n junctions are formed at the boundary of these two materials. It was envisaged that the use of substituents to increase and decrease π-electron density within an organic molecule could induce rectifier properties, in much the same way as a p-n type junction. The molecules studied consisted of a donor π-system and an acceptor π-system connected by a bridge, which serves to physically connect, but electronically decouple, the donor and acceptor systems. It was theoretically proposed that such a molecule would behave in an analogous fashion to a p-n junction. Whilst the calculations appeared to verify the potential use of single molecules in electronic devices, their idea was long considered a theoretical curiosity that could not be tested experimentally.
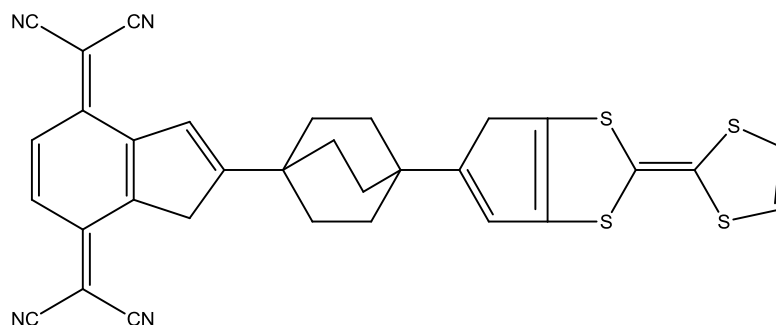
Figure 1.1 An example of a rectifier molecule.

The late 1990s finally saw what is believed to be the first transport experiment of a single molecule junction; a collaboration between the groups of Mark Reed and James Tour resulted in publication of the results of a study to determine the conductance through a single molecule of 1,4-benzenedithiol (BDT)[4], a breakthrough that is often considered to be the beginning of the field of single molecule conductance. Transport through BDT has since been studied extensively using a variety of methods.[5-8] The publication of this pioneering work made the realisation of electrical components consisting of single molecules seem a step closer, and resulted in an explosion of interest in the field of molecular electronics. Many techniques for determining the conductance of a single molecule have since been developed and utilised to probe electronic behavior at the single molecule level.[9]

It seems unlikely that silicon-based electronics will ever be entirely replaced by molecular electronics, rather the two technologies can be seen to complement each other. Molecular electronics could in principle offer advantages in terms of, for example, size, speed and synthetic tailorability. Moreover, molecular junctions provide an ideal system in which to investigate fundamental electron transport mechanisms, which play a key role in chemistry and biology.

In order for this emerging technology to move forwards, a deep understanding of the fundamental mechanisms that govern electron conduction at the molecular level is imperative. One of the principle challenges is the fabrication of reliable molecular junctions, although several techniques are now well established. The analysis and potentially tailoring of structure-property relationships is hugely important, and could lead to new and unforeseen applications for this emerging field.

1.2 Measuring the Conductance of a Single Molecule

The most commonly employed techniques involve trapping a single molecule between two metallic contacts, thus forming a metal-molecule-metal junction (Figure 1.2).[10]
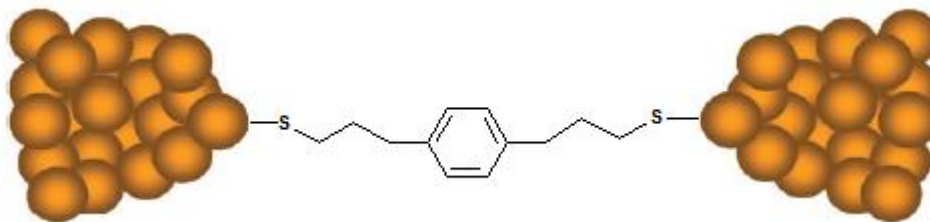
Figure 1.2 A metal-molecule-metal junction.

The single molecule conductance can then be determined by employing, most typically, a scanning tunnelling microscope (STM), atomic force microscope (AFM) or break junctions. Within this work, it is the use of an STM to determine the conductance of a single molecule that is of interest.

1.2.1 Scanning Tunnelling Microscope

The invention of the STM in 1981 provided the first atomic resolution images of solid surfaces;[11] the inventors, Gerd Binnig and Heinrich Rohrer, would later win the 1986 Nobel Prize in Physics for their design.

The STM is based on the quantum mechanical effect of tunnelling. The basic operation of an STM uses a conducting metal tip, which is brought to within a few angstroms of the sample being studied. When a voltage is applied between the two, electrons may be allowed to tunnel across the gap. The resulting tunnelling current is a function of the distance between the tip and substrate, and decays exponentially with increasing distance. The tip is scanned across the surface of the substrate whilst the current or tip height is monitored.

1.2.1.1 Quantum Tunnelling

Classical mechanics states that if a particle is incident upon a barrier, the energy of which is greater than the energy the particle has available to it, the particle will not

traverse the barrier. Quantum mechanics, however, predicts that the particle will not necessarily reflect, but will have some probability of tunnelling through the barrier.
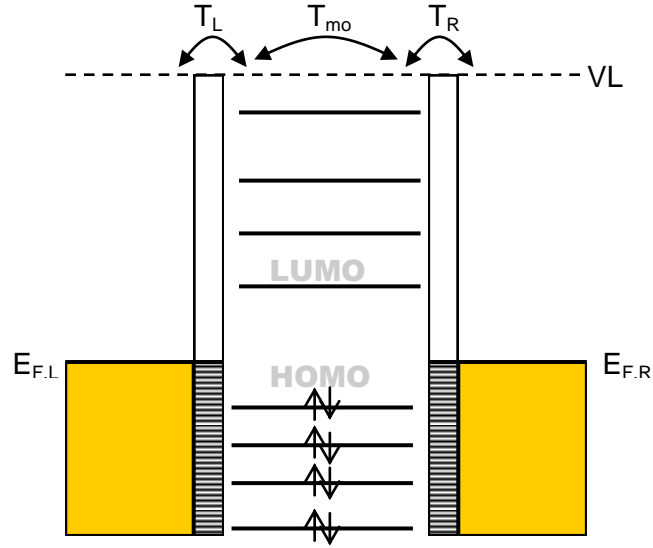
Figure 1.3 Schematic diagram of a metal/molecule/metal junction; T_L, T_R and T_{mol} are the transmission co-efficients of the left and right contacts and the molecule respectively; E_F is the Fermi energy and VL the vacuum level.

The tunnelling current though a metal/molecule/metal junction can be described using the Landauer formula for conductance[12]:

$$G = \frac{I}{V} = \frac{2e^2}{h}T_L T_{mol} T_R \qquad \textbf{1.1}$$

where I = current; V = applied bias; e = charge on one electron (1.602 x 10⁻¹⁹ C); h = Planck's Constant (6.626 x 10⁻¹⁹ J s) and T_L, T_R and T_{mol} are the transmission co-efficients of the left and right contacts and the molecule respectively.

The maximum conductance per conductance channel, i.e. the situation where T_L. $T_R.T_{mol}$= 1, can be shown from equation 1.1 to be $G_0 = \frac{2e^2}{h} = 77500$ nS; this value is called the quantum of conductance.

1.2.1.2 Instrumentation and Principles of Operation

Scanner- The scanner is responsible for the movement of the tip in all three mutually perpendicular directions; X, Y and Z. Separate voltage signals give independent movement of the three axes, as well as high resolution over a relatively large range. In order to meet these specifications piezoelectric actuators are

employed. These contain a piezoelectric material, which is stretched or compressed with nanoscale precision upon applying a voltage.

Tip - The tip is one of the most important components of the STM, its geometry and chemical nature are both crucial for optimum operation. The best results are obtained when tunnelling occurs through a single atom at the end of the tip; therefore the ideal is a tip with a monoatomically sharp apex. If tunnelling occurs through multiple atoms on the tip, anomalous imaging artifacts can appear. This is often referred to as double-tip imaging. It is also possible for tunnelling to occur through a group of atoms; in this case the image will appear as a convolution of multiple images.

Controlling the shape of a tip down to the final atom is not easy. However, it is often found that if certain metal wires are cut, a rugged surface with a single protruding atom is achieved. This is often enough to obtain images of atoms. It is also possible to electrochemically etch tips; this allows the surface geometry of the tip to be controlled.

Tungsten tips are most commonly used in Ultra High Vacuum (UHV) STM. However, in ambient-conditions gold and platinum/iridium tips are preferred, as tungsten oxidises easily in air. Gold tips are highly favourable when studying sulfur terminated single molecules due to the strong affinity of sulfur for gold.

The Feedback Loop - The STM employs a feedback loop, which acts to control the tip-sample separation in order to maintain a constant current. When the STM tip is close enough to the substrate surface a tunnelling current will flow, which is amplified by a controller. When the tunnelling current passing between the tip and sample deviates from a user-defined current, called the set-point, an error signal is generated and used by the feedback loop to re-position the tip so that the set-point is maintained. The gain settings of an STM determine its sensitivity to the error signal. The inherent time delay within the feedback loop means that a higher gain setting results in faster approach of the reference position. The gain value must be selected carefully, if it is set too high the system will rapidly overcorrect, resulting in oscillation about the reference position, However, if the value is too low the system will respond more slowly, which may cause the tip to crash into the surface of the substrate.

1.2.2 Measuring Conductance Using an STM

In recent years STM systems have been modified in order to allow the determination of the conductance of a single molecule. There are three main techniques that have been developed:

- *I*(*s*) Method
- *I*(*t*) Method
- STM break junction technique

All three methods use a (sub-)monolayer of molecules adsorbed onto the substrate surface and involve the formation of metal-molecule-metal junctions. The way these junctions are formed varies slightly between the methods.

1.2.2.1 The I(s) Method

This technique was introduced by Haiss *et al.* in 2003[13] and measures the tunnelling current as a function of the distance between the tip and substrate. The tip is held within close proximity of the surface of the substrate (Figure 1.4, A), the exact value of the tip-substrate gap at this point is determined by the set-point. Molecules on the surface of the substrate can bridge the tip-substrate gap, thus forming a metal-molecule-metal junction (Figure 1.4, B). The tip is retracted and pulls the molecules upright, until eventually the tip-substrate gap reaches the length of the molecule thus causing the junction to break (Figure 1.4, C and D).
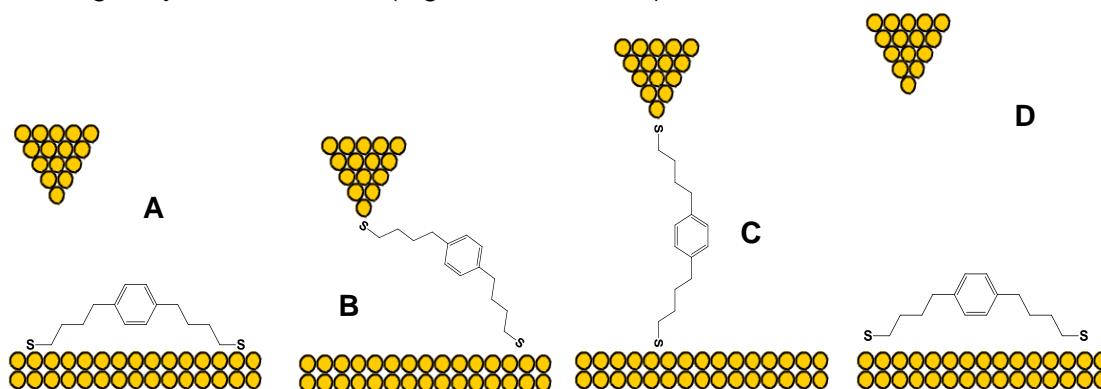
Figure 1.4. The I(s) technique of Haiss *et al.*[13]

If, during the acquisition of an *I*(*s*) scan, no molecule bridges the tip-substrate gap the current will decay exponentially to zero (Figure 1.5). However, if a molecule bridges the gap a current plateau will be observed; the current recorded within this plateau corresponds to the conductance of the molecule. Several hundred *I*(*s*) scans

are recorded and plotted in a histogram. The resulting peak is used to determine the average value of the current plateau in all the $I(s)$ traces, and the conductance can then be calculated using equation 1.2:

$$\sigma = \frac{I_w}{U_{bias}} \qquad\qquad \textbf{1.2}$$

where σ is the conductance (nS), I_w the current (nA) and U_{bias} the bias applied between the tip and the substrate (in volts).

Exponential decay seen when no
molecule bridges tip-substrate gap
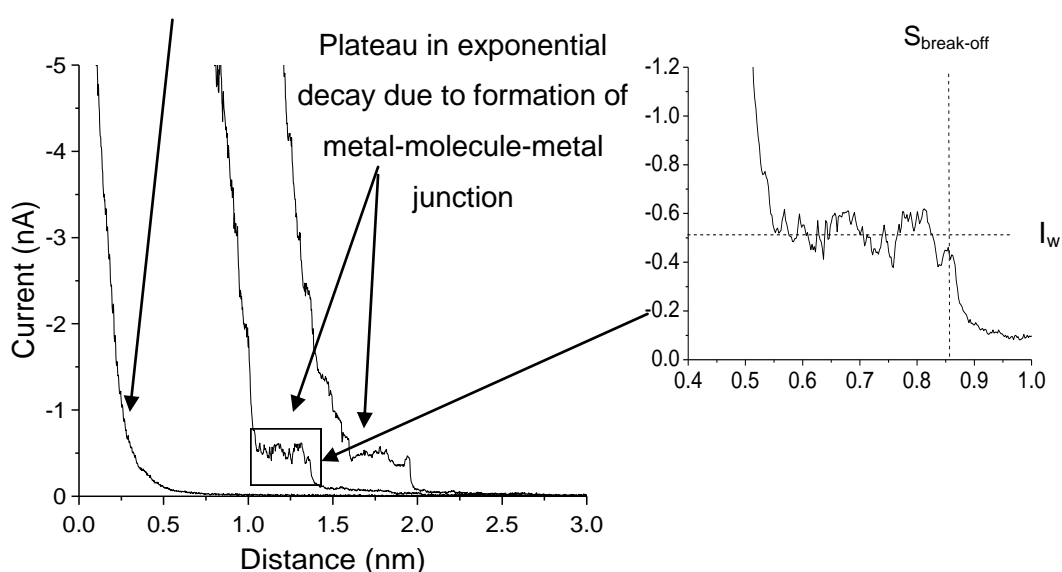
Figure 1.5 Example $I(s)$ scans.

The distance at which the metal-molecule-metal junction breaks can be compared to the known length of the molecule, thus confirming the formation of a molecular wire. The total break-off distance is the sum of two components:

$$S_{total} = S_0 + \Delta S \qquad\qquad \textbf{1.3}$$

The term S_0 represents the distance between the tip and the substrate at the predetermined set-point current. In order to calibrate this distance several $I(s)$ scans must be recorded during the conductance measurements that show no evidence of molecular bridge formation.

These scans are then plotted as *ln(I)* versus *s* (*ln (current)* vs. *distance displacement*) in the distance range relevant to the experiment. Linear regression is

8

used to determine $\frac{dln(I)}{dS}$, which is the slope of the plot. The following equation can then be used to determine the distance between the tip and the substrate at a given set-point value, I_0:[14]

$$S_0 = \frac{\ln \left(G_0 \times \frac{U_{bias}}{I_0} \right)}{\frac{dlnI}{dS}} \qquad \textbf{1.4}$$

where G_0 is the point contact conductance of gold (known to be 77400 nS) and U_{bias} is the bias applied between the tip and substrate.

The term ΔS represents the tip displacement, from S_0, at which the molecular bridge breaks. This is measured for every plateau included in the conductance histogram and often shows considerable variation, this is due to the stochastic nature of the junction breaking process. An average of all the experimental break-off distances is therefore used.

Haiss *et al.* introduced this method in the determination of the single molecule conductance of an *N*-alkanethiol disubstituted 4,4'-bipyridine (6V6) (Figure 1.6).[12]
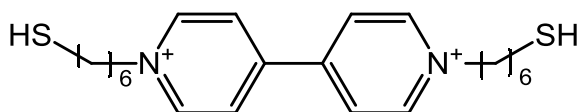
Figure 1.6 The viologen analogue 6V6.

A conductance value of 0.49 ± 0.08 nS at a bias of 0.2 V was reported. The appearance of two further conductance values at two and three times the magnitude of the first were also described. These were attributed to the presence of two and three molecules in the molecular junction respectively.

The group went on to describe the measurement of conductance in an electrochemical environment, which allowed them to control the redox state of the molecule during the measurements (see section 1.6.2.1).[13]

1.2.2.2 The I(t) Method

When determining single molecule conductance using the *I*(*t*) method the tip is held at a fixed position above the surface of the substrate, and the current is recorded as a function of time.[15] If the tip-substrate gap is shorter than the length of the molecule

it is possible for the adsorbed molecules to 'jump' and bridge the tip substrate gap. The jumps in $I(t)$ traces can be statistically analysed in much the same way as described for the $I(s)$ method, however a break-off distance cannot be determined in this method.
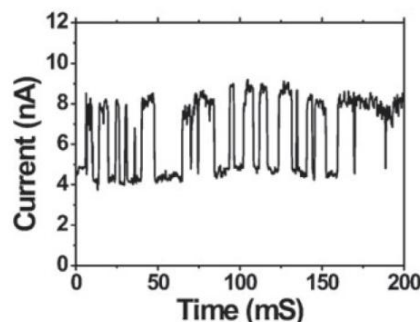
Figure 1.7 Example current jumps obtained using the I(t) method, taken from the thesis of Edmund Leary.

In Situ Break Junction (BJ) Method

The *in situ* BJ method, developed by Tao e*t al.* in 2003,[16] involves measuring the tunnelling current as a function of the tip-substrate separation in much the same way as the *I(s)* technique. However, the way in which the junctions are formed is different. In this case the tip is pushed into the substrate at the start of the scan, thus forming a metallic contact. As the tip is withdrawn from the surface large current jumps can be seen. These jumps correspond to G_0, the point contact conductance of gold, and multiples thereof. As the contact is cleaved it creates the break junction into which a molecular bridge can form. A series of smaller current steps can then be seen, which correspond to molecular junctions being formed and broken.

Tao *et al.* used this method to determine the conductance of 4,4'-bipyridine (BIPY), which they reported to be 774 nS.[16] They also used a series of control experiments to support their conclusion that molecular junctions were indeed being formed. Firstly, the measurements were performed in the absence of any molecules and in the presence of 2,2'-bipyridine, which, due to the relative positions of the two nitrogen atoms, cannot simultaneously bind to the two electrodes. In both cases no conductance peaks were seen below the value of G_0. Secondly, the experiments were performed at different potentials with respect to a reference electrode. At negative potentials, where the molecules would not be expected to bind to the electrodes, the conductance peaks below G_0 again disappeared. Finally, they

demonstrated that the conductance peaks were different for different molecules, and that the conductance of *N*-alkanedithiols decreased exponentially with the length of the molecule.

1.3 Transport Through Molecular Junctions

A molecular junction can be formed by contacting a single molecule between two metal electrodes, thus forming a metal/molecule/metal junction. The interfaces between the molecule and the two electrodes can give rise to energy barriers; the energy states of both the electrodes and the molecule are therefore important when considering the electron transport process. The metal electrodes are characterized by their densities of states, which are occupied up to the Fermi level. The molecule can be thought of as having a discrete set of energy levels, the most important of which for the transport process are the highest occupied molecular orbital (HOMO) and lowest occupied molecular orbital (LUMO). The energy barrier associated with the interfaces depends on the coupling regime between the molecule and the electrodes. For a physisorbed molecule the energy barrier can be large, and the coupling therefore weak. If a strong chemical bond exists between the molecule and the electrode, the energy barrier can be small and the coupling regime strong.

1.3.1 Coherent Charge Transport

The term "coherent tunnelling" refers to the transport regime in which the electrons flow elastically through the molecules without exchanging energy[17]. Intuitively, this will be the dominant mechanism as long as the time required for an electron to cross a molecular bridge is shorter than the time necessary for an electron to undergo an inelastic scattering event; coherent tunnelling therefore dominates through relatively short molecules. The decrease in conductance, σ_M, as a function of the length of the bridging molecule in this regime follows an exponential distance dependence:

$$\sigma_{M=}G_{con}e^{-\beta R} \qquad \qquad \textbf{1.5}$$

where $G_{con} = G_0 T_L T_R$. It can be seen that conductance, σ_M, decreases exponentially with the bridge length (or tunnelling barrier) *R*, as quantified by the attenuation factor, *β*. A plot of *lnσ_M* versus *R* can be used to determine the magnitude of *β*. A linear dependence of *lnσ_M* versus *R* and high values of β are usually associated with a coherent tunnelling mechanism of charge transport.

1.3.1.1 Manifestations of Coherent Charge Transport

The simplest way to model the tunnelling current density of a molecular junction is as an arbitrary tunnel barrier within the Simmons approximation:[18]

$$I = \frac{eA}{4\pi^2\hbar d^2}\left\{\left(\phi - \frac{eV}{2}\right)exp\left(-\frac{2d\sqrt{2m_e}}{\hbar}\sqrt{\phi - \frac{eV}{2}}\right) - \left(\phi + \frac{eV}{2}\right)exp\left(-\frac{2d\sqrt{2m_e}}{\hbar}\sqrt{\phi + \frac{eV}{2}}\right)\right\} \qquad \textbf{1.6}$$

where A is the junction area, d is the barrier width, m_e is the electron effective mass, ϕ is the barrier height and e is the electron charge. In molecular junctions the barrier width corresponds to the molecular length, whilst the difference between the Fermi level of the electrode and the nearest molecular orbital can be used to approximate the barrier height.

In the low bias regime, when the voltage is much smaller than the barrier height, and with no molecular energy level within the accessible energy range, direct tunnelling is the only possible mechanism. In this case the Simmons model can be simplified to:

$$I \approx \left(\frac{e^2V\sqrt{2m_e}\phi}{h^2d}\right)\exp\left(-\frac{2d\sqrt{2m_e}\emptyset}{\hbar}\right) \qquad \textbf{1.7}$$

This can be rewritten in order to allow for comparison to experiment using the decay constant, β:

$$I \propto Ve^{-\beta d} \qquad \text{with } \beta = \frac{2\sqrt{2m^*\phi}}{\hbar} \qquad \textbf{1.8}$$

In the high bias regime the voltage is larger than the average barrier height, there are now molecular energy levels available in the accessible energy range and the conduction mechanism is replaced by Fowler-Nordheim tunnelling. The Simmons model can be approximated as:

$$I \approx \left(\frac{e^3V^2}{\hbar d^2\phi}\right)exp\left(-\frac{4d\sqrt{2m_e}\phi^{\frac{3}{2}}}{3\hbar eV}\right) \qquad \textbf{1.9}$$

This can be rewritten in the form:

$$I \propto V^2exp(-\beta_{FN}d) \qquad \text{with } \beta_{FN} = \frac{4\sqrt{2m_e}}{3\hbar eV}\phi^{\frac{3}{2}} \qquad \textbf{1.10}$$

In principle, several molecular orbitals can participate in the electron transport simultaneously. However, it can be envisaged that if one level (HOMO or LUMO) lies closer to the Fermi level of the metal it will dominate the transport in a certain voltage range. Such a situation can be described by the resonant tunnelling model.
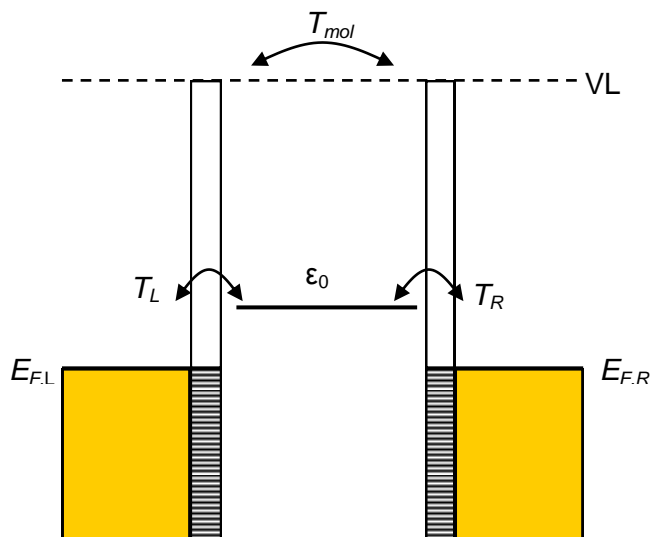
Figure 1.8 Energy level scheme of a molecular junction where the transport is dominated by a single level, ε_0.

At low bias, when the Fermi levels are away from resonance by ε_0, the current is quite low, especially if T_L and T_R are small. In the resonant condition the level is aligned with the chemical potential of one of the electrodes; as the voltage approaches this condition the current is greatly enhanced. Finally, at sufficiently large voltages, the current saturates and is determined by T_L and T_R.
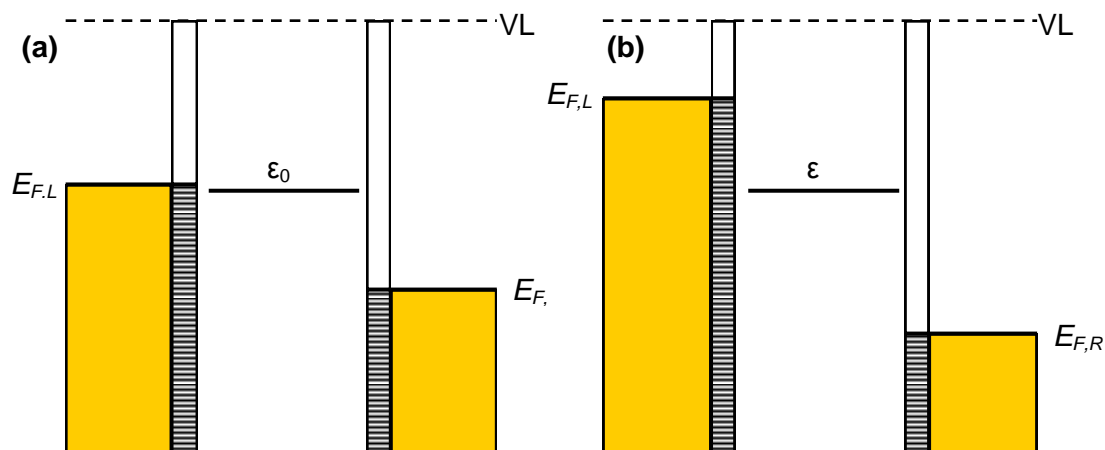
Figure 1.9 Voltage dependance of the level alignment in the resonant tunnelling model in (a) the resonant situation and (b) the large bias region, where the current saturates.

One final situation to consider is that where the charge carriers overcome the metal-molecule barrier by thermal agitation. This mechanism of transport is known as

thermionic emission and shows strong temperature dependence. Thermionic emission observed in several molecular junctions can be described using the Schottky-Richardson relationship[19]:

$$I = AT^2 exp\left(-\frac{e\Phi_{TE} - e\sqrt{\frac{eV}{4\pi\varepsilon_0\varepsilon_r d}}}{kT}\right)$$

1.11

where A is the effective Richardson constant, Φ_{TE} the thermal emission barrier height, ε_0 the permittivity of vacuum and ε_0 the dielectric constant of the molecular layer. Its voltage dependence takes the form:

$$I \propto exp(V^{\frac{1}{2}})$$

1.12

The classification of this mechanism as coherent originates from the elastic passage of the electrons over the potential barrier.

1.3.2 Double Barrier Tunnelling

Double barrier tunnelling is a quantum physical phenomenon. Classically, if two barriers were lined up in series the transmission across both barriers would be less than the transmission across one. However, in particle tunnelling when a wave hits an energy barrier there are always two components of the wave; the transmitted part, which penetrates the barrier, and the reflected part, which does not. In the case of a double barrier tunnelling junction, two energy barriers are separated by an energy well, inside of which the transmitting particle can become localized. Since both barriers can reflect the wave, constructive interference becomes possible. This serves to enhance the transmission probability across the two barriers.

1.3.3 Non-Coherent Charge Transport

The incoherent hopping regime manifests itself when the time an electron takes to traverse through a potential barrier is larger than the time scales associated with inelastic interactions (or scattering events). The realisation of this mechanism therefore becomes more likely as the length of the molecular bridge increases. In the most extreme case, when the scattering time is much smaller than the tunnelling time, the electrons can be localized at certain points within the molecule, and can

hop between these points. The current in this regime is directly proportional to the voltage.
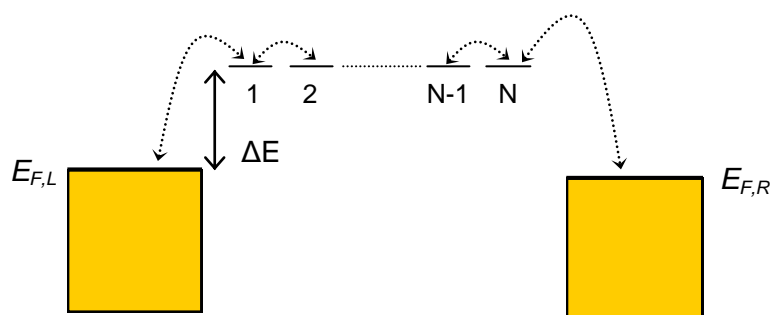
Figure 1.10 Schematic representation of the hopping regime. Here the molecule hops across the molecule via *N* sites with the same energy. ΔE is the activation energy for this process.

1.3.4 Identifying the Transport Mechanism

The mechanism of charge transport can often be investigated using both the temperature and voltage dependencies of a molecular system. If a system is thermally activated it falls into the thermionic or hopping category. The temperature dependence of hopping follows the form:

$$\ln\left(\frac{I}{V}\right) \propto \frac{1}{T}$$

1.13

whilst that of thermionic emission follows the form:

$$ln\left(\frac{1}{T^2}\right) \propto \frac{1}{T}$$

1.14

Although temperature dependencies provide insights into the mechanism of charge transport, the experimental techniques designed to work with single molecules are not always suitable for temperature dependent measurements. Thus, it may not be possible to use the temperature dependencies to distinguish between thermionic emission and hopping. Furthermore, the coherent tunnelling mechanisms do not usually exhibit any temperature dependency. In these cases the transport regime can be discriminated by analysis of the current-voltage characteristics.

1.3.5 Transition Between Charge Transport Mechanisms

Since the mechanism of transport through a molecular wire depends on both bias and molecular length, it is possible to observe transitions between certain mechanisms. Frisbie and coworkers have demonstrated the transition between both direct tunnelling and Fowler-Nordheim Tunnelling with increased voltage, and direct tunnelling and hopping on increasing molecular length, within a series of oligophenyleneimine (OPI) molecules (Figure 1.12).[20] The molecules varied in length between 1.5 and 7.3 nm, and were investigated using an atomic force microscope (AFM).
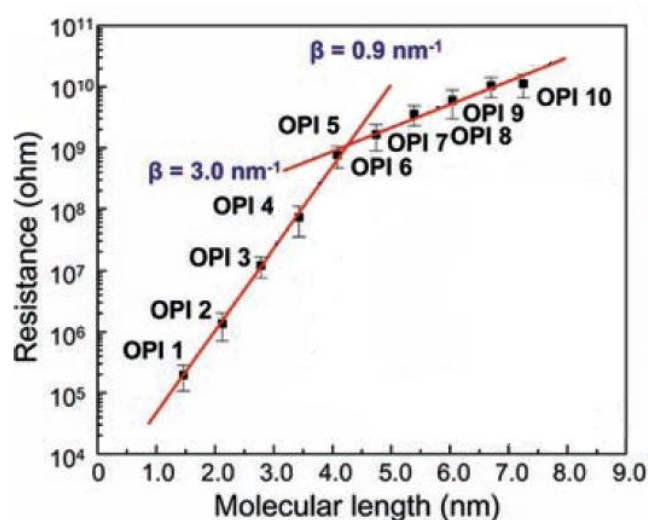
Figure 1.11 A semilog plot of resistance versus molecular length for a series of oligophenyleneimine molecules. The plot shows two distinct regions of length dependence. Reprinted with permission from Choi *et al.*[20] Copyright (2008) The American Association for the Advancement of Science.

A semilog plot of resistance versus molecular length in this series of OPI molecules (Figure 1.11) was shown to have two distinct regions of length dependence, which strongly indicates that the conductance mechanism is different in short and long OPI molecular wires; the transition between mechanisms appeared to occur at around 4 nm. In shorter molecules a linear fit to the data provided an attenuation factor of 3 nm^{-1}, which is within the acceptable range for non-resonant tunnelling. For longer molecules the attenuation factor was found to be around 0.9 nm^{-1}, which suggests that the principle transport mechanism is hopping. A study of the dependence of resistance on temperature showed that only longer molecules exhibit thermal activation, which is also consistent with a hopping mechanism.
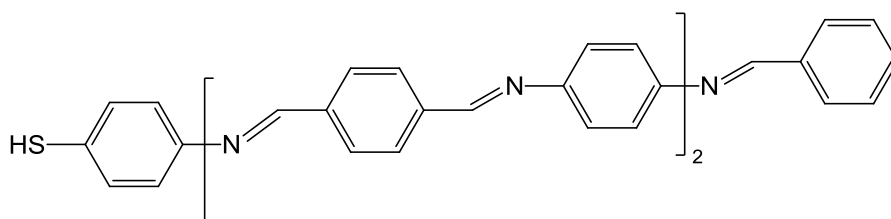
Figure 1.12 An example of an OPI molecule studied by Choi *et al*.X

Plots of the I-V characteristics for the two distinct regions also exhibited very different behaviour. The longer molecules showed a linear relationship at low bias, which in this case provides further evidence for a hopping mechanism. A log plot of OPI 4, a representative shorter molecule, shows two distinct regions with a transition at 0.75 V. In the low bias regime the current scales linearly with voltage; from equation 1.4 it can be seen that this voltage dependence is in good agreement with that expected of direct tunnelling. At higher voltages the current scales linearly with 1/V, which is indicative of a transition to Fowler-Nordheim tunnelling. A decrease in the transition voltage with decreasing length suggests that the barrier height also decreases with length, which is as predicted from the trend in oxidation potentials determined by cyclic voltammetry (see 1.5.3).

The same group had previously studied this latter transition in some detail in a series of π-conjugated thiols.[21] Upon combining their transport results with photoelectron spectroscopy experiments, it was possible to correlate the transition voltage with the energy level alignment.

17

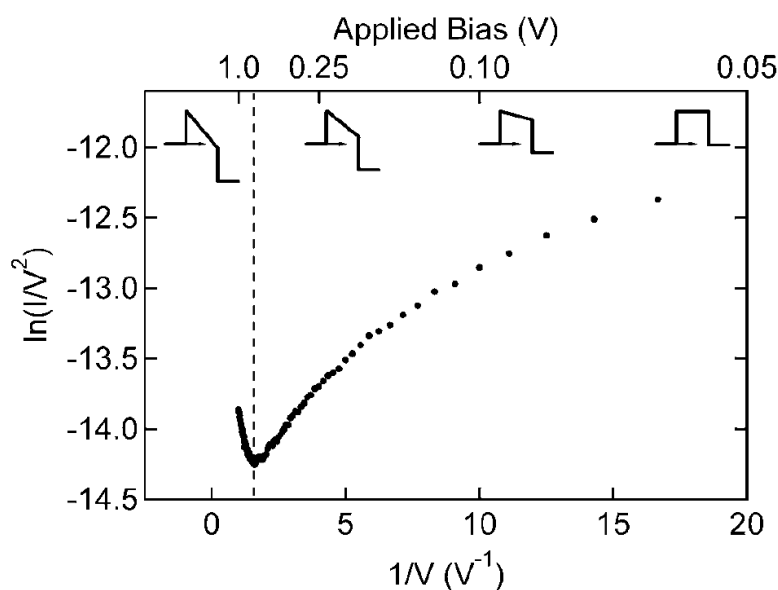**Figure 1.13 A plot of 1/V vs. ln(1/V^2) for a Au-anthracenethiol-Au junction. The dashed line represents the transition voltage. Also shown are representations of the barrier shape at various values of applied bias. Reprinted with permission from Beebe *et al.*[21] Copyright (2006) American Physical Society.**

The group described the change in mechanism as a transition from a trapezoidal to a triangular tunnelling barrier. In the zero-bias regime the barrier is rectangular and the Simmons approximation can be simplified to equation 1.5. In the low bias regime, when the applied bias is less than the barrier height, the Simmons approximation describes a trapezoidal barrier. Finally, when the applied bias exceeds the barrier height the barrier transitions from trapezoidal to triangular, and the current-voltage dependence can be described by equation 1.7.

1.4 Self Assembled Monolayers

A common contact in single molecule conductance measurements is thiols adsorbed onto gold; self assembled monolayers of thiols on gold surfaces will be therefore be discussed in this section.

Self assembled monolayers (SAMs) are arrangements of molecules on a solid surface, which have been formed spontaneously from solution or from a vapour phase.[22] Each molecule can be divided into two main parts, a headgroup and a backbone; the headgroup links the backbone to the surface. The interactions between the backbones of the molecules determine the packing and stability of the monolayer, increasing chain length of the backbone therefore increases the stability of the monolayer.

18

1.4.1 Thiol and Dithiol SAMs adsorbed onto Gold

Self assembled monolayers of thiol and dithiol molecules on gold surfaces have received particular attention due to their ease of preparation and high stability in ambient conditions, attributes which make them promising in many fields of nanotechnology. Since their discovery by Nuzzo and Allara in 1983,[23] many aspects of thiol and dithiol SAMs adsorbed onto Au(111) surfaces have been studied extensively both theoretically and using a variety of surface science techniques.[24-28] Despite this, a thorough understanding of the chemistry of the gold-thiolate bond is yet to be achieved. Recent data, both experimental and theoretical, suggests that an interaction between the adsorbates and the surface induce a strong reconstruction of the Au(111) surface involving the formation of thiolate-adatom moieties.[29]

1.4.1.1 The Self Assembly Process

Self assembly of thiols and dithiols on Au(111) surfaces is easy to perform and can be achieved from both gases and solutions. Adsorption times depend on the nature of the adsorbate, for example longer chain alkanethiols have lower adsorption times than their shorter counterparts. The simplest model of the self assembly process involves an initial physisorption step, followed by chemisorption and finally the formation of ordered domains in a close packed configuration (Figure 1.14).[30]
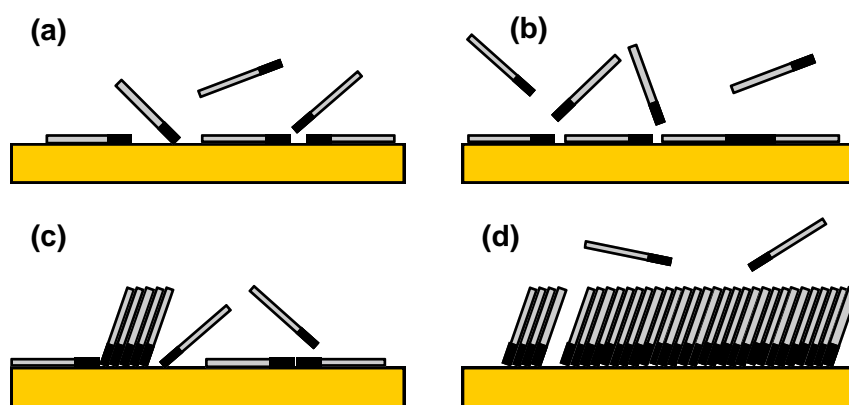

Figure 1.14 The steps of the self assembly process: (a) physisorption, (b) lying down phase formation, (c) nucleation of the standing up phase and (d) completion of the standing up phase.

The physisorption step is difficult to study, as the movement of the mobile species is too rapid for them to be observed by a scanning tunnelling microscope (STM) at room temperature. Images of physisorbed methanethiol and dimethyl disulfide molecules have, however, been achieved at 5K.[31] The subsequent chemisorption step sees the formation of a strong covalent bond, this process takes at least some minutes and leads to the formation of domains of "lying down" molecules. This process sees the loss of the thiol hydrogen, thus transforming the molecule into either a thiolate or a thiol radical. The nature of this process is not entirely understood, and the fate of the hydrogen atom remains a hotly debated issue. Recent work supports the hypothesis that the hydrogen atoms react to generate H_2.[32]

After chemisorption of the molecules has begun, nucleation of islands containing lying down molecules takes place. These islands then continue to grow and increase the surface coverage until the standing up phase is complete.

1.4.2 Characterising Self Assembled Monolayers

Self assembled monolayers can be studied by many different surface science techniques, both *in situ* and *ex situ*. The SAMs employed within this work were characterised by polarization modulation infrared reflection/absorption spectroscopy (PM-IRRAS) and STM, the latter of which is discussed in some detail in section 1.4.1.

1.4.2.1 PM-IRRAS

PM-IRRAS is a very powerful, surface sensitive spectroscopic method that can be used to characterize SAMs absorbed onto metal substrates. It takes advantage of the different absorption of *p*- and *s*-polarised light at an interface.
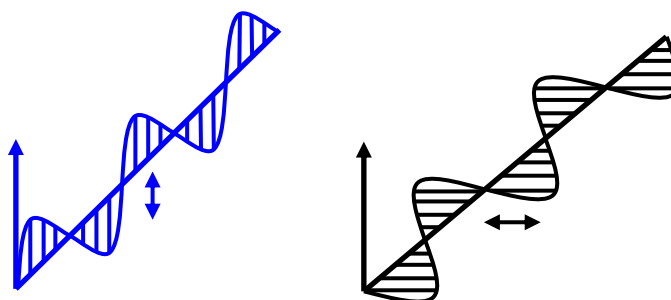

Figure 1.15 The components of *s* (blue) and *p* (black) plane polarized light.

The terms *s*- and *p*- polarised light refer to the orientation of the light component relative to the plane of incidence (Figure 1.15); the *s*- component is perpendicular whilst the *p*-component is parallel to this plane. Self assembled monolayers on metal surfaces interact with the *p*-polarised component of the light, but not with the *s*-polarised one. This means that any differences in measured *p*- and *s*- polarised light can be attributed to molecules on or close to the surface of the interface. PM-IRRAS employs a high frequency modulation between *s*- and *p*-polarisation, thus it can measure two signals simultaneously: the difference between the spectra for *s*- and *p*-polarised light and the corresponding sum spectra. It is therefore possible to construct spectra for SAMs on reflecting surfaces. Since it is the *p*-polarised component of light that interacts with the SAM, the vibrations that can be detected must have a dipole moment in the direction normal to the sample. This requirement is what gives rise to the surface selection rule for PM-IRRAS.

1.5 Electrochemistry

One area of great interest in single molecule conductance is molecular switching through manipulation of the redox state of the molecule. It is therefore important to understand electrochemistry and the electrochemical methods used to investigate the redox properties of molecules.

Electrochemistry is the study of chemical reactions that take place at the interface of an electrode and an electrolyte, and which involve the transfer of electrons between the electrode and either the electrolyte or a species in solution.

1.5.1 Electrode Potentials

Consider an aqueous solution of Fe(II) and Fe(III) ions, which is electroneutral due to the presence of negatively charged counter ions. The electronic structures of the ions differ by only one electron, it therefore follows that the ions can be interconverted by the addition or removal of a single electron. If a metal wire, for example platinum, is dipped into the solution it can act as a source or sink of a tiny number of electrons. This would serve to oxidise the Fe(II) ions or reduce the Fe(III) ions. Since both of these redox reactions can occur simultaneously, an equilibrium is established at the surface of the metal:

$$Fe^{3+}(aq) + e^{-}(metal) \longrightarrow Fe^{2+}(aq)$$
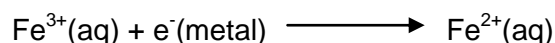
If this equilibrium lies to the left the electrode will bear a net negative charge and the solution a net positive charge. Conversely, if the equilibrium lies to the right the electrode will bear a net positive charge and the solution a net negative charge. In either case there will exist a charge separation, and therefore a potential difference, between the metal and the solution.

This means that the relative amounts of Fe(II) and Fe(III) in the solution will affect the potential difference. The potential difference is in fact given by the Nernst equation:

$$E = E^0 + \frac{RT}{nF} \ln \frac{[Fe^{3+}]}{[Fe^{2+}]} \qquad \qquad \textbf{1.15}$$

where E = Potential difference, E^0 = Standard potential, R = the gas constant (8.31 J K^{-1} mol^{-1}), T = absolute temperature (K), F = the Faraday constant (96487 C mol^{-1}) and n = number of electrons transferred.

It can be seen from this that two different types of electrochemical experiment are possible:

1. Equilibrium electrochemistry – experiments in which an electrode is dipped into solution, thus establishing an equilibrium according to the predictions of the Nernst equation. Such experiments can be used to yield precise sets of thermodynamic data.
2. Dynamic electrochemistry – experiments in which a potential is applied between the electrode and solution, which causes the concentrations of the analytes to adjust in order to comply with the Nernst equation. This type of electrochemical experiment has synthetic and mechanistic importance.

1.5.2   Electrode reactions

A typical electrode reaction involves a sequence of steps:

- Mass transport – the movement of the reactant to the interface of the electrode and electrolyte solution
- Electron transfer – this takes place *via* quantum mechanical tunnelling between the electrode and the reactant
- The product moves away from the electrode, thus allowing fresh reactant to reach the interface

There are several types of electrode reaction, the simplest of which is a single electron transfer reaction. An example of this is the reduction of Fe^{3+} to Fe^{2+}, and is depicted in Figure 1.16.
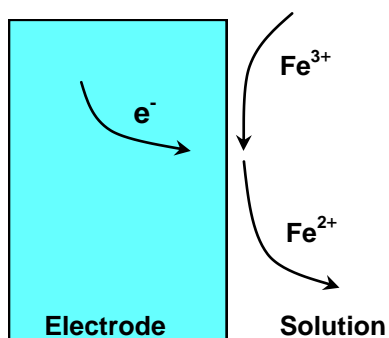

Figure 1.16 A single electron transfer reaction.

The Fe^{3+} moves towards the interface, where it accepts an electron from the electrode, thus forming Fe^{2+}. The product then moves away from the interface allowing further reactant to reach it. By monitoring the current throughout the experiment it is possible to determine exactly how many Fe^{3+} ions are reduced.

If the species formed during an electrode reaction is unstable it is possible for further reactions to occur, an example of this is shown in Figure 1.17.
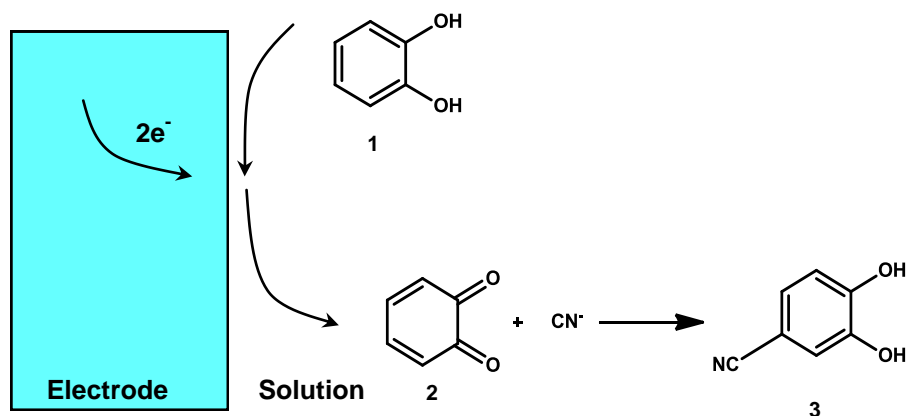

Figure 1.17 An example of an EC electrode reaction.

Here the reactant moves towards the interface, where it accepts 2 electrons from the electrode to form the intermediate *o*-benzoquinone **2**. However, the species formed in this two electron transfer process is unstable and undergoes a further chemical reaction to form the final product, 3,4-dihydroxybenzonitrile **3**.

The nomenclature used to describe the various mechanisms that can occur at an electrode involves the use of an E for an electron transfer reaction, and a C for a chemical reaction. The mechanism described in Figure 1.17 would therefore be called an EC mechanism. Further, more complicated mechanisms are possible. For example an ECE mechanism would involve an initial electron transfer step, followed by a chemical reaction and then a further electron transfer step.

1.5.3 Voltammetry

Voltammetry is a very useful tool commonly employed to acquire qualitative information about electrode reaction mechanisms. During voltammetry experiments the applied potential is varied whilst the resulting current is monitored. There are several types of voltammetry, including:

- Potential step voltammetry - experiments involve instantaneous jumps of the potential and the recording of the resulting current as a function of time. This allows the estimation of the diffusion coefficients of the species to be obtained.
- Linear sweep voltammetry – involves recording the current as a function of the electrode potential, which is swept from a lower limit to an upper limit. It is used to determine either the reduction or oxidation potential of a species.
- Cyclic voltammetry – this technique can provide information about both the forward and reverse redox potentials, as well as the diffusion coefficients. It is the method of choice for the work presented herein.

1.5.3.1 Cyclic Voltammetry

Cyclic voltammetry is frequently used to acquire information about the redox properties of organic compounds. As in linear sweep voltammetry, the potential of an electrode in contact with an analyte is controlled while measuring the resulting current. Most experiments use a three electrode set up, which consists of a working electrode, a reference electrode and a counter electrode. The working electrode is the electrode at which the reaction being studied occurs; depending on whether the reaction is oxidation or reduction the working electrode can be referred to as an anode or cathode. Common working electrodes consist of inert metals such as gold, or inert carbon such as glassy carbon. The counter electrode acts as the cathode when the working electron is functioning as the anode, and vice versa. The surface area of the counter electrode is often much larger than that of the working electrode, this is to ensure that the half reaction occurs rapidly and therefore does not limit the rate of reaction at the working electrode. The reference electrode is a half cell that has a stable, known potential and is used to measure and control the potential of the working electrode. The standard hydrogen electrode is the universal reference for reporting electrode potentials; its half cell is:

$$2H^+(aq) + 2e^- \rightleftharpoons H_2(g)$$
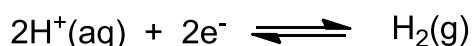
The absolute electrode potential of this system is estimated to be around 4.5 V at 25°C, but in order to allow comparisons between other electrode reactions its standard electrode potential is declared to be zero at all temperatures.

During a cyclic voltammetry experiment the potential is controlled between the reference and working electrodes, and the current flow between the working and

counter electrodes is measured. The potential is swept between two predetermined potential limits (Figure 1.18), with the current being monitored on both the forward and reverse sweeps. The data is then plotted as *current* (*i*) vs. *potential (E).*
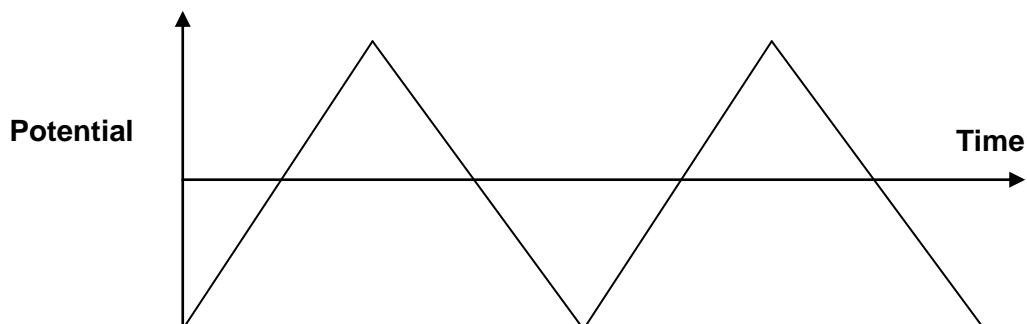

Figure 1.18 The potential waveform for a CV experiment.

If, during the scan, the potential approaches the redox potential of the analyte the current will increase. This increase slows as the concentration of the analyte at the interface decreases, thus producing a peak in the voltammogram. If the electrode reaction is reversible a second, reverse peak will appear when the applied potential is inverted. Cyclic voltammograms acquired in solution will always display a hysteresis between the reduction and oxidation peaks, due to the limits imposed by mass transport.
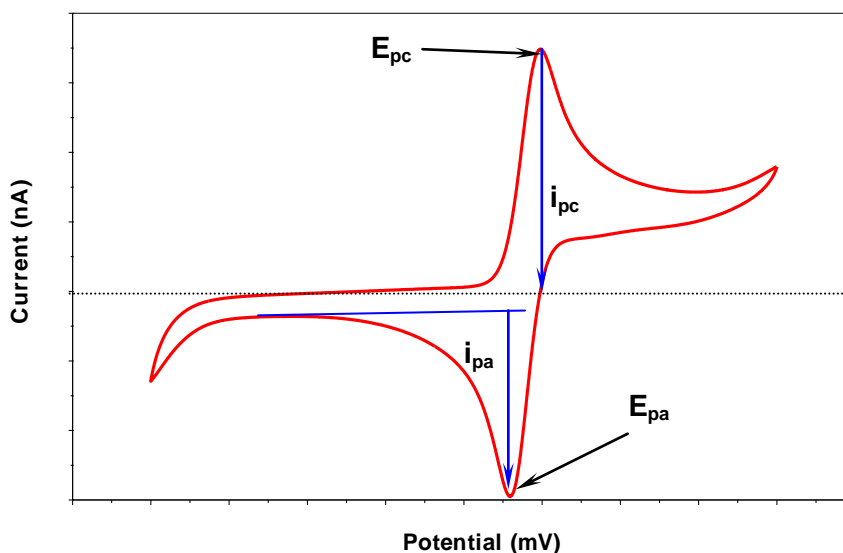

Figure 1.19 A typical cyclic voltammogram.

The electron transfer kinetics of the electrode reaction determine the shape of the cyclic voltammogram. If the electron transfer is very rapid compared with the rate of diffusion, the Nernst equilibrium can be maintained at the surface for all potentials

and the reaction is said to be reversible. The shape of cyclic voltammograms of reversible electrode reactions can be predicted by theory, and their peak currents are given by the Randles-Sevčik Equation:

$$i_p = 2.69 \times 10^5 n^{\frac{3}{2}} A D^{\frac{1}{2}} C_\infty v^{\frac{1}{2}}$$ **1.16**

where i_p = peak current (Amps), n = number of electrons transferred, A = electrode surface area (cm²), D = mean diffusion coefficient of solution redox species (cm² s⁻¹), C_∞ = bulk concentration (mol cm⁻³), v = sweep rate (volt s⁻¹).

There are also several diagnostic tests that have been devised for the analysis of reversible voltammograms:

- The peak separation is independent of sweep rate, and is equal to 59/n mV
- The ratio of the peak anodic and cathodic currents is one
- The peak current is proportional to $v^{1/2}$
- At potentials beyond E_p the current falls off with $t^{-1/2}$

If electron transfer is slow, and therefore insufficient to maintain surface equilibrium, the reaction is said to be electrochemically irreversible. Intermediate cases also exist, and are termed quasi-reversible. Figure 1.20 shows the effect of a decreasing rate constant of electron transfer.
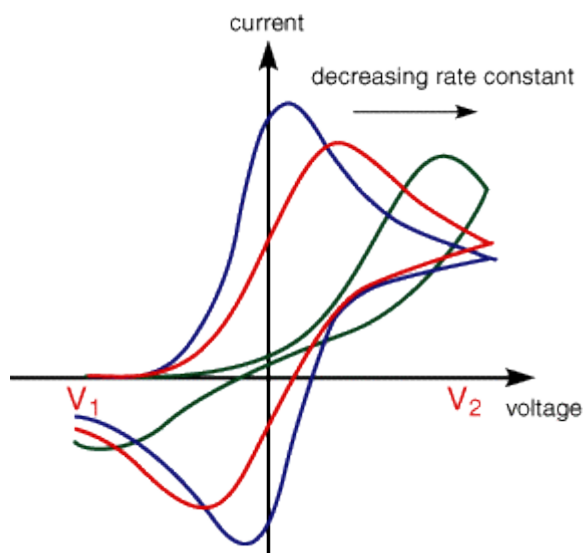

Figure 1.20. Voltammograms for different values of the rate constant.

The blue line shows the voltammogram of a process that has a high rate constant, and is therefore reversible. As the rate constant decreases the curves shift to more

and more extreme potentials, and slower sweep rates are necessary in order to observe a reverse peak.

The electron transfer step of an EC electrode reaction can be thought of as being chemically irreversible; in this case both the sweep rate and the rate constant of the subsequent chemical reaction will determine whether or not a reverse peak is observed.

1.6 Tailoring Electronic Behaviour

A clear advantage to the use of molecular systems in electronics is the almost limitless nature of molecules available to probe structure-property relationships, and thus tailor the electronic behaviour of the system. Since the introduction of methods to determine the conductance of single molecules, many systems have been investigated. The next pages will detail some of the structure-property relationships that have been probed, as well as some novel ways of gating conductance at the molecular level.

1.6.1 Anchoring Group Effects

As can be seen from equation 1.1, the nature of the metal-molecule coupling is one of the fundamental factors that determine the coherent transport in a molecular junction. The strength of this coupling can be tuned chemically, to a certain degree, by using appropriate anchoring groups. To date thiol groups are the anchoring groups most often used to form connections to metal leads, such as gold electrodes, due to their high affinity and strong covalent bonding to gold. Lately, however, it has been argued that the variability in the bonding between thiol groups and gold may be detrimental for the reliability of measurements of single molecule conductance.

Venkataraman and coworkers have investigated the potential use of amine groups to bind molecules to gold.[33] They measured the conductance of benzenediisonitrile, benzenedithiol and benzenediamine using the STM BJ method and reported that the latter gave a strikingly well defined peak in the conductance histogram, whilst the other two gave no well defined trend and a broad peak respectively. However, an estimation of the contact resistance for two amine-Au bonds show it to be a factor of ten times larger than the value for alkanethiols.
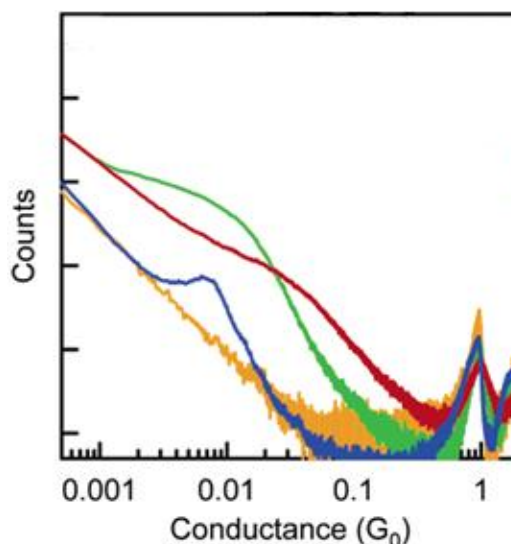
Figure 1.21 Normalised conductance histograms of over 3000 traces measured in the presence of 1,4-benzenediamine (blue), 1,4-benzenedithiol (red) and 1,4-benzenediisonitrile (green) on a log-log plot. The yellow line represents a control experiment where no molecules were present. Reprinted with permission from Venkataraman *et al.*[33] Copyright (2006) American Chemical Society.

The lack of a well defined peak for dithiols and diisonitriles in this work was attributed to variation in the binding to gold, as well as oxidative disulfide formation for thiols and ease of oligomerization for diisonitriles. Lörtscher and coworkers have since reported conductance measurements of dithiols using acetyl protected precursors, which are hydrolysed at the electrode surface thus avoiding disulphide formation.[34]

Tao *et al.* have systematically studied the effect of anchoring groups on the conductance of single molecules; they used the STM BJ method to measure the conductance of alkanes terminated with dithiol, diamine and dicarboxylic acid groups.[35] These anchoring groups bind to gold surfaces with differing strength. The Au-S bond is known to be a strong covalent bond, whilst the Au-NH$_2$ binding is thought to be a weak covalent interaction. The Au-COOH bond is not yet fully understood, but it is thought to involve both ionic and coordination interactions. The strength of these interactions is demonstrated by the variation in their experimental stretching lengths, which suggest that the S-Au contact is hardest to break and COOH-Au the easiest, whilst NH$_2$-Au is in between.

Since tunnelling is the expected mechanism for these molecules, their length dependence can be described by equation 1.5. A systematic study of the length dependence was used to determine values of G_{con}, which reflect the contact resistance. Values were shown to be 0.66 G$_0$, 0.037 G$_0$ and 0.007 G$_0$ for dithiol,

diamine and dicarboxylic-acid terminated alkanes respectively. Thus, the contact resistance appears to correlate with the binding strengths of the three contacts; stronger binding gives lower contact resistance. One factor that might affect the strength of the electronic coupling between the molecule and the contact is the size of the anchoring group. However, the variation in size in these molecules is much smaller than the corresponding variation of contact resistance. Thus, size alone does not seem to explain the observation. It is noteworthy that no issue was reported in this work regarding the measurement of single molecule conductance of dithiols.
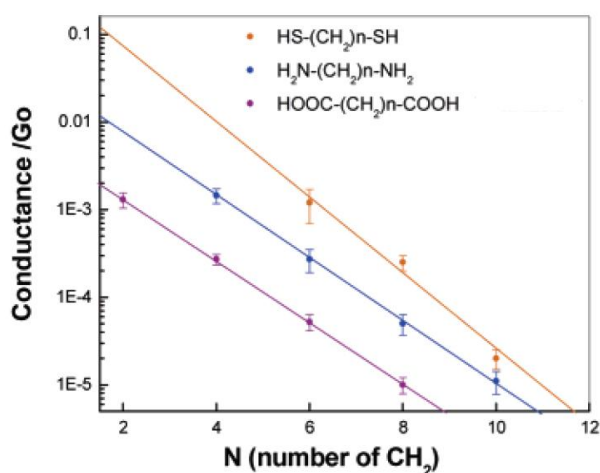

Figure 1.22 Logarithmic plots of single molecule conductance vs. molecular length. These plots allowed the determination of both β and G_{con}. Reprinted with permission from Tao *et al.*[35] Copyright (2006) American Chemical Society.

Tao *et al.* also observed differences in the magnitude of β, which is a measure of the decay with increasing length. They found that the anchoring groups differed with the trend β(dithiol) > β(diamine) ≥ β(dicarboxylic acid). Since both experimental evidence and theoretical calculations indicate that β depends on the alignment of the molecular energy levels relative to the Fermi energy of the electrodes, it can be deduced that anchoring groups change the energy level alignment.

The inherent nature of the amine and carboxylic acid anchoring groups mean that their binding to gold is expected to be dependent on the pH in which the measurement is carried out. For both diamine- and dicarboxylic acid- terminated alkanes the pH has a significant effect on either molecular junction formation or the conductance value; this is due to the protonation/deprotonation of the anchoring groups. Dithiol-terminated alkanes, contrastingly, show no significant pH dependence of conductance.

Kim and coworkers have shown that the variation in contact resistances between anchoring groups is caused by differences in the offset between the energies of the HOMO and the Fermi level of gold.[36] They used a conducting probe atomic force microscope to measure transport, and ultraviolet photoemission spectroscopy to probe the electronic structure of conjugated oligoacenes terminated with thiols or isocyanides. They found that the Au-CN contact was more resistive than Au-S, and that this difference correlates with the HOMO of the isocyanide series being lower in energy (relative to the Fermi level of gold) than the HOMO of the thiol series.

Venkataraman and coworkers have recently demonstrated a method of creating junctions with a direct Au-C covalent bond, thus removing the inherent resistance of the anchoring group.[37] They synthesised a series of $SnMe_3$-terminated polymethylene chains and measured their conductance using the STM BJ method. The conductance of a molecular junction formed using 1,4-bis-trimethylstannylbutane was shown to be about $0.1G_0$, which is approximately 100 times larger than that achieved with 1,4-diaminobutane. The results of this study strongly suggested that the $SnMe_3$ groups are cleaved *in situ*, leading to the formation of covalent Au-C bonds. These new direct Au-C contacts have since been employed to measure the single molecule conductance of a series of oligophenyl molecules, with the backbone containing two to four phenyl units.[38] The conduction mechanism of these molecules was shown to be tunnelling, and the decay constant shown to be 1.9 per phenyl unit.

1.6.2 Gating Molecular Conductance

Some of the most exciting studies in recent years have detailed variations in conductance with factors such as temperature,[39] environment[40,41] and redox state. Such variations can be exploited in order to gate the conductance at the single molecule level.[42]

1.6.2.1 Redox Gating

Perhaps one of the most studied methods of manipulating charge transport is the variation of redox state. Early work by Nichols' group demonstrated the change in conductivity of viologen based structures at fixed voltages,[43] this redox moiety has since received much attention.[44-51]
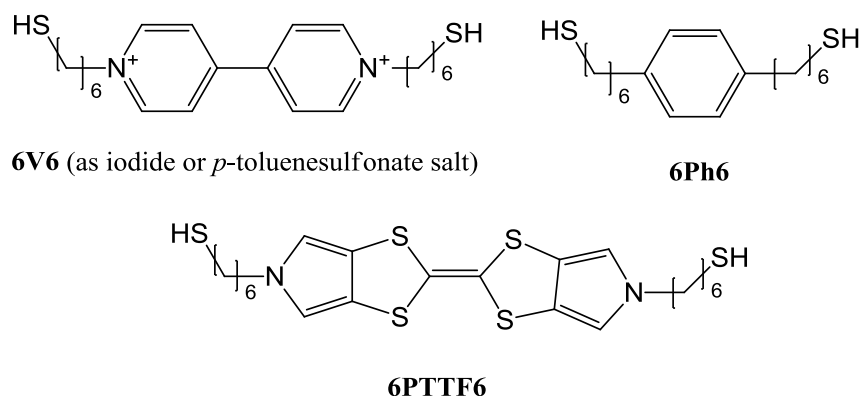
Figure 1.23 The structures of 6V6, 6Ph6 and 6PTTF6

Haiss *et al.* used the *I(s)* STM method to measure the conductance of a molecule containing a viologen centre as a function of its redox state.[13] In these experiments the gold tip and substrate act as the source and drain; the current flows between these two electrodes. The counter electrode acts as the gate. They reported reversible conductance changes from 0.5 to 2.6 nS when the molecule was switched from the oxidized to reduced state. The same group later used this method to probe structure property relationships in redox-gated single molecule junctions.[52] This latter study compared the conductance–overpotential behaviour of pyrrolo-tetrathiafulvalene (PTTF) and viologen (V) redox groups, as well as the conductance-electrode potential behaviour of the redox inactive phenyl (Ph) group (Figure 1.23). Figure 1.24 shows the reported single molecule conductance data for each molecule as a function of either the overpotential (redox active molecules) or the electrode potential (6Ph6).
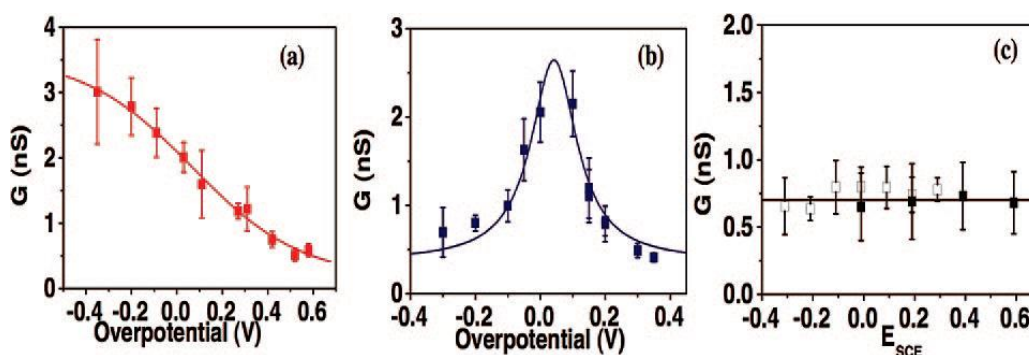

Figure 1.24 Single molecule conductance data for (a) 6V6 (b) 6PTTF6 as a function of overpotential and (c) 6Ph6 as a function of electrode potential (Solid points were acquired using the I(s) method, hollow points using I(t) method). Reprinted with permission from Leary et al.[52] Copyright (2008) American Chemical Society.

The data for the 6PTTF6 molecule exhibits a sharp *off-on-off* transition as the electrochemical gating potential is swept through the redox transition, while the data for the 6V6 molecule exhibits a much broader *off-on* switching profile. The conductance of the redox-inactive 6Ph6 was shown to be similar to that of the "off" states of 6V6 and 6PTTF, though it does not change as a function of potential.

The conductance of both 6V6 and 6PTTF6 in the "off" state, and the factor by which the conductance changed upon reduction/oxidation are similar. Since the $-(CH_2)_6SH$ spacer groups were present in all three molecules, presumably the difference must lie in the properties of the central redox moiety.

It has been suggested that the cause of the variation in these two systems is the significant configurational differences upon reduction in the viologen system. These are not present in the PTTF system, which has been shown to be planar in both the solid state and as an isolated molecule.

Whilst the viologen moiety has been shown to provide a means to reversibly gate conductance, other molecules have been studied that show irreversible conductance enhancement; one such example was demonstrated by Tao *et al.*[53] They investigated the electron transport properties of two oligo(phenylene ethynylene) (OPE) analogues using the STM BJ method.
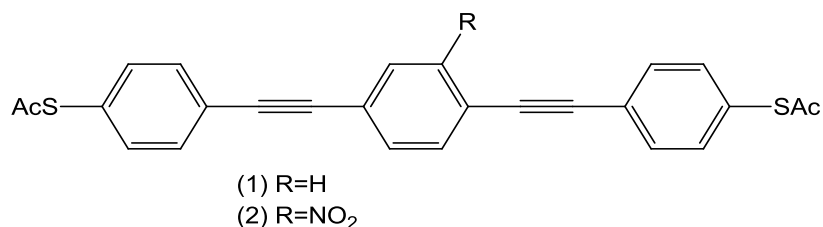

(1) R=H
(2) R=NO$_2$

Figure 1.25 The structures of (1) unsubstituted oligo(phenylene ethynylene) and (2) nitrosubstituted oligo(phenylene ethynylene), which were studied by Tao *et al.*[53]

The conductance values of molecules 1 and 2 were firstly determined in the absence of electrochemical control, and were shown to be ~13 nS and ~6 nS respectively. Subsequent analysis of the I-V characteristics of single molecule junctions also showed large differences. The most significant were asymmetric I-V curves for 2, as well as current peaks between 1 and 2 V; these resemble the negative differential resistance (NDR) effect. The NDR-like peaks diminish in the reverse voltage sweep, which indicates that an irreversible redox process is involved; it is suggested that this redox process is the reduction of the nitro moiety.

The conductance of 1 and 2 was then measured at potentials between -0.9 and 0.3V. For 1, the conductance was found to be independent of the electrode potential. The conductance of 2, however, was sensitive to the potential and showed an increase as the potential was shifted more negative. This change in conductance is attributed to the change in substituent on the central benzene ring; the irreversible reduction of the nitro moiety in aqueous solutions gives rise to this change in substituent. The reduction process can be described *via* a sequence of intermediates:

$$NO_2 \longrightarrow NO \longrightarrow NH(OH) \longrightarrow NH_2$$

The change in conductance was shown to correlate with estimations using Hammett's substituent parameter values,[54] which correlate the electronic effect of substituents with the rates and equilibrium of organic reactions.

1.6.2.2 Chemical Gating

The use of electron-donating and electron-withdrawing substituents has also been shown to create a conductance gating effect. Venkataraman and coworkers demonstrated this using a series of substituted benzenediamine (BDA) molecules, the conductance values of which were determined using the STM BJ method.[55] They found an increase in molecular junction conductance with electron-donating substituents, and a decrease in molecular junction conductance with electron-withdrawing substituents. The variation in molecular conductance was then related to the Hammett constants; this showed a clear trend of decreasing molecular conductance with increasingly positive Hammett constant (Figure 1.24). The negative slope indicates that the transition state in the tunnelling process is positively charged, which is consistent with hole tunnelling.
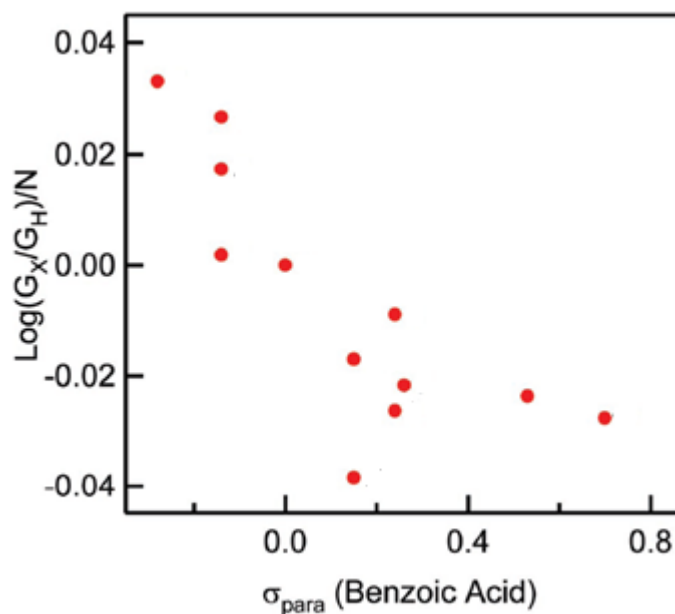
Figure 1.26 Log of the ratio of the substituted molecule conductance to the unsubstituted molecule conductance divided by the number of substituents in each molecule against the Hammett σ_{para} coefficient. Reprinted (adapted) with permission from Venkataraman *et al.*[55] Copyright (2007) American Chemical Society.

Leary *et al.* have reported a similar study on a series of molecules in which a benzene ring is sandwiched between two alkyl chains.[56] In these molecules, the frontier orbital energies of the alkyl groups lie far from the Fermi energy of gold, whilst the frontier orbital energies of the π-system of the benzene ring are much closer to the Fermi level. The benzene ring can therefore be thought of as acting as a barrier indentation, thus enhancing the magnitude of conduction.

The group then used a range of both electron-donating and electron-withdrawing substituents on the ring in order to change the frontier orbital energies of the well. The single molecule conductance of each analogue was then measured using both the *I(t)* and *I(s)* STM methods.
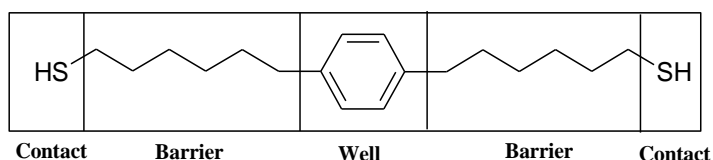

Figure 1.27 The molecule 6Ph6 as a double tunnelling barrier junction.

35

The results firstly showed that the conductance values were considerably greater than would be expected for alkanedithiols of comparable length, indicating that benzene rings do indeed serve as effective indentations in the tunnelling barriers. The group then plotted the conductance values against the HOMO energy for each molecule and observed a weakly linear relationship.
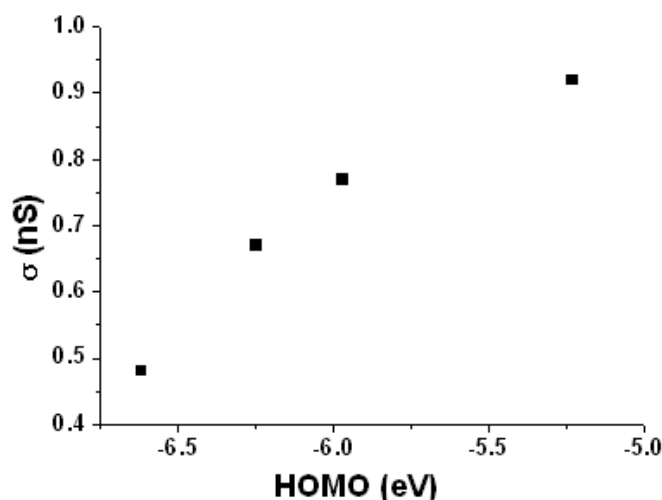

Figure 1.28 Plot of conductance against HOMO energy. Reproduced from data in the thesis of Edmund Leary.

This result suggests that, although the conduction mechanism in these molecules is probably different to those studied by Venkataraman *et al.*, the effect of substitution is the same and can be exploited in order to tailor the frontier orbitals and thus the single molecule conductance.

1.6.2.3 Environmental Gating

1,4-Benzenediamine (BDA) has also been used to investigate the effect of the environment on the conductance of single molecules. A study by Fatemi *et al.* utilised BDA to demonstrate a solvent gating effect using the STM break junction technique.[57] They determined the conductance for benzenediamine molecular junctions in a range of 13 different solvents with varying parameters such as molecular dipole moment, permittivity and chemical substituents. The resulting conductance trends showed no correlation with either the solvents' intrinsic molecular dipole moments or their bulk dielectric constants. It was noted, however, that the conductance was low for all chlorine containing solvents (chlorobenzene, for example), higher in solvents with bromine groups (bromobenzene for example) and nearly the highest in the solvent with an iodine group (iodobenzene). Thus, a

detailed theoretical study focused on three representative halogen containing solvents, chloro-, bromo- and iodobenzene, was performed. This allowed the group to explain the increase in conductance by showing that the solvents bind to undercoordinated gold sites around the molecular junction, thereby inducing a shift in the gold contact work function. This shift reduces the separation between the gold Fermi level and the HOMO of the benzenediamine in the molecular junction. Since the BDA junction conductance is known to arise through nonresonant tunnelling through the BDA HOMO, its conductance will show a dependence on the alignment between the Fermi level and the HOMO. The variation between the chloro, bromo and iodobenzene conductance can therefore be attributed to the variation in the binding energy of each of the solvents; the low binding energy of the chlorobenzene results in a low probability of a solvent molecule replacing a BDA molecule on an undercoordinated surface site.

Nakashima *et al.* presented similar findings using the STM BJ method to measure the conductance of BDA in tetraglyme, mesitylene, water and nitrogen.[41] By considering the molecular size and other physical properties, it can be predicted that the interaction between the Au electrode and solvent would decrease in the order of tetraglyme, mesitylene and water; the conductance of the single BDA molecular junction also decreased in that particular order. This result is consistent with increasing solvent interactions causing a reduction in the separation between the gold Fermi level and the HOMO of the benzenediamine in the molecular junction.

Leary and coworkers have reported that the presence of a water solvation shell has a dramatic effect on the conductance of a family of oligothiophene containing molecules, and that the longer the oligothiophene the larger the effect.[40] They investigated molecules comprising n thiophene rings (n=1,2,3,5) sandwiched between two alkyl chains using the STM *I(s)* method (Figure 1.29). Since the Fermi level of gold is predicted to lie within the HOMO-LUMO gaps of these molecules, the mechanism of conduction is likely to be tunnelling and the molecular conductances are expected to decrease exponentially with length.
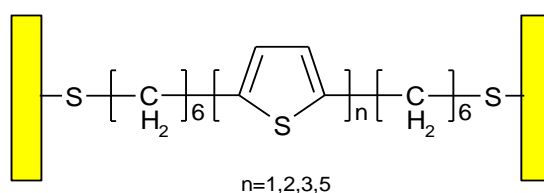

Figure 1.29 The structure of the family of oligothiophene molecules studied by Leary *et al.*[40]

The conductance histograms for the terthiophene analogue (n = 3) show a reversible switch from ≈ 0.012 nS in argon to ≈ 1 nS under ambient conditions (Figure 1.30). The group were unable to determine the conductance of quinquethiophene (n = 5) under argon; they attributed this to the current being too low to be recorded. Since this puts an upper limit of the conductance in the absence of water of 0.006 nS, it can be deduced that the conductance in the presence of water is over two magnitudes larger. In contrast, the conductance of the monothiophene analogue (n = 1) did not change significantly when switching between dry and ambient conditions.
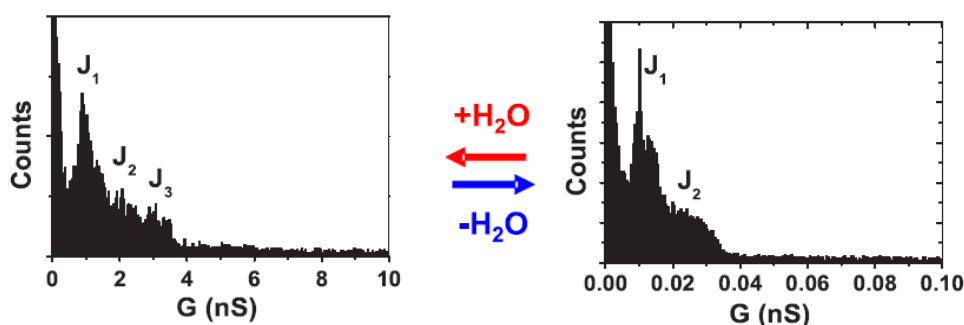

Figure 1.30 Histograms of the characteristic current plateaus observed for the terthiophene analogue (Figure 1.27, n = 3) under dry argon and ambient conditions. J_n denotes the number of molecules in the junction. Taken from the thesis of Edmund Leary

These results all agree with theoretical predictions, which showed a shift in the transmission resonances due to an interaction between the molecules and the first 38nterrupt shell of water. The longer molecules exhibit greater shifts due to the presence of a larger number of water molecules. Since straightforward alkanedithiols have the same molecular conductance whether measured in air or under vacuum it can be deduced that the interaction involves the aromatic backbone.

1.6.3 Conjugation

When considering the motion of charge in the coherent regime the charge pathway can be thought of as comprising of three key segments: the two metal-molecule interfaces, and the molecule itself. In order to achieve efficient conductance, strong electronic coupling among the segments must be achieved. The coupling within the molecule is provided by the orbital overlap of the molecular subunits, and is therefore enhanced by unsaturation and/or conjugation. The 38nterruptio π-electron

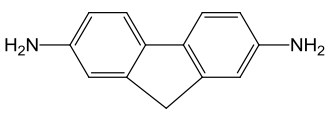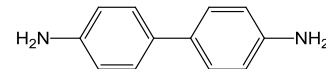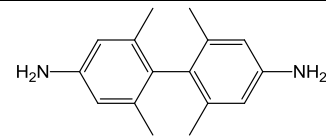system in conjugated molecules therefore makes them potentially very good candidates for molecular wires.

	Torsion Angle (°)	Conductance (G_0)
H_2N—⬡—⬡—NH_2	0	~1.54 x 10^{-3}
H_2N—⬡—⬡—NH_2	34	~1.16 x 10^{-3}
H_2N—⬡—⬡—NH_2	88	~7.6 x 10^{-5}

Figure 1.31 The molecular structure, torsion angles and measured conductance for some of the molecules studied by Venkataraman *et al.*[58]

In the case of a molecule containing a biphenyl moiety, the π-system of the two phenyl rings is strongly coupled when the two rings are coplanar. However, as the torsion angle between them is increased the coupling of the two subsystems will decrease to a minimum at π/2. It can be seen from this that the conductance of such a system should decrease with increased torsion angle, due to 39nterruption of the conjugation across the molecular bridge.

Venkataraman and coworkers have illustrated this idea by measuring the conductance of a series of diaminobiphenyl analogues using the STM BJ method.[58] They found that the conductance for this series does indeed decrease with increasing torsion angle (Figure 1.31). Furthermore, as the molecules gain additional rotational degrees of freedom, the conductance peak broadens. This latter observation is likely due to each molecular junction formed during the measurements consisting of a different conformation, with the final conductance peak being an average of all the possible conformations. This is supported by increased broadening of the conductance peak with increased rotational degrees of freedom.
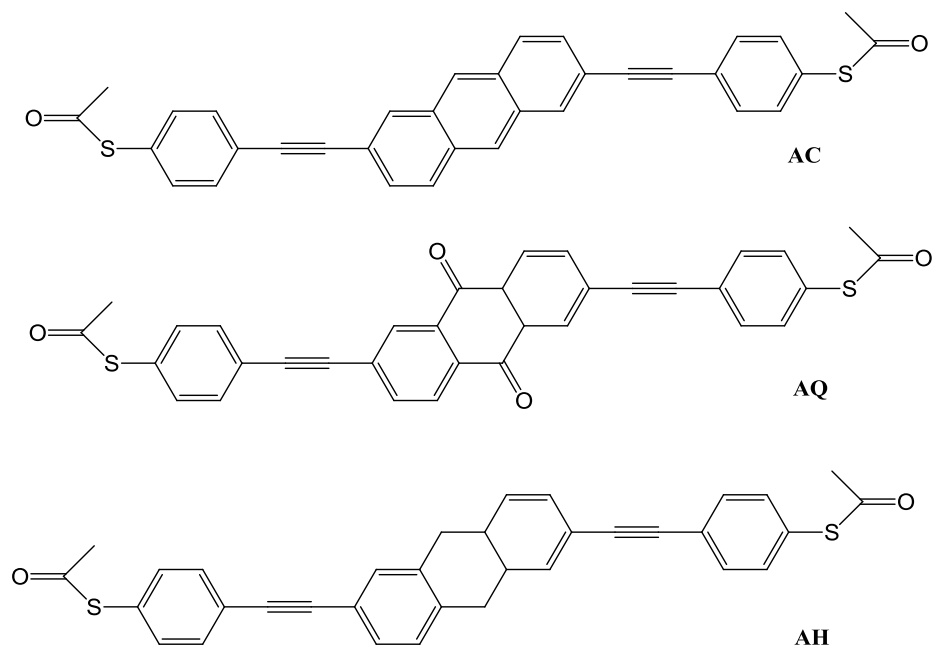
Figure 1.32 An anthracene-based linearly conjugated wire (AC), an anthraquinone-based cross conjugated wire (AQ) and a dihydroanthracene-based wire (AH) with broken π-conjugation.

Hong and coworkers have also studied the influence of conjugation on single molecule conductance using a mechanically controlled break junction setup.[59] They measured the conductance of an anthracene-based linearly conjugated wire (**AC**), an anthraquinone-based cross conjugated wire (**AQ**) and a dihydroanthracene-based wire (**AH**) with broken π-conjugation (figure 1.32). The measurements demonstrate that the conductance of the linearly conjugated molecule is several hundred times larger than that of the broken π-conjugated molecules, which in turn has a conductance value five times higher than that of the cross conjugated molecule. The latter result was attributed to destructive quantum interference. The observations in these experiments highlight the key role played by conjugation in charge transport.

Chapter 2

Varying Barrier Widths in α,ω-Dithiaalkane Molecular Wires

2.1 General Introduction

Since the first successful measurement of the conductance of a single molecule in 1997, a wide variety of systems have been investigated. One of the simplest groups of molecules that have been studied extensively are the alkane-thiol and dithiols; these have been most commonly tethered to gold electrodes *via* the strong Au-S bond. The linkages are chemically stable and have a large HOMO-LUMO gap, properties which make them ideal for probing the contribution of the metal-molecule coupling to the conductance. A variety of surface analytical tools have been used to characterise SAMs of both thiols and dithiols on gold surfaces, including X-ray photoelectron spectroscopy[60], Fourier transform infra red (FTIR),[61,62] Raman spectroscopy[63] and STM.[27]

2.1.1 Alkane Thiols and Dithiols

Several groups have used a variety methods such as STM,[64] atomic force microscopy (AFM)[65] and matrix isolation[66] to investigate charge transport through alkane thiol and dithiol systems. Whilst tunnelling was the generally accepted mechanism, this was not proven definitively until work by Reed and coworkers in 2003.[67] They detailed a systematic study of the temperature-dependent current-voltage ($I(V,T)$) characteristics of monolayers of alkanethiols, as well as the dependence of tunnelling current on molecular length. It can be seen from section

1.3.1 that the temperature dependence results will allow the conduction mechanism to fall into one of two categories:

- Thermionic emission or hopping, which show temperature dependent behaviour.
- Direct or Fowler-Nordheim tunnelling, which show temperature independent behaviour.

The group studied the $I(V,T)$ characteristics of dodecanethiol in the bias range $V = 0$ to 1 V at temperatures from 80 to 300K; they found no significant temperature dependence of these characteristics. This absence of thermal activation means the conduction mechanism falls into the tunnelling category. In order to distinguish between Direct and Fowler-Nordheim tunnelling a study of the current-voltage dependency is necessary. A plot of $\ln(I/V^2)$ *vs* $(1/V)$ can be seen in Figure 2.1 and shows no voltage dependence, which indicates no significant Fowler-Nordheim contribution in this bias range and proves the conduction mechanism to be direct tunnelling. Furthermore, this result determines that the barrier height is larger than the applied bias ($\emptyset_B > 1$ eV). The group concluded the study with length dependence measurements, allowing them to determine an attenuation factor of 0.83-0.72 Å^{-1}.
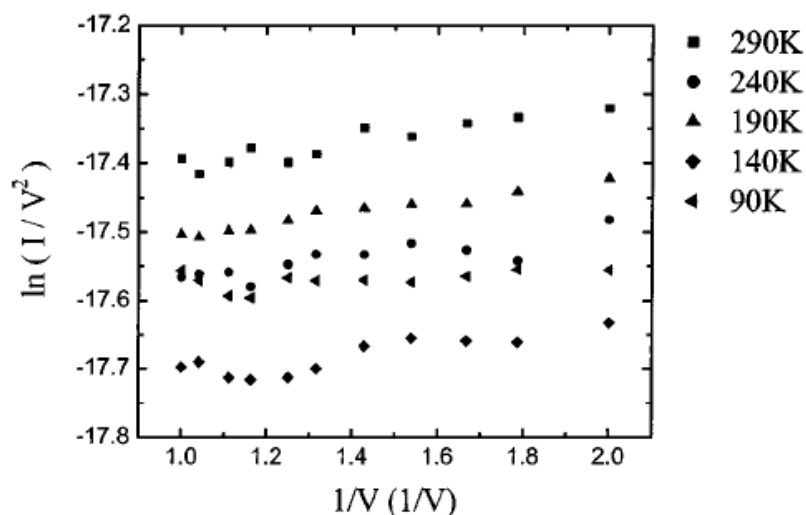

Figure 2.1 A plot of ln(I/V^2) *vs* (1/V) at various temperatures. Reprinted with permission from Reed *et al.*[67] Copyright (2003) American Physical Society.

The determination of the single molecule conductance of alkane dithiols of varying length has been undertaken by several groups, and has yielded quantitatively different results (Table 2.1). Haiss *et al.* studied the electrical conductivity of

hexanedithiol (HDT), octanedithiol (ODT) and nonanedithiol (NDT) using both the *I(s)* and *I(t)* STM methods (except in the case of HDT, which is too short to be easily measured using the *I(s)* method).[15] They reported conductance values of approximately 2.5, 1.0 and 0.5 nS respectively; the value for the conductance of ODT is in firm agreement with the value obtained by Cui *et al.* using a matrix isolation method.[66] However, all three values vary by at least an order of magnitude in comparison to similar results reported by Tao *et al.*, which were measured using the comparable break junction method[16].

	Molecule	σ (nS)	β (N^{-1})
Haiss (I(s) and I(t) Methods)	HDT	2.5	0.52
	ODT	1	
	NDT	0.5	
Tao (BJ Method)	HDT	93	1
	ODT	19	
	DDT	1.5	

Table 2.1 Comparison of the results obtained by Haiss *et al.*[14] and Tao *et al.*[16]

Tao and coworkers later refined their method and reported that two sets of well defined peaks could be seen, corresponding to two different conductance values.[64] The presence of these two groups was attributed to variations in the metal-electrode contact. They noted that each individual conductance curve generally only had steps from one conductance value, the presence of both in one curve was very rare. If the latter situation did occur they only ever observed the lower value after the higher one. These observations were used to propose the following:

- The higher conductance value corresponds to a molecule with both ends sitting on hollow sites of the gold electrodes.
- The lower conductance value corresponds to a molecule with one end on a top site of the electrode and the other end on a hollow site.

The group explains the lack of even lower conductance peaks corresponding to the top-top geometry to be due to the pulling of gold atoms out of the electrodes during the experiment. However, Fujihira *et al.* postulated that the group merely missed the conductance group because of the tunnelling background currents observed in their experiments.[68]

Haiss *et al.* attempted to address this by comparing experimental results from four different techniques, with an emphasis on the role of the surface morphology.[69] They

concluded that the appearance of different conductance groups could be attributed to different combinations of terrace and step edge adsorption sites of the sulfur contacts (Figure 2.2).

The low conductance group, A, is seen when both sulfur atoms adsorb at terrace sites, this is experimentally more likely at relatively large tip-sample separations. The medium conductance group, B, occurs due to one of the sulfur atoms adsorbing at the site of a step edge on the gold surface. Finally, the high conductance group, C, is due to the adsorption of both sulfur atoms at step edge sites, this is only possible when the tip is brought into close proximity of the sample and is therefore experimentally more likely during break junction experiments.
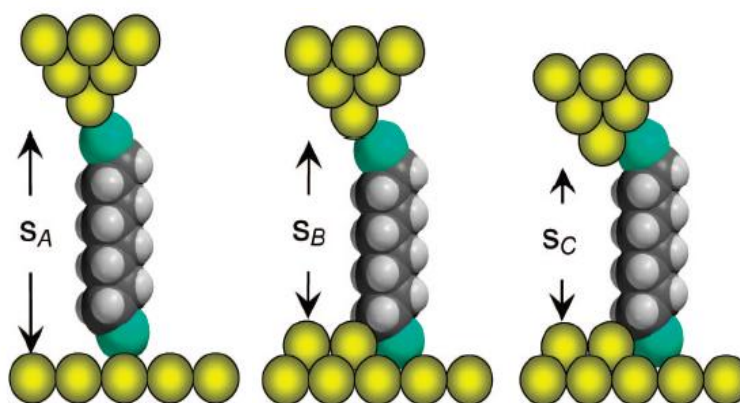

Figure 2.2 The various contact geometries for sulfur contacts. S_A is the separation in the case of both sulfur atoms adsorbing at terrace sites; S_B is the separation for one sulfur atom adsorbing at a terrace site and the other at a step edge site; S_C is the separation for both sulfur atoms adsorbing at step edge sites. Reprinted with permission from Haiss *et al.*[69] Copyright (2009) American Chemical Society.

They confirmed their conclusions by performing the measurements on different surface morphologies of the substrate. They found that the higher conductance groups dominated on rough surfaces, whereas lower conductance groups dominated on atomically flat surfaces. Furthermore, analysis of the respective break off distances for each conductance group showed the expected trend, with the lowest conductance groups having the longest break of distances.

2.1.2   Attenuation With Molecular Length

Many groups have studied the change in transport characteristics with increasing molecular length in the coherent regime, and attenuation factors for a variety of systems have been reported. One relatively early example of such a study by Wold *et al.* in 2002 focused on the differences in the distance dependence characteristics of saturated versus unsaturated systems. They studied SAMs of oligophenylene thiolates and alkanethiolates on a gold surface using an AFM. The results demonstrated a much weaker dependence of resistance on molecular length for unsaturated ($\beta \approx 0.42$ Å^{-1}) compared with saturated systems ($\beta \approx 0.94$ Å^{-1}). This result can be rationalised by considering the increased orbital overlap present within unsaturated molecules. Choi *et al.* have demonstrated similar length dependence of the conjugated polymers oligophenyleneimine (OPI) and oligonaphthalenefluoreneimine (ONI),[70] which they showed to have attenuation factors of 0.3 Å^{-1} and 0.25 Å^{-1}.

Schneebeli and coworkers have investigated the effect of π-stacking on the decay of conductance with increasing carbon-carbon bonds.[71] They studied a series of π-π-stacked benzene rings, held together in eclipsed fashion *via* ethylene bridges (see Figure 2.3), with direct electrode-to-benzene ring connections.
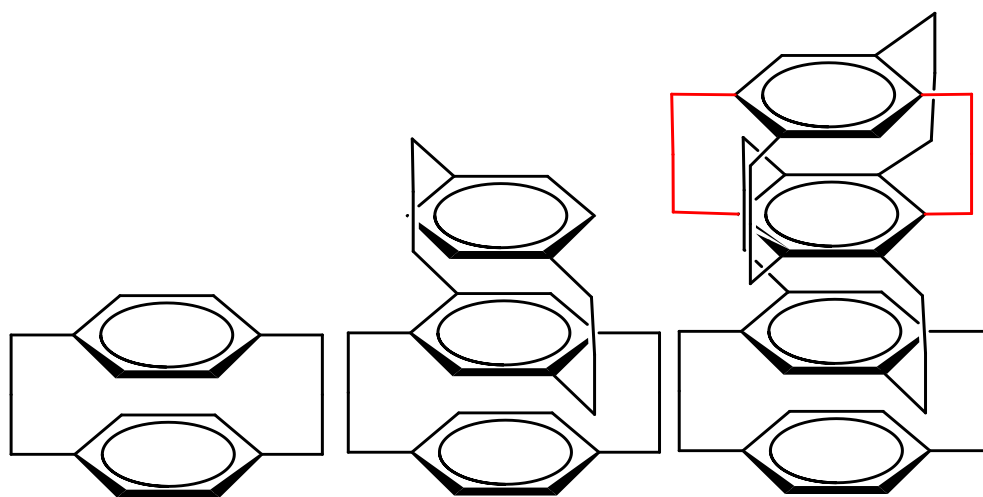

Figure 2.3 The π-stacked molecules studied by Schneebeli *et al.*[71] The four ring analogue was isolated and measured as a mixture of isomers (red and black lines).

They found that the conductance did indeed decay exponentially with increasing number of stacked aromatic rings, supporting a non-resonant tunnelling mechanism of charge transport. The attenuation factor was reported in terms of three factors:

- As a function of the number of stacked benzene rings, giving (1.94 ± 0.25)/stacked benzene ring
- Per Angstrom, using a ring spacing of (3.07 ± 0.02) Å, giving (0.63 ± 0.09)/Å. This is smaller than reported values for alkanes.
- As a function of σ-through bond channel distance, giving a value of ~0.5/(C-C bond).

This latter value is roughly half the magnitude of those previously reported, suggesting that conductance is not solely occurring through the σ channel. They concluded that the conductance channel in which electrons tunnel between the contacting π-π-stacked layers makes a significant contribution to the overall conductance in these systems, and helps reduce the decay with increasing length.

2.1.3 Aims of this Study

Upon introduction of the $I(s)$ method in 2003, Haiss and co-workers measured the conductance of N-hexanethiol disubstituted 4,4'-bipyridine (6V6).[43] It was noted that even though 6V6 is longer than dodecane-1,12-dithiol, it is more conductive. Leary and coworkers proposed that since the frontier orbital energies of the alkyl groups lie far from the Fermi energy of gold, whilst those of the π-system are much closer, the molecule can be regarded as a single molecule equivalent of a double tunnelling barrier (Figure 1.25).[53] In this architecture the two alkyl chains can be thought of as barriers, with the viologen unit acting as a barrier indentation, or well. They went on to show that the presence of a phenyl ring in the middle of an alkyl chain could also serve as an indentation in the tunnelling barrier.

 The magnitude of the conductance in these systems will depend on both the height of the tunnelling barrier and its width, the latter of which is the length of the alkyl chains. The group demonstrated that the conductance of molecules of this type could be gated by using substituents to chemically tune the electronic structure of the barrier indentation.
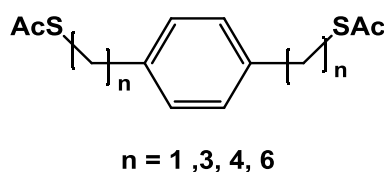

n = 1 ,3, 4, 6

**Figure 2.4 The structure of the series of molecules used in this study.**

The aim in this work is to analyse the effect of the barrier width, or alkyl chain length, on the single molecule conductance and its attenuation with increasing molecular length. The molecules studied consist of a single phenyl ring sandwiched between two alkyl chains comprising 1 (1,4-benzenedimethanethiol, BDMT), 3 (S,S''-(1,4-phenylenebis(propane-1,3-diyl)) diethanethioate, 3Ph3), 4(S,S''-(1,4-phenylenebis(butane-1,4-diyl)) diethanethioate, 4Ph4) and 6 (S,S'-(1,4-phenylenebis(hexane-1,6-diyl))diethanethioate, 6Ph6) methylene units.

2.2   Synthesis

1,4-Benzenedimethanethiol is the only one of the four molecules studied that is commercially available, the remaining three were synthesised from commercially available starting materials.

2.2.1   Synthesis of 6Ph6

The synthesis of the 6Ph6 analogue was a straightforward 3 step procedure, as shown in Scheme 2.1. The first step was a Sonogashira coupling of 1,4-diiodobenzene **2.1** with 6-chlorohex-1-yne, which provided dialkyne **2.2**. Saturation of the triple bonds *via* catalytic hydrogenation, and a subsequent displacement of the terminal chloride using potassium thioacetate yielded the target molecule **2.4**.
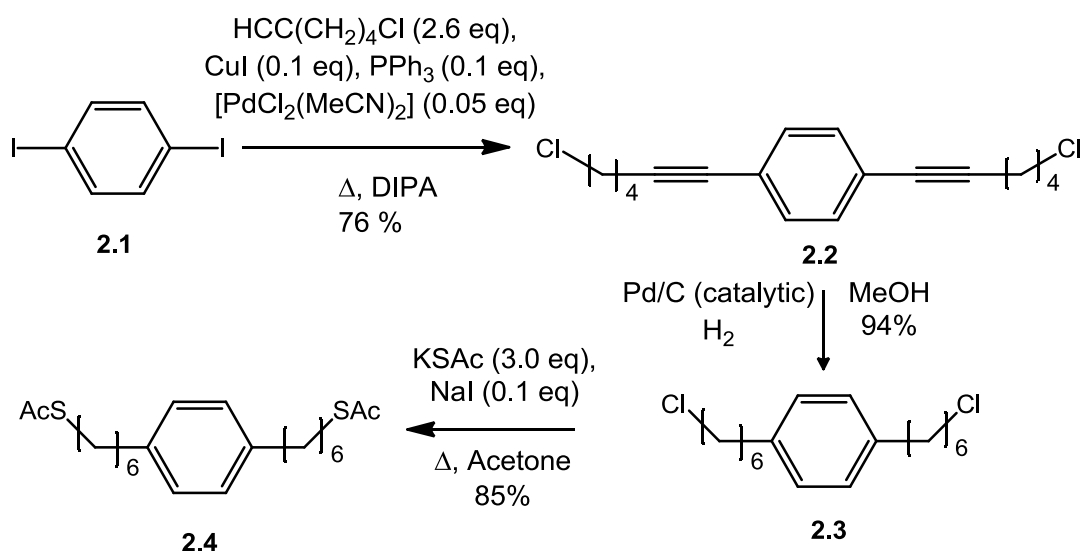

Scheme 2.1 The synthesis of 6Ph6 (2.4).

2.2.2   Synthesis of 4Ph4 and 3Ph3

The synthesis of 3Ph3 and 4Ph4 was more protracted. In the latter case the desired alkyne starting material, 4-chlorobut-1-yne, is not commercially available. In the former case the analogous alkyne would be propargyl chloride, which would itself react with Pd(0) to form a π-allenyl complex, resulting in loss of the chloride-moiety (Scheme 2.2).
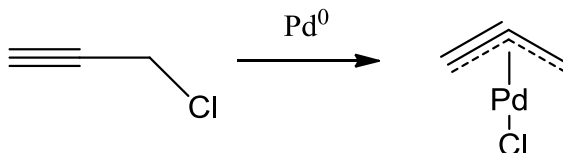
**Scheme 2.2 The formation of a π-allenyl complex from propargyl chloride.**

The Sonogashira coupling in the first step of these two analogues therefore employed terminal alkynes with alcohol moieties on the opposite terminus, yielding dialkynes **2.5** and **2.6**. Subsequent catalytic hydrogenation provided quantitative yields of the analogous saturated primary alcohols **2.7** and **2.8** (Scheme 2.3).

2.5: m = 1, 86%
2.6: m = 2, 78%

2.7: n = 3, 97%
2.8: n = 4, 97%
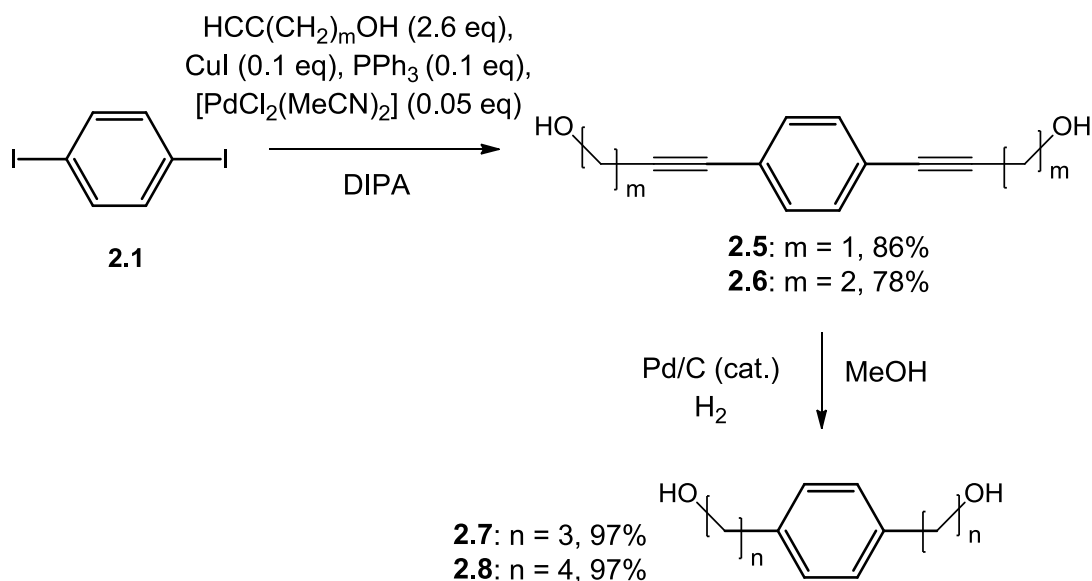
Scheme 2.3 Synthesis of saturated primary alcohols 2.7 and 2.8.

Mitsunobu chemistry was then employed in attempts to convert the terminal alcohols into thioacetate groups. This chemistry uses triphenylphosphine, an azodicarboxylate and a carboxylic acid; in this case the latter two were di*iso*propylazodicarboxylate (DIAD) and thioacetic acid. Whilst the conversion

appeared to proceed without problem, subsequent removal of the triphenylphosphine oxide by-product proved problematic (Scheme 2.4).
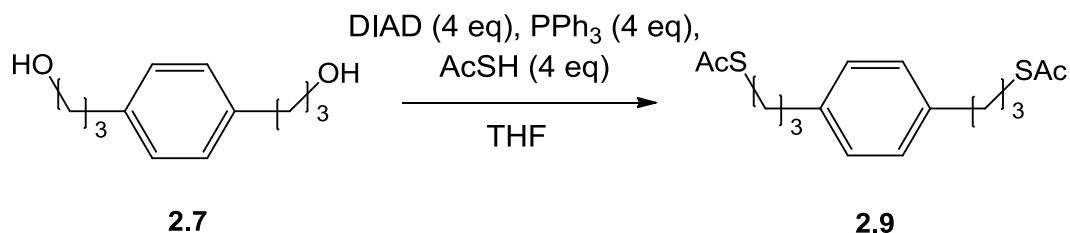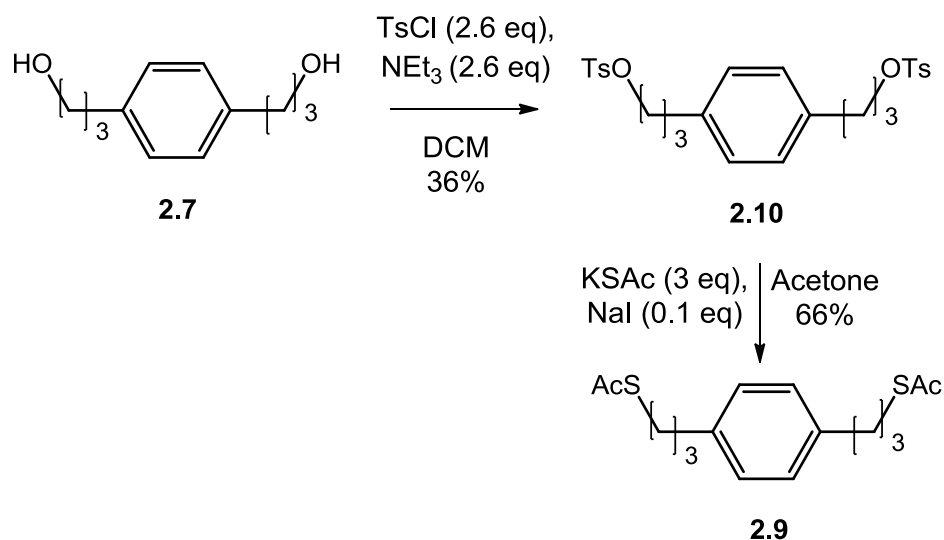

Scheme 2.4 Synthesis of dithioacetate 2.9 using Mitsunobu chemistry.

O'Neil and coworkers have reported a modified procedure aimed at alleviating the purification problems associated with the production of triphenylphosphine oxide as a by-product.[72] They replaced triphenylphosphine with 1,2-bisdiphenylphosphinoethane (DPPE); the by-product thus formed is diphenylphosphinoethane dioxide, which is completely insoluble in some organic solvents and can be removed by filtration. Attempts at utilising this chemistry showed no evidence of any conversion (Scheme 2.5), a result that concurred with previous attempts to employ sulfur nucleophiles in this modification.
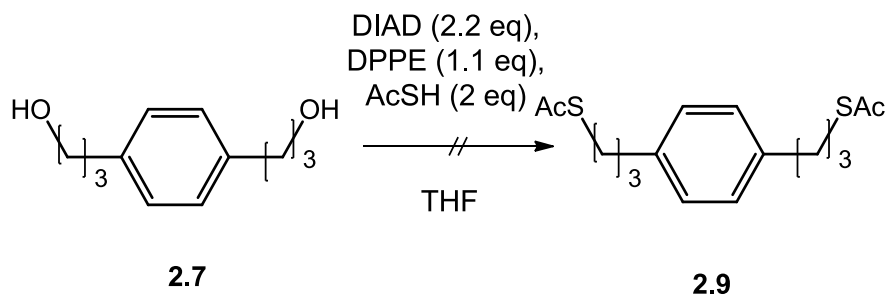
Scheme 2.5 Attempt to synthesise dithioactetae 2.9 using a filterable phosphine source.

Since attempts to directly convert the alcohol to the required thioacetate moiety proved fruitless, conversion of the alcohol groups into suitable leaving groups was investigated. The reaction of 1,4-phenylenebis(propan-1-ol) **2.7** with *p*-tosyl chloride in the presence of triethylamine yielded the desired bis-tosylate; subsequent displacement of the tosyl groups provided the target molecule, 3Ph3 (**2.9**). Whilst the final displacement reaction showed a good conversion yield, the penultimate tosylation reaction proceeded in disappointing yield (Scheme 2.6).

**Scheme 2.6 Tosylation and displacement to yield dithioacetate 2.9.**

Replacement of the alcohol groups with bromides was investigated in the synthesis of 4Ph4, a conversion which is often achieved using triphenylphosphine in the presence of a bromine source, commonly carbon tetrabromide. However, this chemistry again produces triphenylphosphine oxide and can therefore present similar purification problems as those seen previously.

	Solvent	Bromine Source	Yield (%)	Comments
1	DCM	NBS	-	$Ph_2POCH_2CH_2POPh_2$ in product
2	Et_2O	NBS	-	No product
3	THF	NBS	42%	$Ph_2POCH_2CH_2POPh_2$ precipitates
4	THF	$BrCl_2CCCl_2Br$	71%	$Ph_2POCH_2CH_2POPh_2$ precipitates

Table 2.2 Optimisation of the bromination of compound 2.8.

Pollastri and coworkers have shown that this chemistry can also be modified to use DPPE in place of triphenylphosphine,[73] resulting in good conversion and an insoluble phosphine by-product that can be filtered off. This chemistry was investigated using different solvents and bromine sources; as can be seen from Table 2.2 the optimum results were achieved using dibromotetrachloroethane in THF and gave 71% yield of the product. The subsequent displacement reaction also

proceeded in good yield, thus providing a much improved pathway to these analogues (Scheme 2.7).
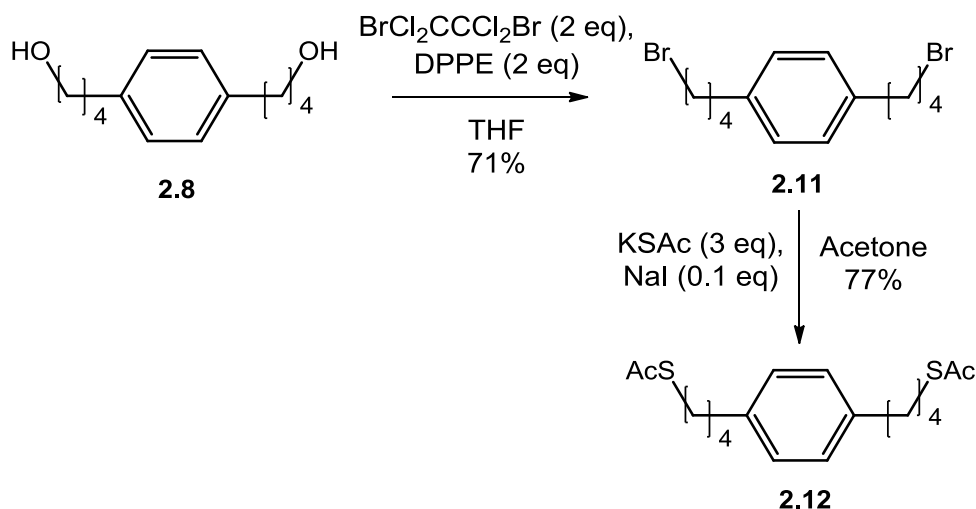

Scheme 2.7 Optimised procedure for the synthesis of dithioacetate 2.12.

2.2.3 Synthesis of 8Ph8

The synthesis of 8Ph8 was perhaps the most challenging, due to a lack of suitable commercially available starting alkynes. One possible pathway was to employ the nickel catalysed Kumada coupling to cross couple a suitable Grignard reagent with diiodobenzene **2.1**. Since the precursor to the Grignard reagent should contain only one halo group, the inclusion of an alcohol group on this molecule is desirable to provide a means of incorporating the thioacetate moiety in the final compound. However, alcohol groups are generally incompatible with Grignard reagents and their protection is therefore necessary.

Attempts to employ silyl protecting groups did not yield the desired result. The benzyl protecting group was chosen as it is robust and easily cleaved. Benzyl bromide is most commonly used in order to incorporate this moiety and an alkoxide is required, bromooctanol could therefore not be used. Instead octanediol **2.13** was treated with sodium hydride and benzyl bromide, yielding the monoprotected octanol **2.14**. The bromination of **2.14** was achieved using the chemistry discussed previously, and provided the benzyl protected bromooctanol **2.15** in good yield (Scheme 2.8).
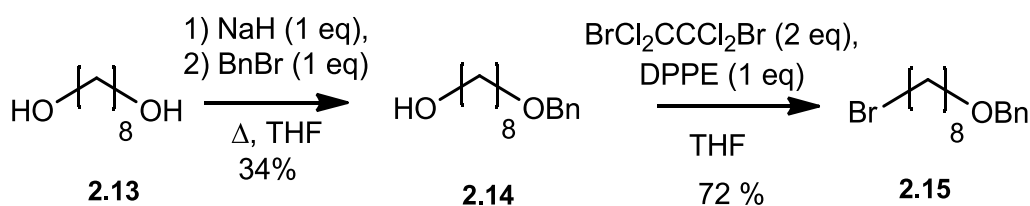
Scheme 2.8 Monoprotection of octanediol 2.13 and subsequent bromination to 2.15.

Attempts to cross couple diiodobenzene **2.1** with the Grignard reagent formed from **2.15** in diethyl ether failed, it was postulated that this may be due to the low solubility of the starting materials in diethyl ether. However, subsequent attempts using THF also failed to yield the desired product.
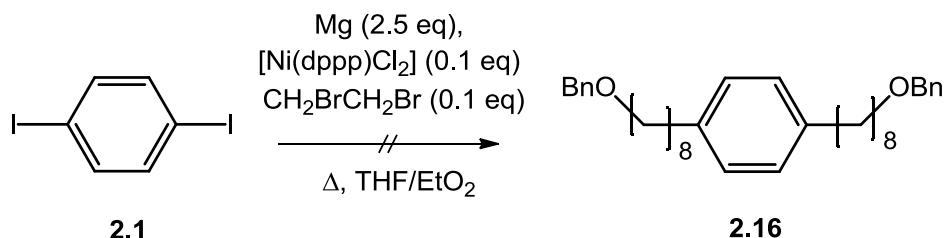
	Solvent	Initiator	Result
1	THF	DBE, heat, sonication	Isolated S.M.
2	EtO$_2$	DBE, heat, sonication	Mg did not dissolve
3	THF	DBE, sonication, reflux o/n	Isolated BnOC$_8$H$_{17}$

Figure 2.5 Attempts to cross couple diiodobenzene 2.1 with a Grignard reagent to synthesise compound 2.16.

Since exploring alternative metal couplings proved laborious it was decided to synthesise a suitable alkyne precursor. Previous syntheses of such an alkyne involved acetylene deprotonation and trapping out with a dihalogenated alkane chain.[74] However, attempts to repeat this synthesis using commercially available sodium acetylide proved unsuccessful. A further option demonstrated by Krasinski and coworkers employed trimethylsilyl (TMS) acetylene,[75] which was deprotonated *in situ* and trapped out with chloroiodohexane (Scheme 2.9). Whilst this synthesis provided the desired eight carbon chain, the product contained a mixture of the chloro- and iodo- analogues, the latter of which could provide a competing reaction pathway in the subsequent Sonogashira coupling.

Scheme 2.9 Attempt to synthesise alkyne 2.19 *via* deprotonation of TMS-acetylene with BuLi and trapping out of the resulting lithio-species with chloroiodohexane to give alkyne 2.18, which was subsequently deprotected with K$_2$CO$_3$/MeOH.

In order to avoid this problem an alcohol moiety was again included to provide a means of introducing the thioacetate group in the final stages of the synthesis. Since free hydroxyl groups are incompatible with butyl lithium a benzyl protecting group was employed; this was the protecting group of choice as it can be cleaved under hydrogenation conditions and will therefore be removed during the reduction of the alkyne triple bond.

The synthetic pathway first saw the monoprotection of hexanediol **2.20** *via* treatment with sodium hydride and benzyl bromide; subsequent bromination using the previously optimised procedure provided benzyl protected bromohexanol **2.22** in good yield (Scheme 2.10). This was then used to trap lithium trimethylsilyl acetylide, which had been generated *in situ* (Scheme 2.11).
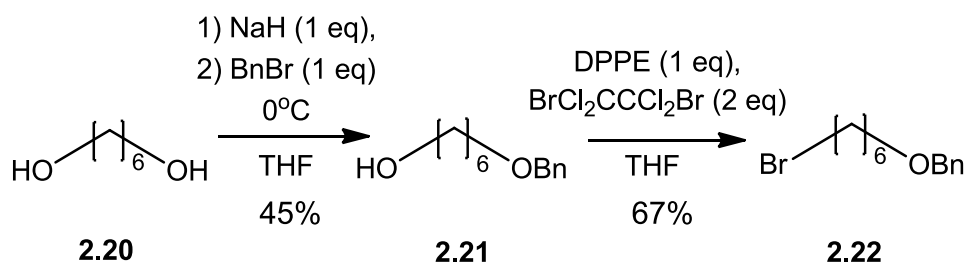
Scheme 2.10 Treatment of hexanediol 2.20 with sodium hydride and benzyl bromide gave monoprotected alcohol 2.21, subsequent bromination provided compound 2.22 in good yield.
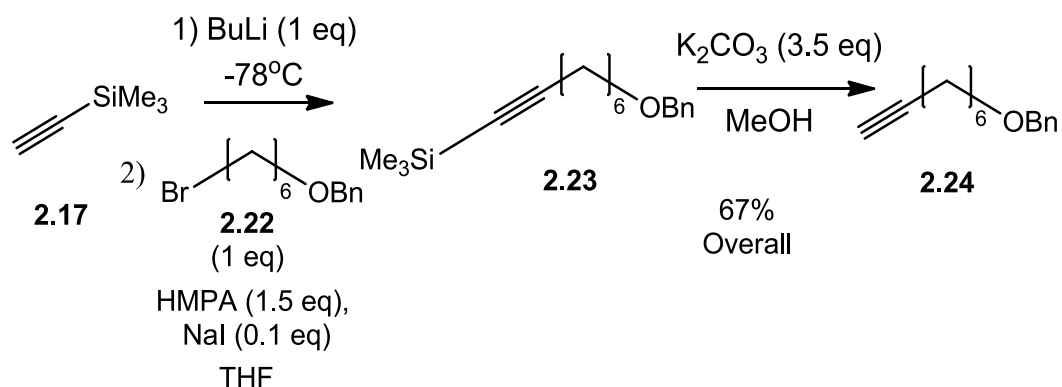
Scheme 2.11 The lithiation of TMS-acetylene and reaction of the resulting anion with benzyl bromide. Subsequent deprotection using MeOH/K$_2$CO$_3$ yielded compound 2.24 in over 67% yield.

The desired product **2.24** was isolated in 67% overall yield, however attempts to employ this alkyne in the subsequent Sonogashira coupling proved problematic. The monosubstitution appeared to proceed with ease; however the second coupling was much less successful. The reaction was heated for extended periods in order to allow ample time for reaction. Unfortunately the competing homo-coupling of two alkyne units prevailed, presumably due to oxygen leaking into the flask over the extended reaction time. Due to time restrictions further work on the synthesis of this analogue was not possible.

2.3 SAM Preparation and Characterisation

2.3.1 Preparing a SAM on a Au(III) Surface

Commercially available gold-on-glass substrates were used throughout this work. Prior to monolayer adsorption the substrate is flame annealed in order to obtain flat areas, or terraces, on the gold surface. This is important because molecules adsorbed at step edges have been shown to have a higher conductance to those adsorbed at a terrace site.
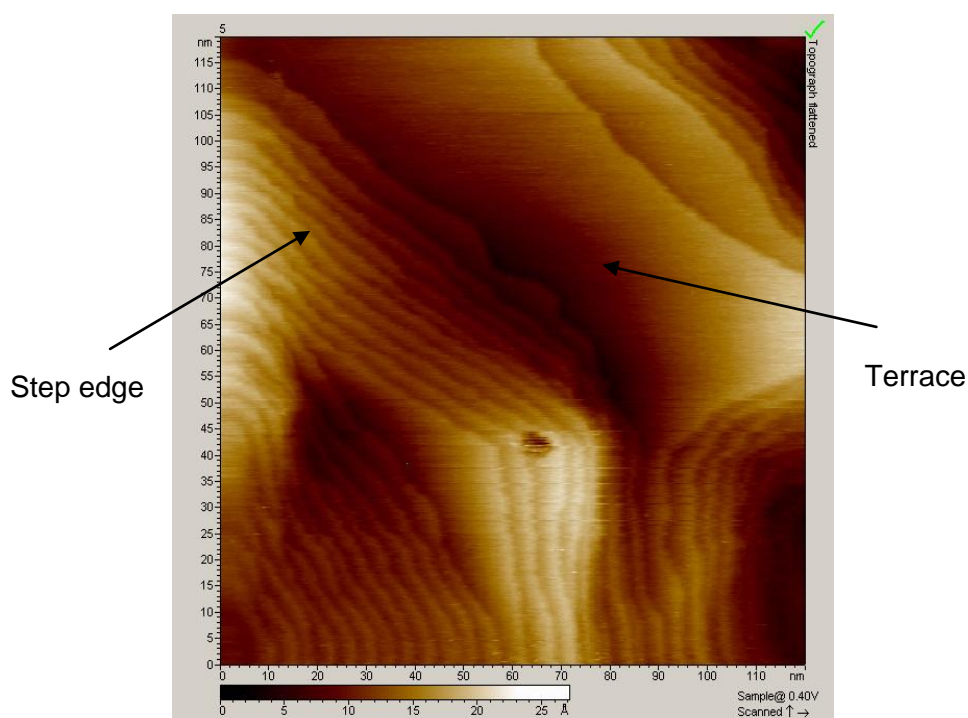

Step edge

Terrace

Figure 2.6 Image of a flame annealed Au(III) surface, acquired at 0.4V with a set point of 0.1nA, showing both step edges and terrace sites.

The sample is then immersed in a solution of the molecule in order to allow adsorption; the immersion time depends on both the stability of the monolayer and the extent of monolayer coverage required. For conductance measurements a low coverage monolayer is required and the immersion time is in the region of a few minutes, whereas for PM-IRRAS experiments a high coverage monolayer is necessary and overnight immersion is required.

2.3.2   Characterisation of the Monolayers

2.3.2.1   PM-IRRAS

A PM-IRRAS spectra of a SAM of 6Ph6 on Au(III) was obtained and is shown in Figure 2.7. Whilst the acquisition of a PM-IRRAS spectrum removes any peaks arising from the atmosphere, it does not take into account absorbance that may arise from the gold slide itself. For this reason a bare gold background spectrum is acquired and subtracted from each monolayer measurement prior to plotting the final spectrum, this ensures that any observed peaks are due to the molecules adsorbed onto the surface of the substrate.
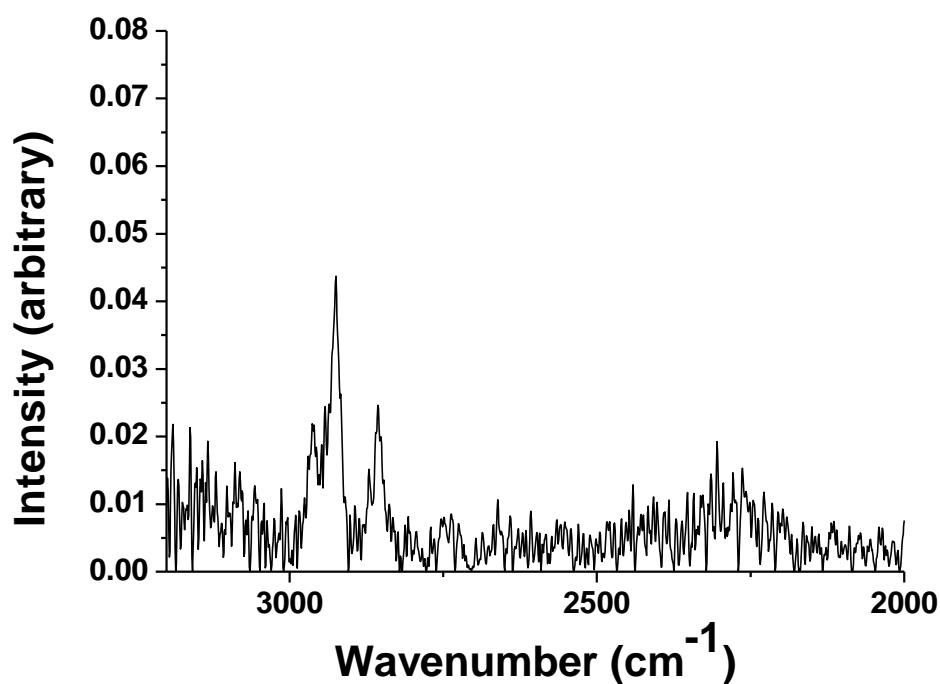

Figure 2.7 A PM-IRRAS spectrum of a monolayer of 6Ph6 on Au(III).

Clear peaks can be seen at around 2924cm^{-1} and 2856cm^{-1}, these correspond to the asymmetric and symmetric stretches of CH_2 groups, respectively. This provides good evidence that the molecule adsorbs onto the surface of the substrate.

2.3.2.2   STM Imaging

STM images of low coverage monolayers of bare gold, 4Ph4 and 6Ph6 are shown in Figure 2.8. Since the adsorbed molecules are mobile on the gold surface true molecular resolution cannot be achieved. However, the molecules may be appearing as bright dots on the surface.
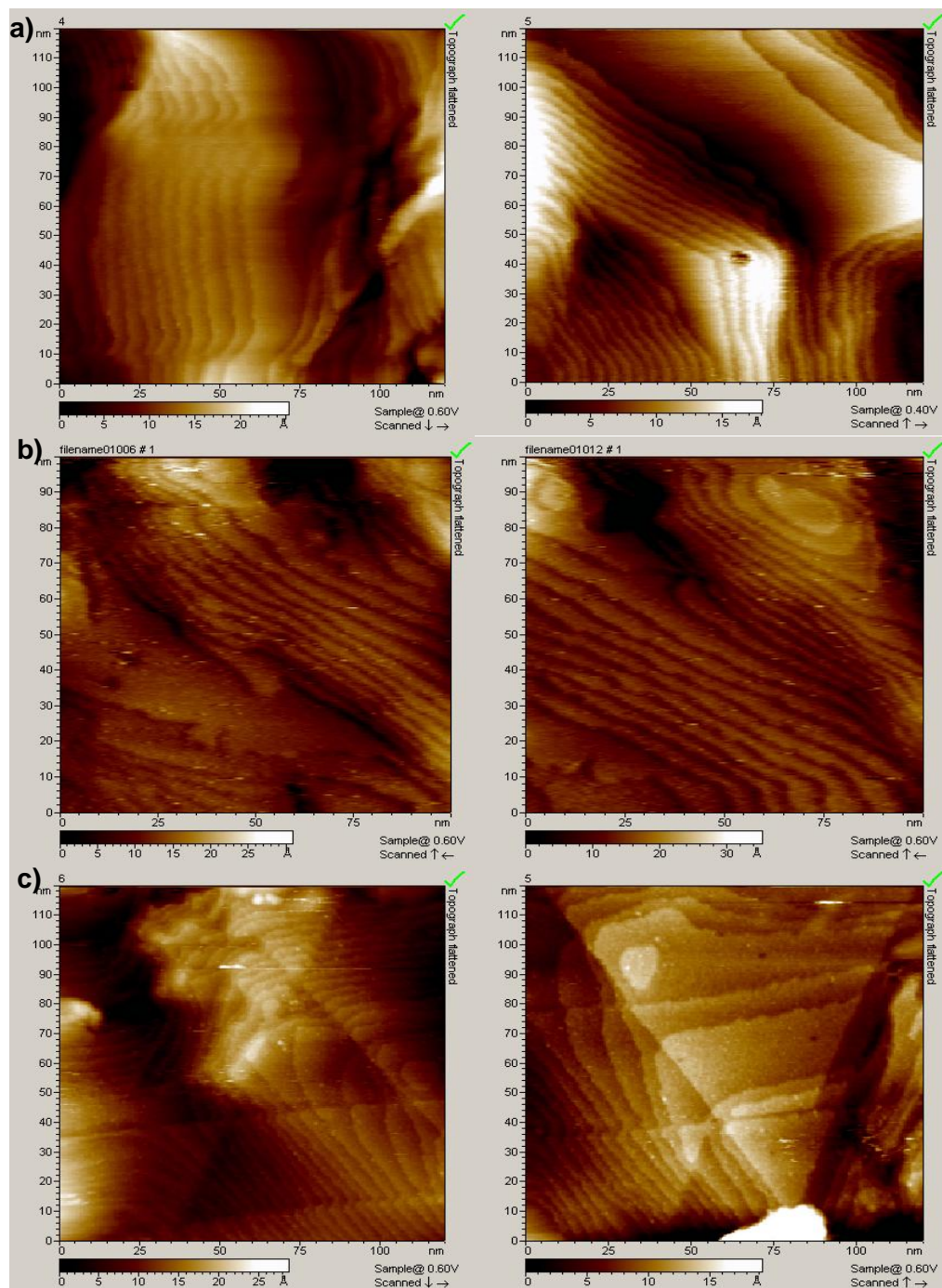

Figure 2.8 STM images of a) a bare gold surface b) a low coverage monolayer of 4Ph4 and c) a low coverage monolayer of 6Ph6.

2.4 Single molecule conductance measurements

All single molecule conductance measurements were performed using the *I(s)* STM method at a bias of 0.6 V. The set point was varied in order to account for the different lengths of the molecules. Two data sets were acquired for each molecule, each using a different set point current. This was done in order to allow the observation of different conductance groups. The set point for the high conductance of 6Ph6 was the same as that used by Leary *et. al.*, but was increased for shorter molecules to ensure a good probability of junction formation. Set points a factor of ten lower were used to measure lower conductance groups. A description of the experimental details can be found in Chapter 5.

2.4.1 Low Conductance

The conductance of 6Ph6 was measured using a set-point of 0.6 nA. A histogram of the conductance versus count is shown in Figure 2.9(a). The conductance was determined to be (0.04 ± 0.01) nS using equation 1.12. It was noted that this conductance value is lower than that reported by Leary and co-workers, which was (0.74 ± 0.24) nS.[53] The relevance of this finding is discussed in section 2.6. A second, broader peak can also be seen at approximately double the current of the first one; this was attributed to a molecular junction containing two molecules.
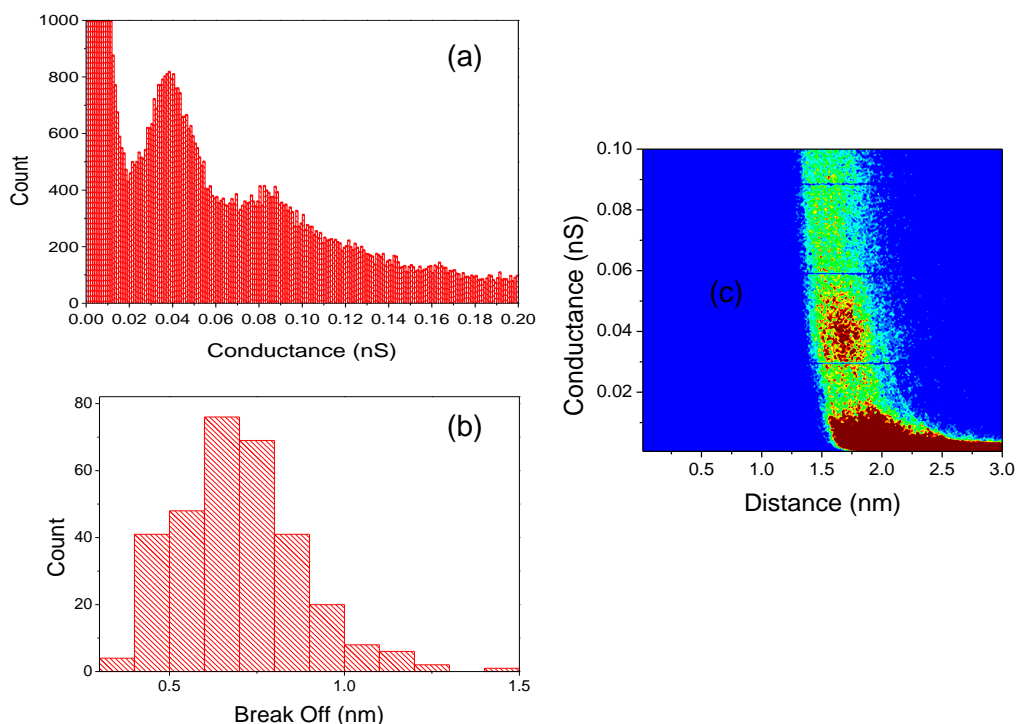

Figure 2.9 Data for 6Ph6 U$_{bias}$ = 0.6 and I$_{set}$ = 0.6nA (a) Histogram of 500 I(s) scans (b) Histogram of the experimental break-off distances (c) 2D histogram showing conductance versus total break-off distance.

Figure 2.9(b) shows a histogram of the experimental break-off distances, which were analysed by hand, and gave an average of (0.7 ± 0.17) nm. The S_0 calibration value was estimated to be (1.14 ± 0.05) nm, giving a total break-off distance of (1.84 ± 0.22) nm. The Au-Au separation calculated within Spartan® was approximately 2.2 nm for the fully extended molecule with alkyl chains in the fully anti form and the thiols bonded to Au(I) ions. When taking into account the stochastic nature of the junction breaking process, particularly for longer molecules, the relatively good agreement of experimental break-off distance and the predicted molecular length provide good evidence that single molecule junctions are indeed forming. The data can also be represented in a 2D histogram (Figure 2.9(c)); these are plotted as conductance *vs.* total break-off distance and use a colour gradient to demonstrate the most likely conductance value as well its corresponding break-off distance (including S_0).

A slightly higher set-point current of 1 nA was used to measure the conductance of 4Ph4 in order to account for its shorter molecular length; the data is presented in Figure 2.10. The conductance was determined to be (0.08 ± 0.02) nS. The S_0 value and average experimental break off distance were calculated to be (1.19 ± 0.13) nm and (0.67 ± 0.16) nm respectively, giving an estimated total break-off distance of (1.86 ± 0.29) nm. This is again in good agreement with the value estimated using Spartan®, which in this case was approximately 1.9 nm for the fully extended molecule as described for 6Ph6.
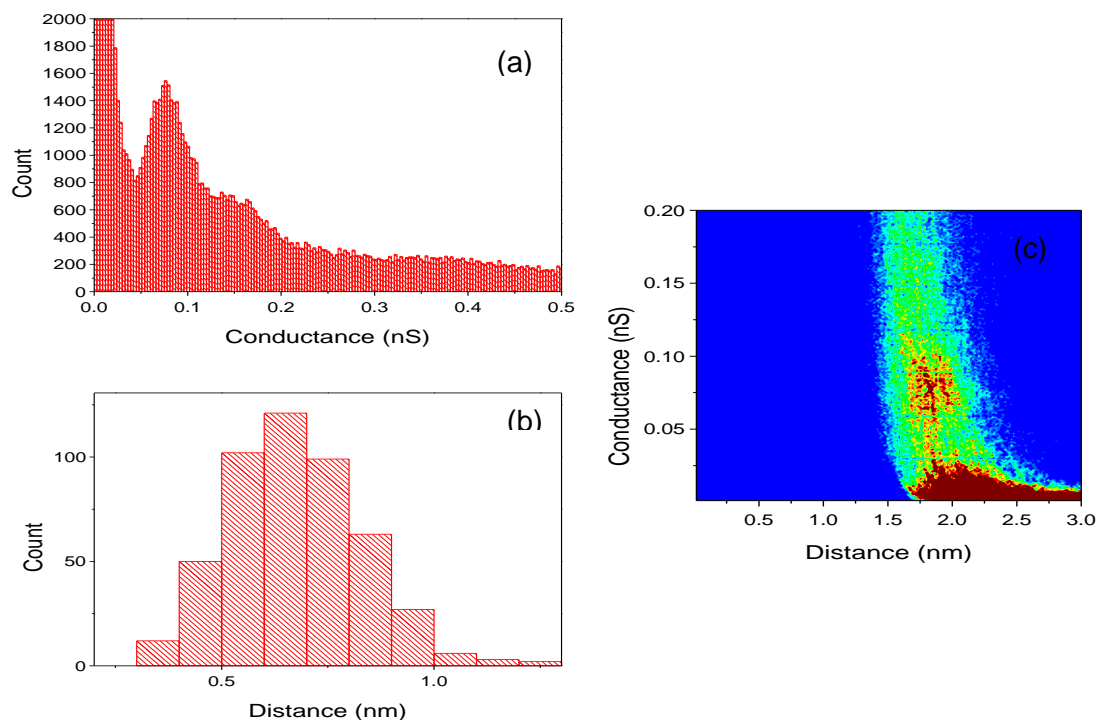

Figure 2.10 Data for 4Ph4 U_{bias} = 0.6 and I_{set} = 1nA (a) Histogram of 500 I(s) scans (b) Histogram of the experimental break-off distances (c) 2D histogram showing conductance versus total break-off distance.
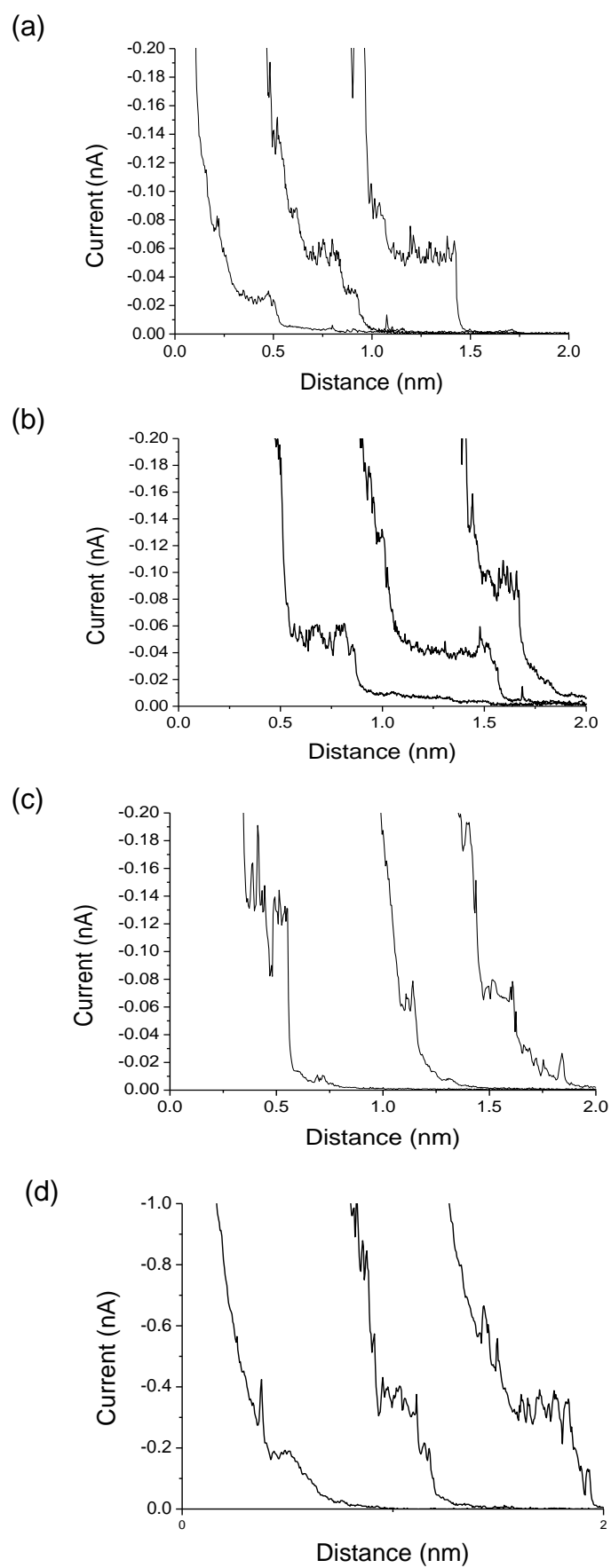
Figure 2.11 Example I(s) traces of (a) 6Ph6 (b) 4Ph4 (c) 3Ph3 and (d) BDMT (distance scale is relative and does not represent actual break-off distance).

The probability of forming a molecular junction (hit rate) was much lower in the 4Ph4 data acquisition, therefore a set point of 2 nA was employed in the measurement of 3Ph3; the data for these measurements is shown in Figure 2.12. The single molecule conductance was found to be (0.12 ± 0.02) nS. A second, broader peak can be seen at around twice this value and can be attributed to two molecules bridging the tip-substrate gap. The broader nature of this peak is due to the wider range of contacts available when two molecules bridge the tip-substrate gap. The experimental break-off distance was determined to be (0.69 ± 0.86) nm, which when added to the S_0 value gave an estimated total break-off distance of (1.55 ± 0.21) nm. This value is in good agreement with the Spartan® predicted Au-Au separation of 1.6 nm for this molecule, calculated as previously described.
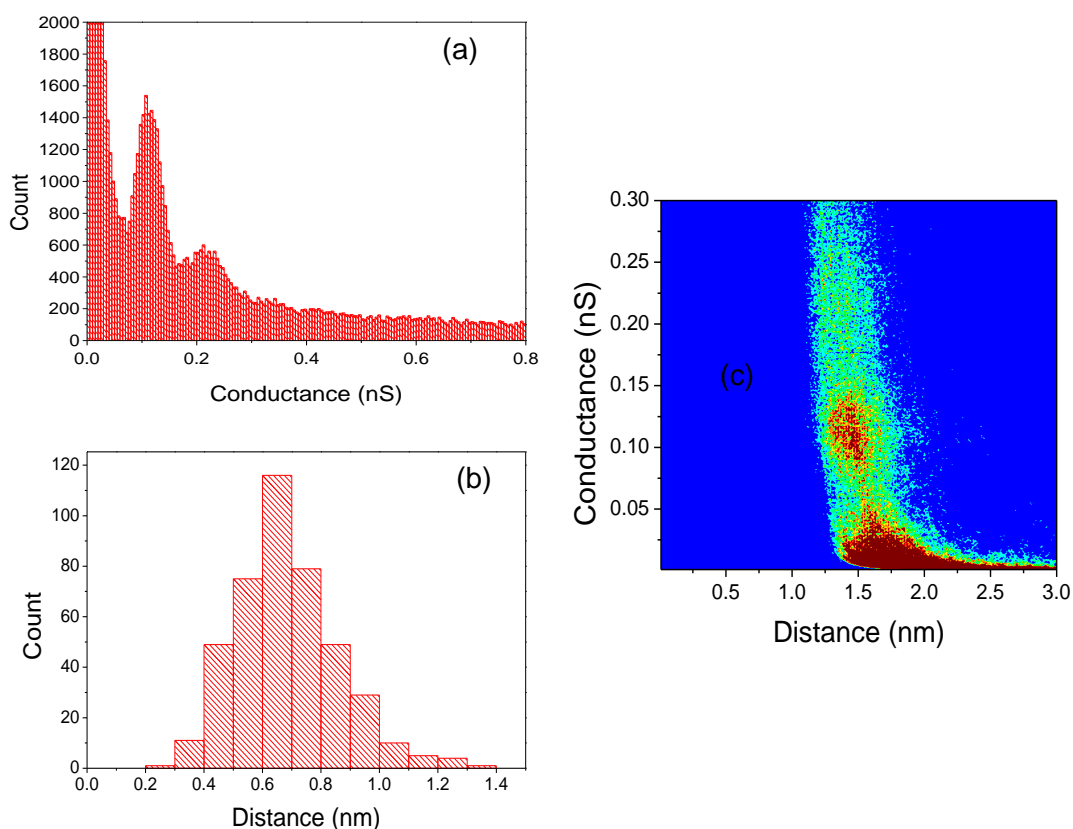

Figure 2.12 Data for 3Ph3 U_{bias} = 0.6 and I_{set} = 2nA (a) Histogram of 500 I(s) scans (b) Histogram of the experimental break off distances (c) 2D histogram showing conductance versus total break-off distance.

The final molecule to be measured in the series was 1,4-benzenedimethanethiol (BDMT). The proportion of molecular junctions formed during the conductance measurements of this molecule was much smaller than for the previous analogues, this is most likely due to its relatively short molecular length. However, statistical analysis was able to provide a single molecule conductance value of (0.3 ± 0.06)

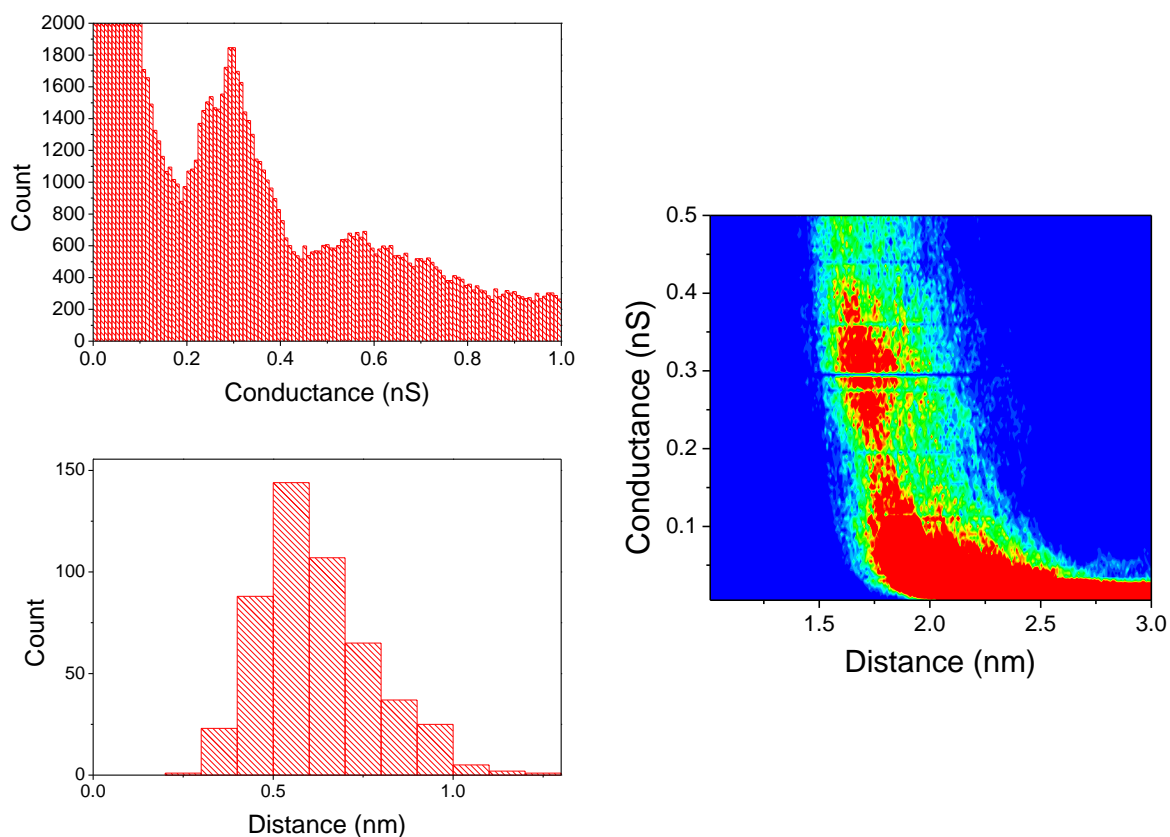nS. Furthermore, a very broad peak can also be seen in the histogram at twice this value (Figure 2.13).

Figure 2.13 Data for BDMT U$_{bias}$ = 0.6 and I$_{set}$ = 3nA (a) Histogram of 500 I(s) scans (b) Histogram of the experimental break-off distances (c) 2D histogram showing conductance versus total break off distance

The low conductance data for the four analogues is summarised in Table 2.3; this shows that the conductance values decay exponentially with increasing length. From equation 1.5 it can be seen that in order to quantify the attenuation factor, β, a plot of ln(conductance) *vs* length is required.

Molecule	Conductance, σ (nS)	Spartan® Au-Au (nm)	Estimated Break-off (nm)
BDMT	0.3 ± 0.06	1.4	1.62 ± 0.28
3Ph3	0.12 ± 0.02	1.6	1.55 ± 0.21
4Ph4	0.08 ± 0.02	1.9	1.86 ± 0.29
6Ph6	0.04 ± 0.01	2.2	1.84 ± 0.22

Table 2.3 Summary of the low conductance data, measured using U$_{bias}$ = 0.6V and various set-points.

The attenuation factor can be determined as a function of three different molecular characteristics:

- Number of methylene units – this is the simplest of the three methods and sees ln(σ) plotted against the number of methylene units, giving the attenuation per methylene unit
- Through bond (TB) length – the sum of all the bond lengths involved in the shortest route from Au to Au (example see Figure 2.14) is plotted against ln(σ), giving the attenuation factor per Ångstrom
- Molecular length – the Au-Au separation is determined using Spartan$^®$, the molecule is drawn in the most extended conformation and energy minimized using the molecular mechanics implementation. This again gives the attenuation factor per Ångstrom
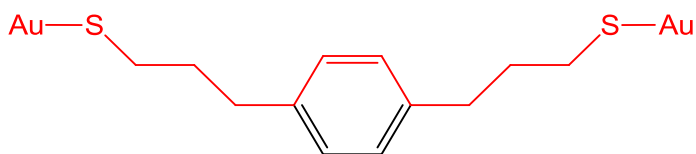

Figure 2.14 The structure of 3Ph3 - the bonds shown in red are included in the calculation of the through bond length

The plots for each of these characteristics are shown in Figure 2.15. Linear regression is used to determine the slope, and therefore attenuation factor for each plot. The results are as follows:

- Attenuation per methylene unit – 0.21
- Attenuation per Ångstrom (through bond) – 0.13
- Attenuation per Ångstrom (Au-Au separation) - 0.24

All three values are much less than expected, they are in fact similar to those values determined in the highly conjugated systems discussed in section 2.1.1. Discussion of the significance of this finding is deferred to section 2.6.
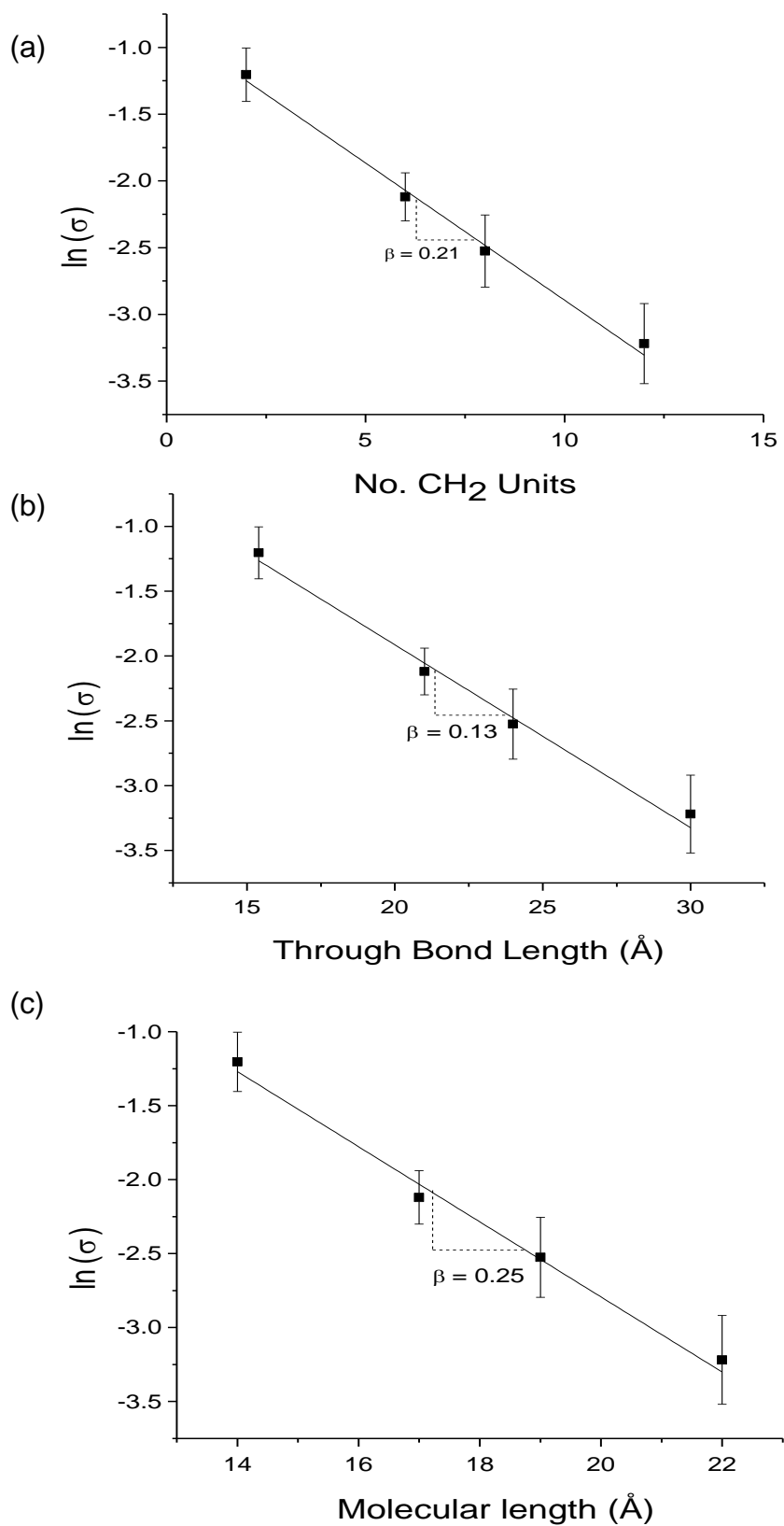
Figure 2.15 Plots of ln(σ) vs (a) number of methylene units (b) through bond length and (c) Molecular length determined using the Au-Au distance computed using Spartan®.

2.4.2   High Conductance

The conductance of all the analogues was measured at a second, increased set-point in order to try and observe higher conductance groups. Again, the set-points were varied between molecules in order to account for differences in molecular length.
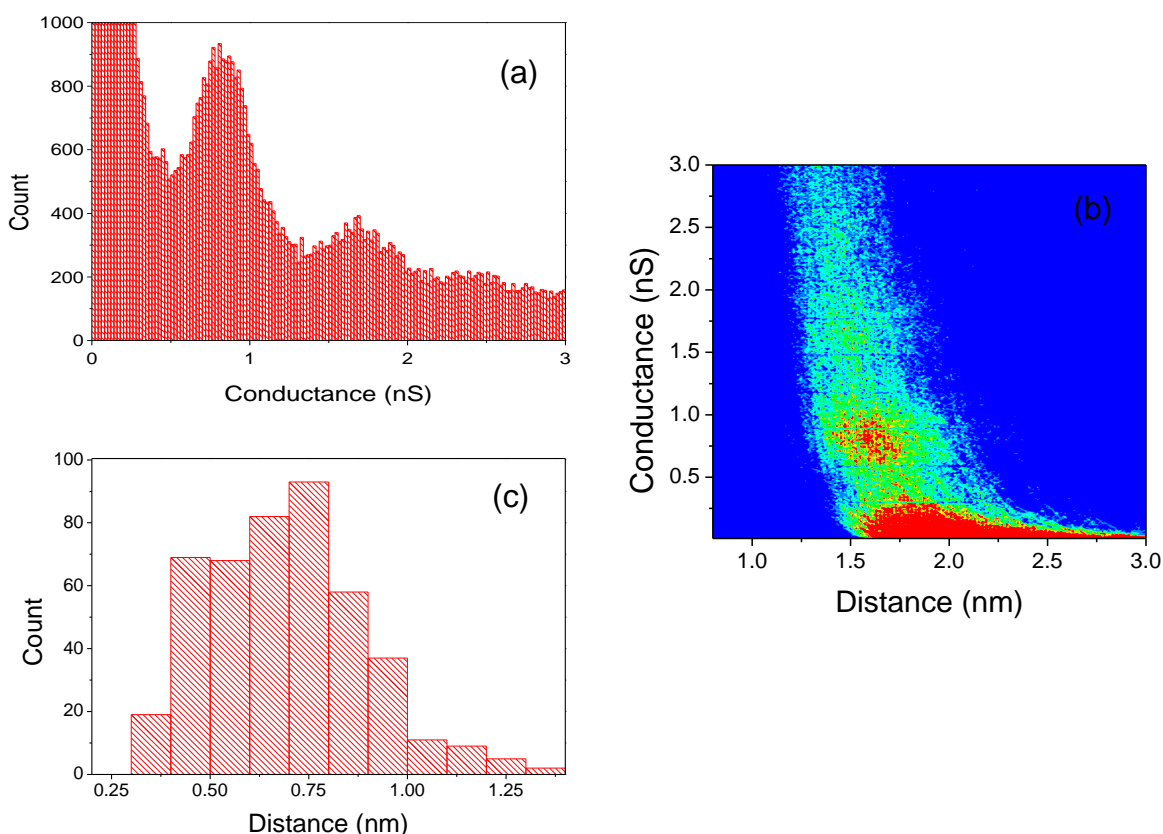

Figure 2.16 Data for 6Ph6 U_{bias} = 0.6 and I_{set} = 6nA (a) Histogram of 500 I(s) scans (b) Histogram of the experimental break-off distances (c) 2D histogram showing conductance versus total break-off distance.

I(s) measurements of the 6Ph6 analogue were performed using a set-point of 6nA, and produced a relatively sharp peak indicating a conductance of (0.82 ± 0.18) nS; this is in good agreement with the value of (0.74 ± 0.24) nS reported by Leary *et al.*[56] A second clear peak can also be seen at a current of approximately twice this value (Figure 2.16(a)), the relatively high intensity of this peak suggests that the set-point was high enough to make multiple junction formation more likely. The total break-off distance for this data set was calculated to be (1.70 ± 0.31) nm.
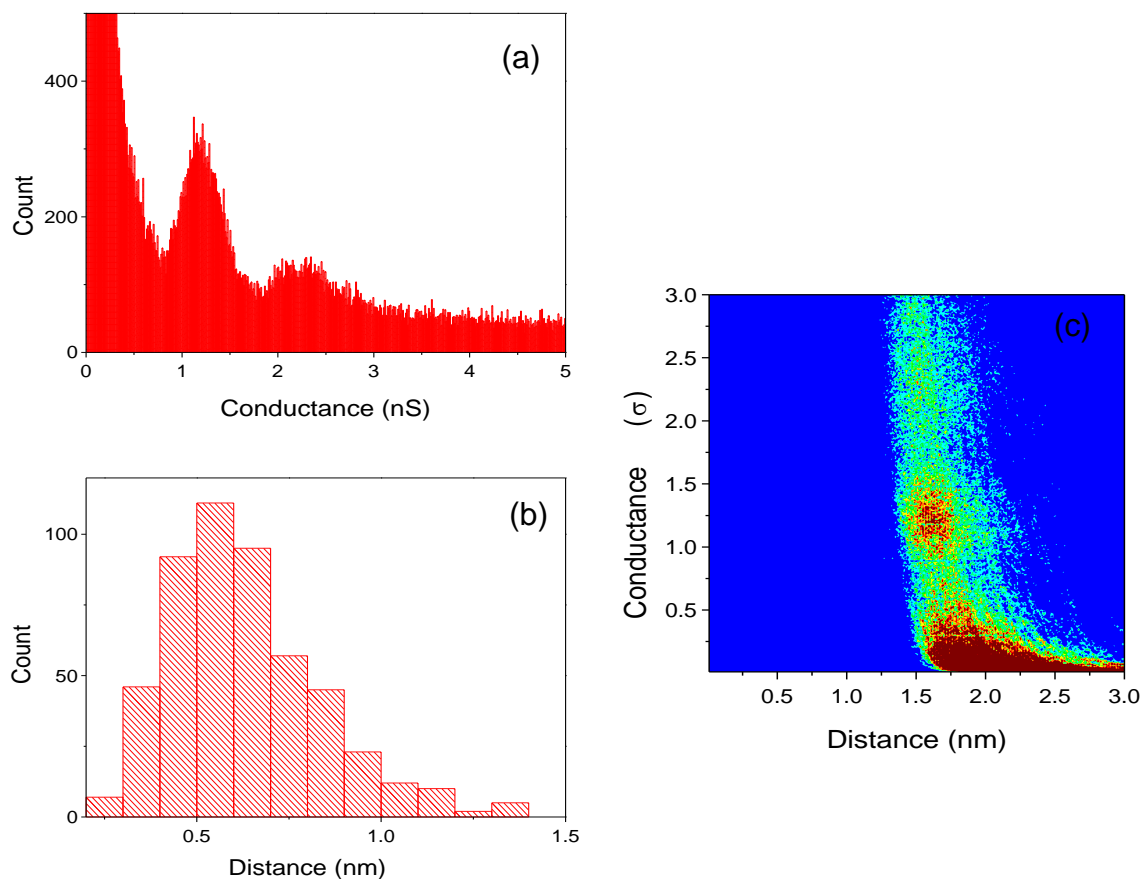
Figure 2.17 Data for 4Ph4 U_{bias} = 0.6 and I_{set} = 10nA (a) Histogram of 500 I(s) scans (b) Histogram of the experimental break off distances (c) 2D histogram showing conductance versus total break off distance.

The data acquired for 4Ph4 is shown in Figure 2.17 and provided a conductance value of (1.21 ± 0.19) nS, furthermore a broad peak can be seen in the histogram at approximately twice this value, although this peak is not as well defined as the one seen in the 6Ph6 data set. The total break-off distance for these measurements was calculated to be (1.5 ± 0.31) nm.

Figure 2.18 shows some example *I(s)* traces for each molecule acquired as described above.

Figure 2.19 shows the data for 3Ph3, which gave a conductance value of (2.01 ± 0.32) nS. The histogram does not show a second peak, suggesting that the junctions were particularly difficult to form. The break-off distance was calculated to be (1.43 ± 0.28) nm.
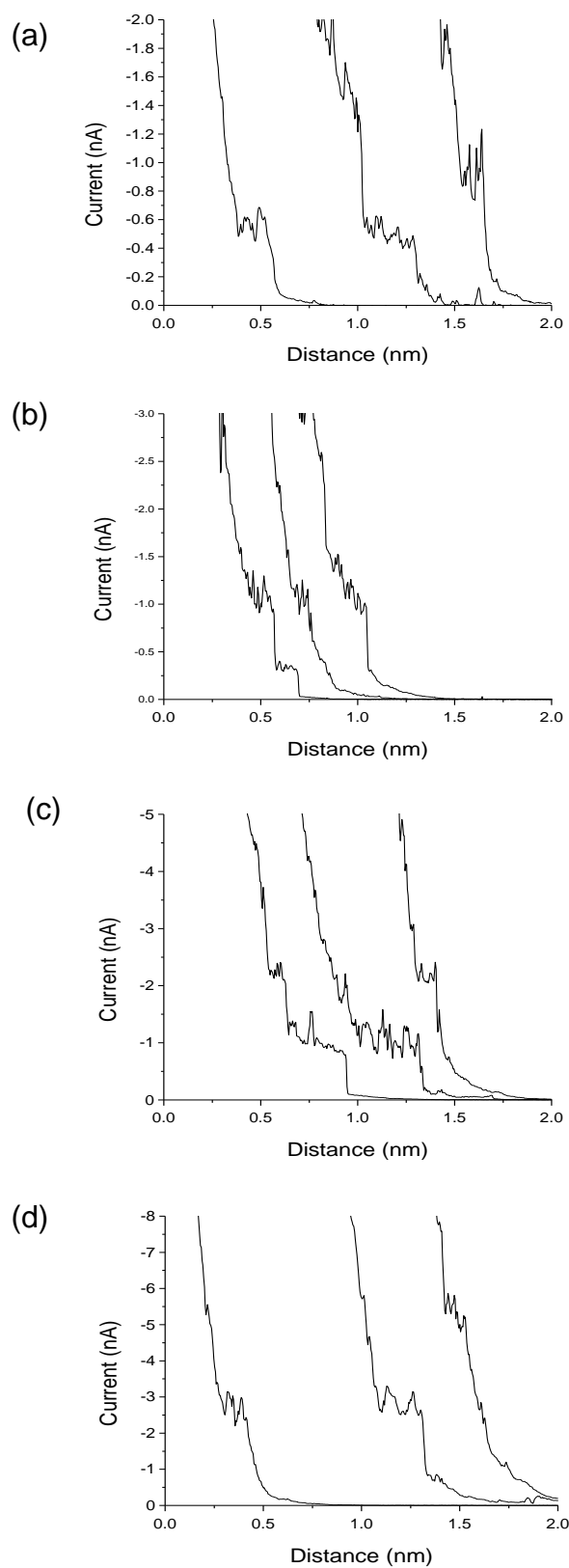
Figure 2.18 Example I(s) traces of (a) 6Ph6 (b) 4Ph4 (c) 3Ph3 and (d) BDMT (distance scale is relative and does not represent actual break-off distance).

Figure 2.19 Data for 3Ph3 U_{bias} = 0.6 and I_{set} = 20nA (a) Histogram of 500 I(s) scans (b) Histogram of the experimental break off distances (c) 2D histogram showing conductance versus total break-off distance.

The final data set is shown in Figure 2.20 and gave a conductance value of (4.14 ± 0.58) nS for BDMT. A second peak was not seen in this data, again this shows the difficulty of forming these junctions. The total break-off distance for these measurements was calculated to be (1.44 ± 0.33) nm.
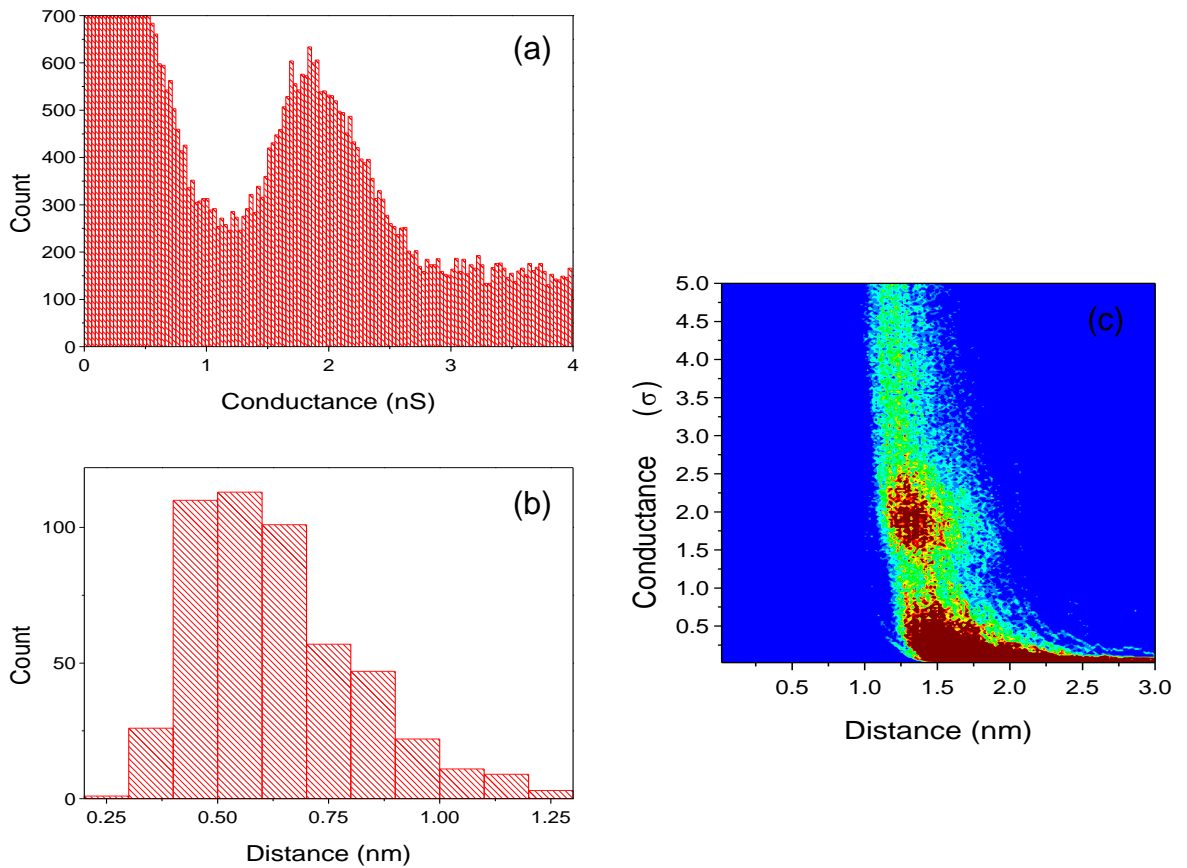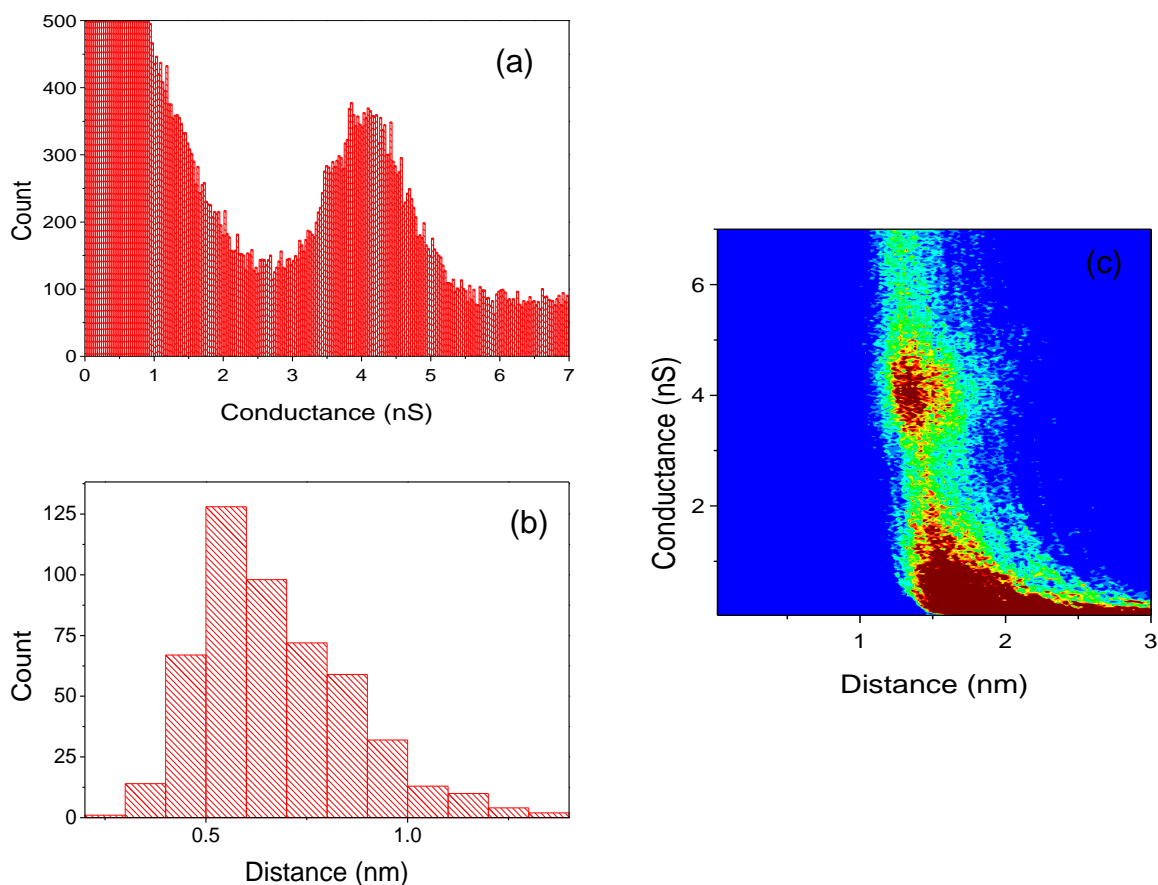
Figure 2.20 Data for BDMT U_{bias} = 0.6 and I_{set} = 30nA (a) Histogram of 500 I(s) scans (b) Histogram of the experimental break off distances (c) 2D histogram showing conductance versus total break off distance.

The high conductance data for the four analogues is summarised in Table 2.4; this again shows that the conductance values decay exponentially with increasing length. Plots of ln(conductance) *vs* length for both high and low conductance are shown in Figure 2.21.

Molecule	Conductance, σ (nS)	Spartan® Au-Au (nm)	Estimated Break-Off (nm)
BDMT	4.14 ± 0.58	1.4	1.44 ± 0.33
3Ph3	2.01 ± 0.32	1.6	1.43 ± 0.28
4Ph4	1.21 ± 0.19	1.9	1.50 ± 0.31
6Ph6	0.82 ± 0.18	2.2	1.70 ± 0.31

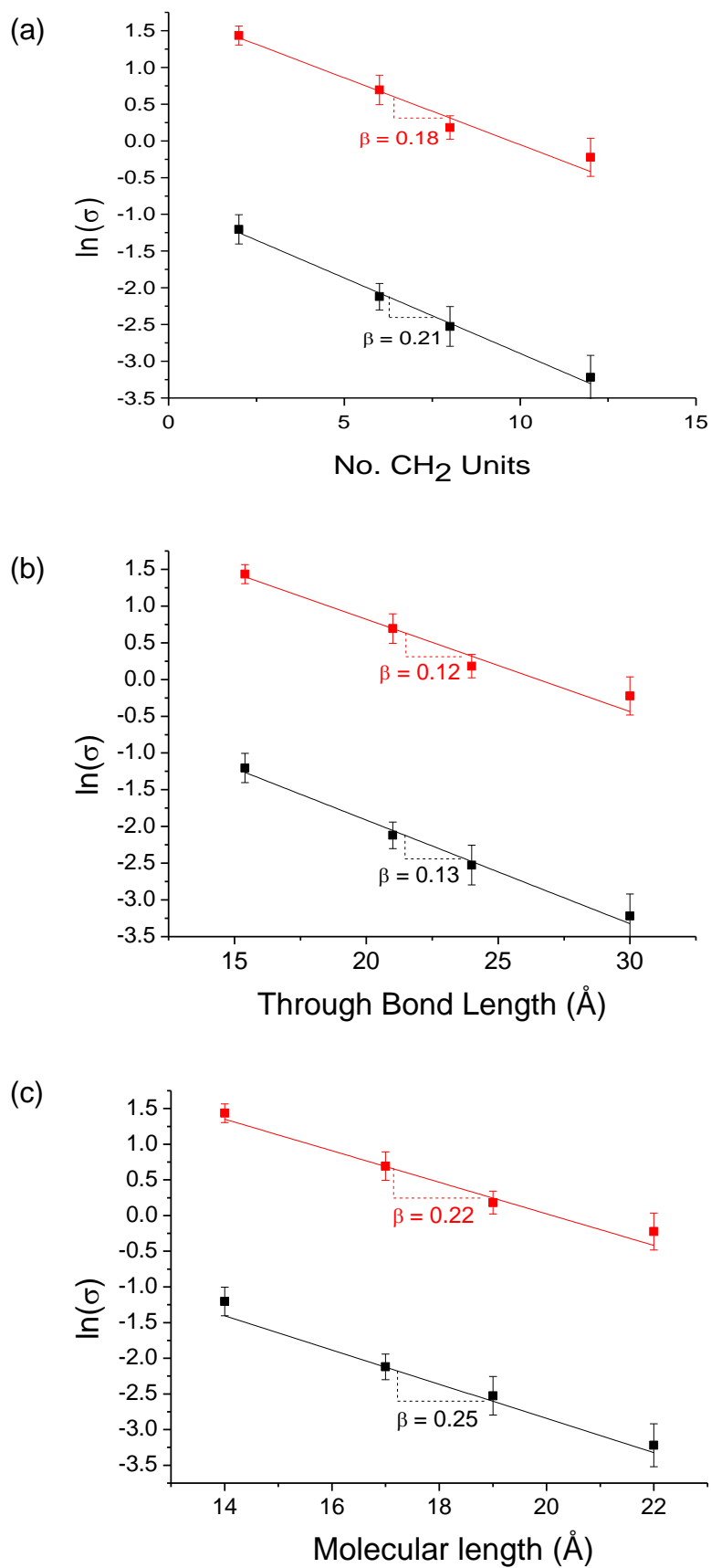**Table 2.4 Summary of the high conductance data, measured using U_{bias} = 0.6V and various set-points.**

Figure 2.21 Plots of ln(conductance) *vs* various measures of distance for both the low (black) and medium (red) conductance groups.

2.5　Molecular Orbitals

The strength of the likely metal-molecule electronic coupling can be judged qualitatively using the energetic positions of the relevant molecular orbitals in comparison to the Fermi level of gold. This provides a method of predicting the effective tunnelling barrier height, which should show very little variation through the series of analogues. The densities of the molecular orbitals can be used to predict which ones are important for charge transport through the molecule.
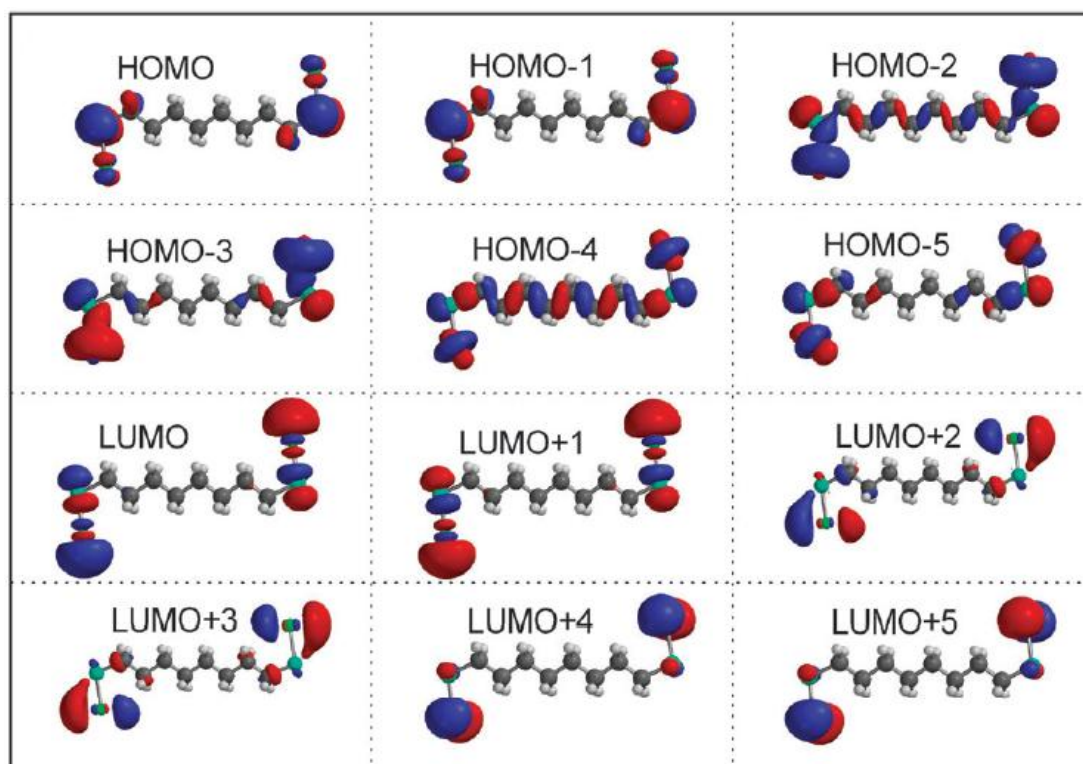

Figure 2.22　Density of the first six HOMOs and LUMOs of octanedithiolate. Reproduced by permission of the PCCP Owner Societies.[76]

Haiss *et al.* have previously reported a theoretical study of the orbital densities and energies of simple alkanedithiols sandwiched between two gold atoms;[76] the orbital densities of the first six HOMOs and LUMOs calculated for octanedithiol in this study are show in Figure 2.22. The LUMOs represented in this figure lie between the Fermi level of gold (at zero bias) and the vacuum level but, as can be seen in Figure 2.22, there densities are located entirely at the sulfur and gold atoms and are therefore not involved in charge transport.

Haiss *et al.* concluded that the orbitals that are relevant to charge transport were HOMO-2 and HOMO-4, both of which have electron densities spanning the entire

71

molecule. The energy of HOMO-2 was calculated to be approximately -7.2 eV, since the Fermi Level of gold has an energy of -5.2 eV[76] the tunneling barrier can be approximated at 2 eV.
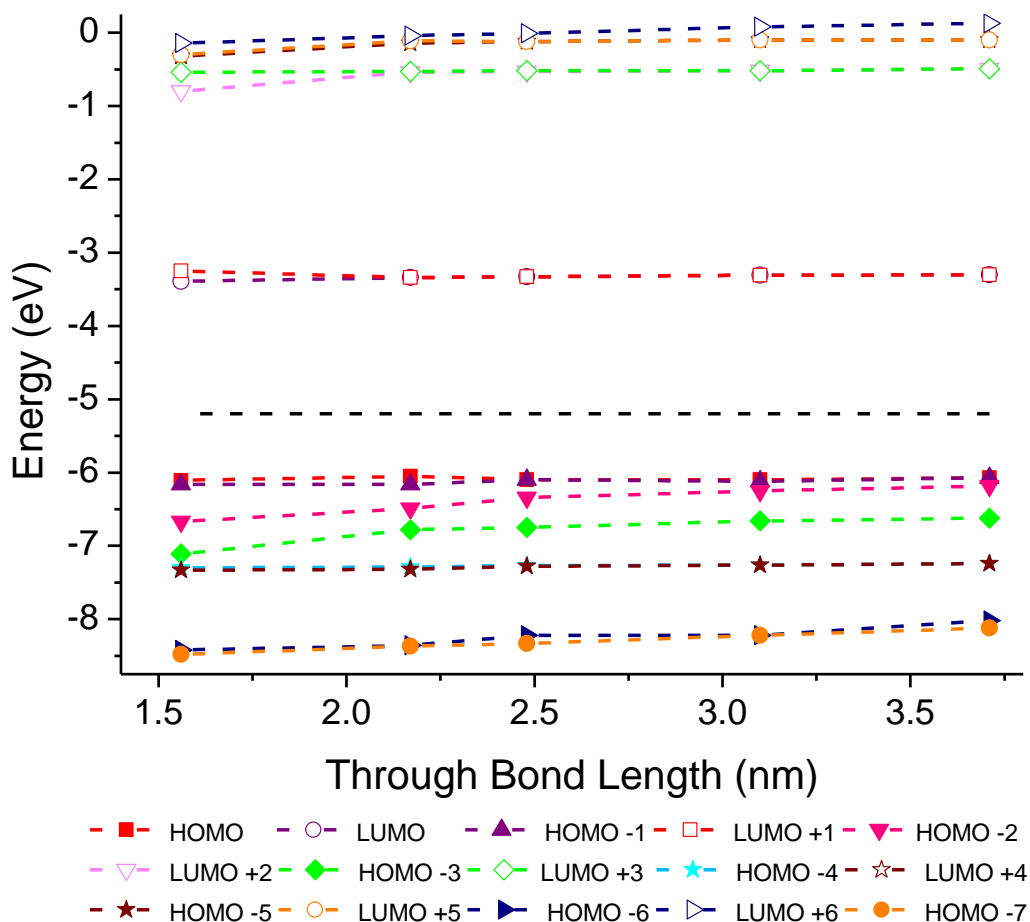

Figure 2.23 Energetic position of the first eight HOMO and the first seven LUMO orbitals of 8Ph8, 6Ph6, 4Ph4, 3Ph3 and BDMT as a function of the through bond molecular length, the black dotted line represents the Fermi energy of gold in vacuum.

In order to perform an analogous study for the current series of molecules the Spartan® implementation of density functional theory (DFT) was used to calculate the molecular orbitals of each dithiol, with one gold atom attached to each sulfur head-group. A B3LYP hybrid exchange correlation function in conjunction with 6-31G* basis set was used, and the core gold orbitals were represented by pseudopotentials.

In Figure 2.23 the energetic positions of the first six LUMO and first seven HOMO orbitals of each of the analogues in the series are shown as a function of through-bond molecular length (for a description of through-bond molecular length see figure

2.14); the Fermi level of gold in vacuum is represented by the dashed black line. Figures 2.24 and 2.25 show the orbital densities of the first six LUMOs and the first ten HOMOs of 6Ph6. As in the study by Haiss and coworkers,[73] it was found that the LUMOs that lie between the Fermi level of gold and the vacuum level (0 V) are located entirely at the sulfur and gold atoms, and are therefore unlikely to be involved in charge transport.
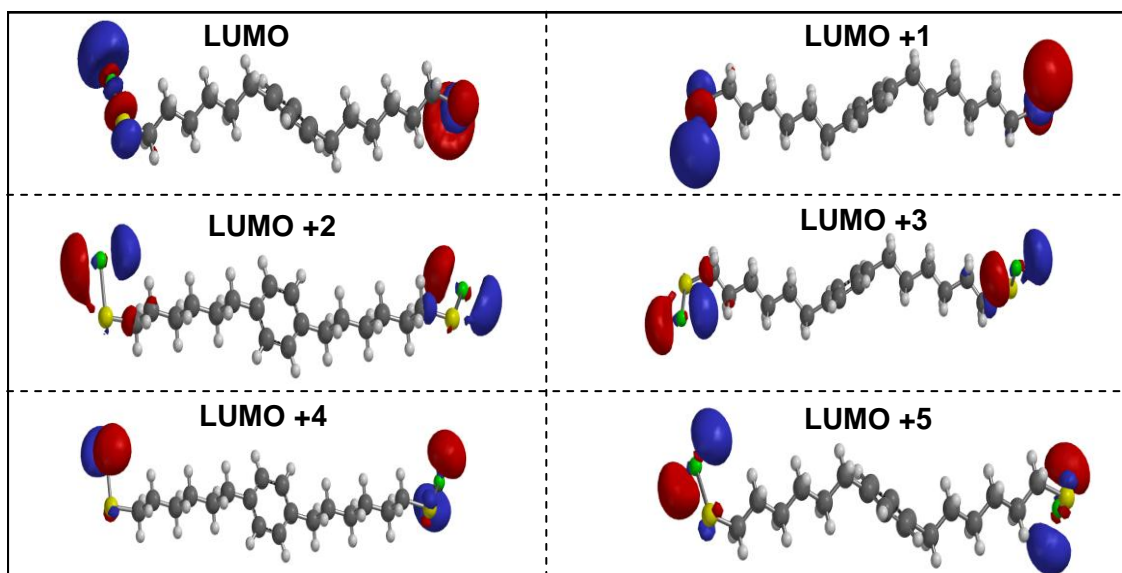

Figure 2.24 Orbital densities of the first six LUMOs of 6Ph6.

From Figure 2.25 it can be seen that HOMO-4, HOMO-5, HOMO-8 and HOMO-9 are located almost entirely on the sulfur and gold atoms, and are consequently not involved in charge transport. The only orbital to span the entire molecule is HOMO-7, which has energy of approximately -8.5 eV. Transport solely through this orbital would therefore have a barrier of approximately 3.3 eV, which is much larger than the predicted value for alkanedithiols. As can be seen from equation 1.8, the conductance is proportional to minus the exponential of the square root of the barrier height. An increase in this value from -7.2 to -8.5 eV would therefore result in a very large decrease in conductance in comparison to the alkane dithiols. Hence, it is unlikely that tunnelling through the molecule is through HOMO-7 alone.
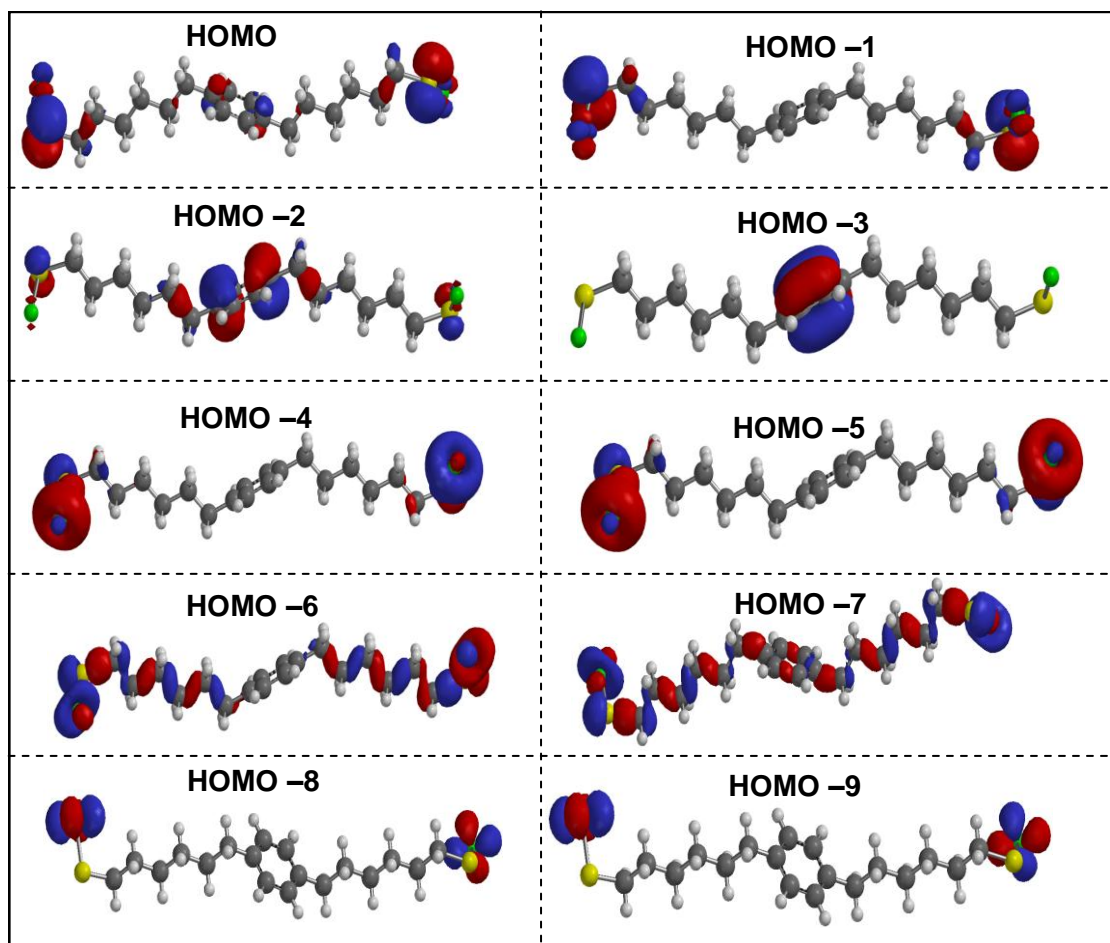
Figure 2.25 Orbital densities of the first ten HOMOs of 6Ph6.

Several other orbitals do have some density located on the molecule, most notably HOMO-2 and HOMO-3, which have energies of -6.25 and -6.66 eV respectively. As can be seen in Figure 2.25 these orbitals are located largely on the central benzene ring (and the contacts in the case of HOMO-2), and have energies much closer to the Fermi level. This orbital picture suggests that the mechanism of charge transport could be different to that of the alkane dithiols, and may see contributions from a 'hopping' type mechanism.

2.6   Discussion

A summary of all the conductance data, along with attenuation factors and estimated break-off distances, is shown Table 2.5.

Molecule	High Conductance (nS)	Estimated Break-Off (nm)	Low Conductance (nS)	Estimated Break-Off (nm)	Spartan Au-Au (nm)
BDMT	4.14 ± 0.58	1.44 ± 0.33	0.3 ± 0.06	1.62 ± 0.28	1.4
3Ph3	2.01 ± 0.32	1.43 ± 0.28	0.12 ± 0.02	1.55 ± 0.21	1.6
4Ph4	1.21 ± 0.19	1.50 ± 0.31	0.08 ± 0.02	1.86 ± 0.29	1.9
6Ph6	0.82 ± 0.18	1.70 ± 0.31	0.04 ± 0.01	1.84 ± 0.22	2.2
β (Å^{-1}, TB)	0.12		0.13		

Table 2.5 Summary of the conductance data (attenuation factor quoted from through bond data).

As can be seen the break-off distances correspond well with the Spartan® estimated Au-Au separations, and generally decrease with the length of the molecule. Furthermore, the estimated break-off distance for each of the higher conductance groups is lower than that of each corresponding lower conductance group; this result fits well with the theory of Haiss *et al.* regarding multiple conductance groups[69] (see section 2.1.1). According to this theory the higher conductance group is observed when the molecule is adsorbed to a step edge on the gold surface; in such circumstances the tip-substrate gap will be smaller than in the corresponding case when the molecule is adsorbed at a top site. It follows that the estimated break-off distance would be predicted to be shorter for the higher conductance groups, as is the case in the study presented herein. However, the low conductance values are smaller than expected. Indeed, the value determined for 6Ph6 is much lower than that reported by Leary *et al.*,[56] although the conductance value determined at the elevated set point current is in good agreement with their study; this suggests that they actually missed the 'A' group and recorded the 'B' group.
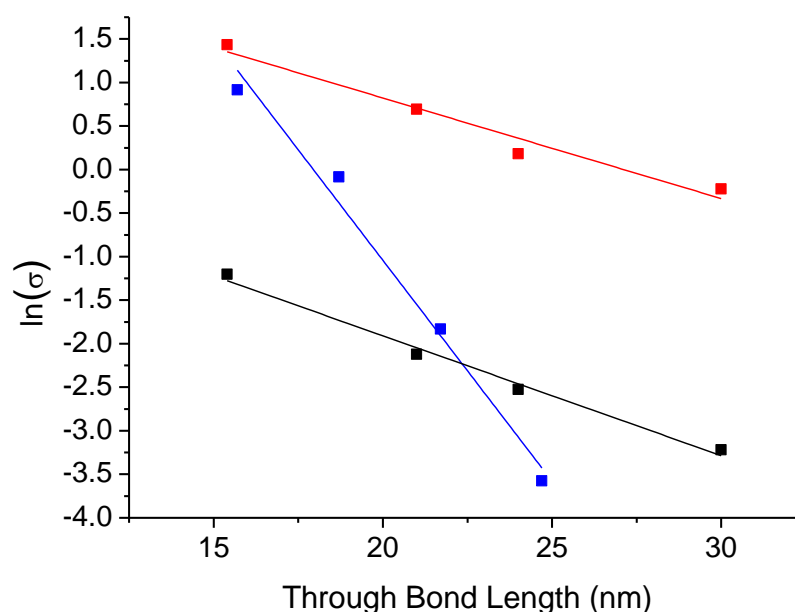
Figure 2.26 Comparison of the length dependence data in this work (black and red lines) to that of Haiss _et al._[76] for various alkanedithiols.

The attenuation factors of both the high and low conductance groups are also exceptionally small in comparison to previous examples[76] involving a tunnelling mechanism (Figure 2.26); such small values are usually characteristic of hopping mediated charge transport.

As discussed in section 2.1, studies of the relatively straightforward alkanedithiol series of molecules have yielded several conflicting values for their attenuation. Haiss _et al._ have systematically studied the conductance of single molecules of alkanedithiols tethered to gold electrodes; the molecules in this study ranged from 3 to 12 methylene units.[76] They found that for molecules containing 8 or more methylene units the conductance decays exponentially with length, which is in good agreement with previous studies. Contrastingly, for shorter molecules containing less than 8 methylene units the attenuation factor decreases with decreasing length, approaching length-independence for molecules containing less than 5 methylene units (Figure 2.27). Haiss and coworkers then performed a theoretical study and noted that an image charge dependent value of the effective hole mass results in quantitative agreement with the experimental results. The data in the current study appears to mirror the latter result, however since the molecules in this work are much longer the same argument cannot be applied.
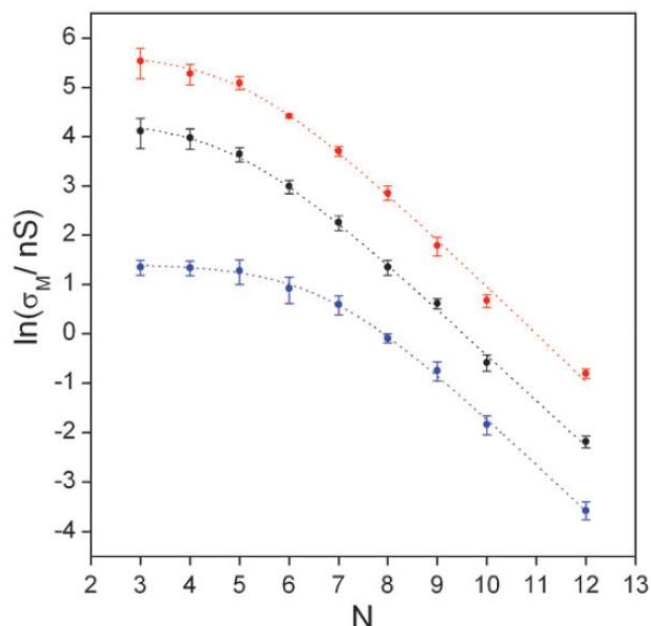
Figure 2.27 Logarithm of conductance of the three fundamental single molecule conductance groups measured for alkanedithiols between gold contacts as a function of the number of CH_2 groups (N) at U_{bias} = 0.6V. Reproduced by permission of the PCCP Owner Societies.[76]

The contribution of hopping mediated charge transport in this system appears to fit the experimental observations; this mechanism would see the benzene ring acting as a 'hopping site'. Charge transport through the molecule would require tunnelling through the first alkyl chain, followed by localization on the benzene ring for a finite time, before tunnelling through the second alkyl chain (Figure 2.29). The orbital densities and energies discussed in section 2.5 fit well with this mechanistic description; the higher energy orbitals located on the alkyl chains function as tunnelling barriers, with the lower energy orbitals on the benzene ring acting as the hopping site. Leary *et al.* have investigated analogues of 6Ph6 in which substituents are introduced to the benzene ring (see section 1.6); they found that the closer the HOMO energy of the aromatic unit is to the Fermi level of gold, the higher the conductance. Whilst this was used as evidence for these molecules acting as double tunnelling barriers, the relationship between the energy of the aromatic HOMO and conductance also provides evidence for a hopping contribution to the mechanism of charge transport.
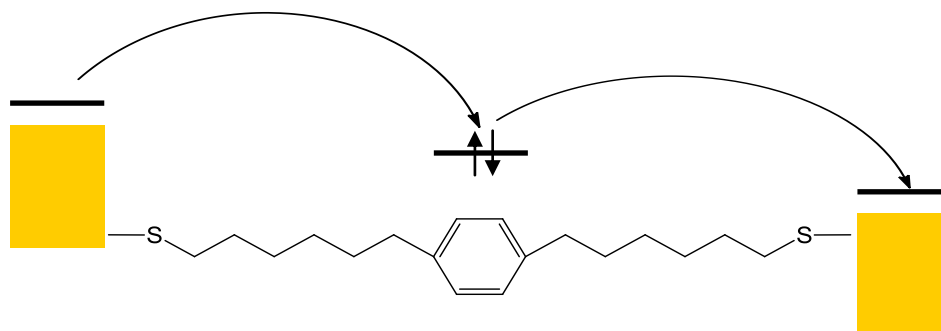
Figure 2.28 Charge transport though 6Ph6 *via* the hopping mechanism.

Since it has already been established that charge transport in the current system is HOMO mediated, it follows that hole, as opposed to electron, transfer is responsible. Similar charge hopping has previously been proposed for DNA.[77] Ratner and co-workers have reported a detailed study of the efficiency of hole migration along sequences of stacked nucleobases with different numbers of adenine-thymine (AT) and guanine-cytosine (GC base pairs).[78] They propose a hopping model, similar to the one described in this work, in which AT base pairs act as tunnelling barriers over which the transport takes place *via* incoherent hopping, with the charge residing on G bases (G has the lowest oxidation potential and hence provides the best hole hopping sites).

2.7   Conclusions and Future Work

The conductance data presented in this work resulted in an unexpected, ultra-low attenuation factor for the analogous series; the value was found to be approximately 0.13 Å^{-1}. As discussed, this suggests a contribution from hopping mediated charge transport in these systems.

The experiments normally employed to unambiguously determine the mechanism of charge transport probe the dependence of conductance on either voltage or temperature, with the latter being the most common. Analysis of the temperature dependence of conductance could provide further evidence regarding the nature of charge transport through this system; coherent tunnelling usually exhibits temperature dependence whilst hopping does not. However, measurements of this nature are not always experimentally straightforward. Haiss and coworkers have studied the temperature dependence of the conductance of alkanedithiols;[79] they observed a pronounced temperature dependence. The origin of this temperature dependence was proposed to be the change in molecular conformer distribution

rather than transitions between conduction mechanisms. This can be thought of as thermal gating, where gating refers to regulating the flow of current by thermally controlling the population of different molecular conformers. This conformer effect could introduce ambiguity in temperature dependence experiments, particularly in the longer chain analogues. The results of a temperature dependence study would, therefore, have to be considered carefully in order to ensure that any correlation between temperature and conductance is not misinterpreted.

The conductance data for 8Ph8, and molecules with even longer alkane chains, would be of great interest to this study. In the hopping model shown in Figure 2.28 the alkyl chains are considered to be two individual barriers, in this case (6Ph6) each containing six methylene units. The work described in section 2.6 by Haiss *et al.* showed an increase in attenuation with length for molecules consisting of eight methylene units or more.[73] Conductance data for 8Ph8 and even longer molecules would show if the attenuation in these molecules follows the same trend. If this is found to be the case it would support the mechanism of transport discussed in section 2.6, in which the alkyl chains act as tunnelling barriers through which the transport takes place *via* tunnelling, with the charge residing on the benzene ring for a finite time.

If a hopping type mechanism is indeed responsible for charge transport through this molecular architecture, it would be of great interest to investigate whether the conductance through much longer alkane chains can be enhanced. The introduction of multiple phenyl rings into such extended chain lengths would provide multiple hopping sites, and could potentially provide long, highly conductive molecular wires of relative simplicity.

Chapter 3

Synthesis of Rotationally Restricted 4,4'-Bipyridines

3.1   General Introduction and Aim

Another molecular system that has received much attention in molecular electronics is that of 4,4'-bipyridine, which has been studied both as the neutral molecule, in which case it binds to gold electrodes through nitrogen, and as a dication with functionalisation at nitrogen, usually in the form of alkyl chains. In the latter case, the alkyl chains contain terminal thioacetate groups, which provide a gold anchor point.

As discussed in section 1.6.2.1, it has previously been shown that the conductance of a molecule containing a 4,4'-bipyridine centre, sandwiched between two thioacetate end-capped hexyl chains (Figure 3.1, X = H), shows an unusual conductance-redox potential relationship. It was suggested that this is due to changes in conformation between the two pyridine rings as a function of redox state. Therefore, it would be desirable to measure the conductance, as a function of redox potential, of rotationally-restricted analogues. However, no such analogues are commercially available and thus they will have to be synthesised.
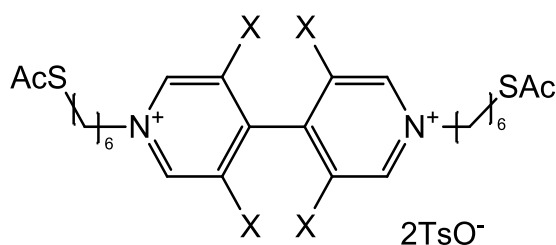

Figure 3.1 The generic structure of the desired analogues.

Further to this work, Professor Walther Schwarzacher's group at Bristol University have recently used an STM BJ method to determine the conductance of 4,4'-

bipyridine (BIPY) without functionalisation at nitrogen. They found the molecule exhibited two conductance groups, at values of approximately 59 nS and 14 nS (Figure 3.2); these conductance values are in good agreement with previous work by Venkataraman and coworkers.[80] The latter group demonstrated that the conductance could be reversibly switched between the two conductance states through repeated junction compression and elongation. They attributed the two conductance groups to distinct contact geometries at the nitrogen-gold bond, with the low conductance group being observed when this bond is perpendicular to the π-system. Furthermore, Schwarzacher *et al.* have found that the conductance of BIPY could be gated electrochemically, despite the lack of a redox switch within the accessible range.[81] It was therefore of interest to repeat these experiments with other analogues; this will help to probe the role of torsion angle and ring twisting in conductance, as well the conductance behaviour of substituted analogues of BIPY.
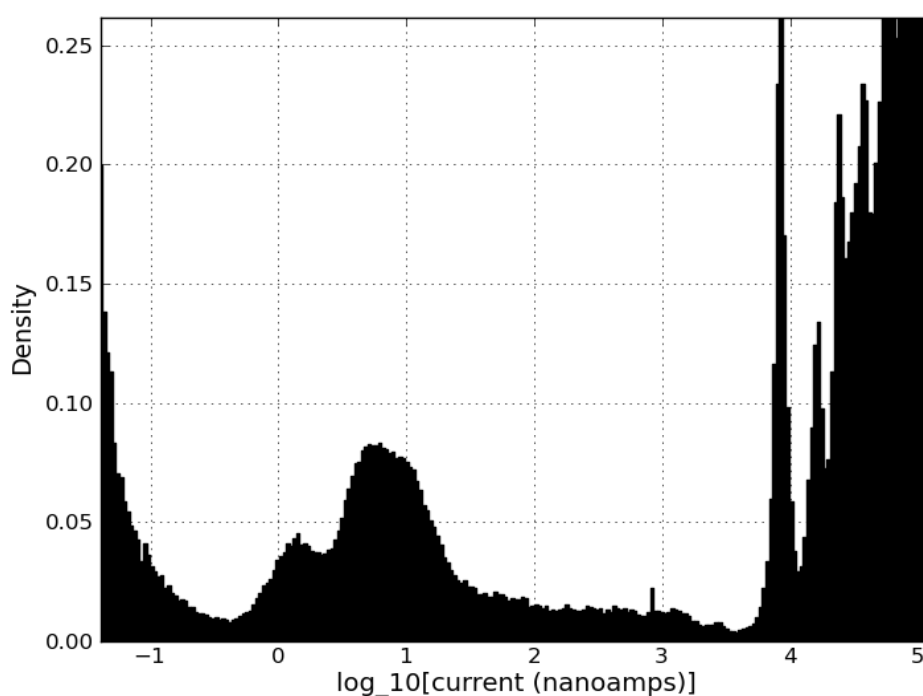

Figure 3.2 Histogram of approximately 1500 scans for BIPY acquired at 0.1 V using the STM BJ technique, provided by Doug Szumski of Bristol University.

The aim of this work was therefore to produce substituted analogues of BIPY, both with and without thioacetate end-capped carbon chains. This would hopefully provide molecules with varied electronic properties as well as different degrees of rotation between the two pyridine units.

3.2   Attempts to Synthesize 2,7-Diazapyrene

One of the closest planar analogues to the viologen redox group is 2,7-diazapyrene, the structure of which is shown in Figure 3.3. The synthesis of this molecule has been published; however, procedures are protracted and low yielding.[82,83]
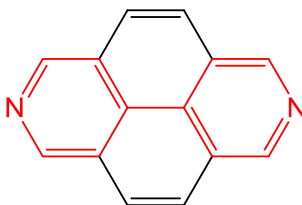

Figure 3.3 The structure of 2,7-diazapyrene highlighting the similarity to 4,4'-bipyridine.

The first literature example, published in 1968[84], involved dehydrogenation of [2.2] (3,5) pyridinophane using palladium on carbon (Pd/C) at 290 °C. However the synthesis of the starting material was very low yielding (2% overall) and the dehydrogenation also gave a poor yield (30 %) making this route impractical.
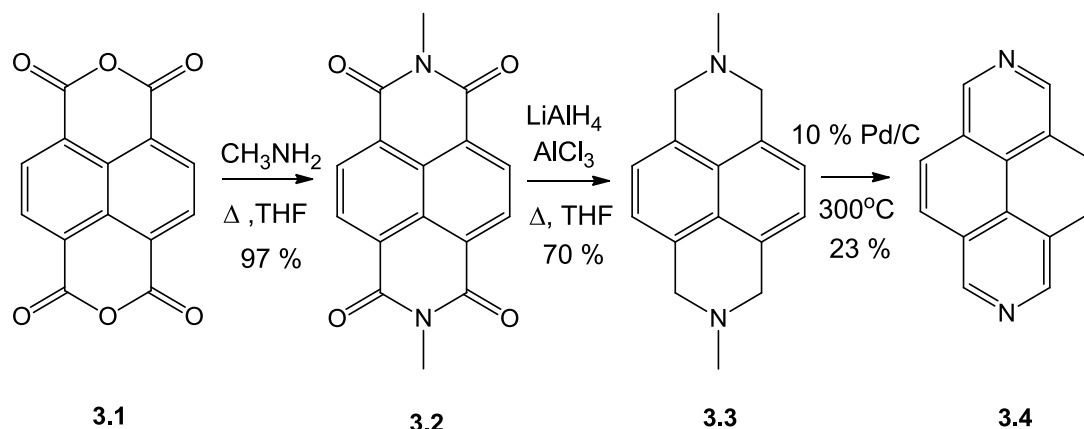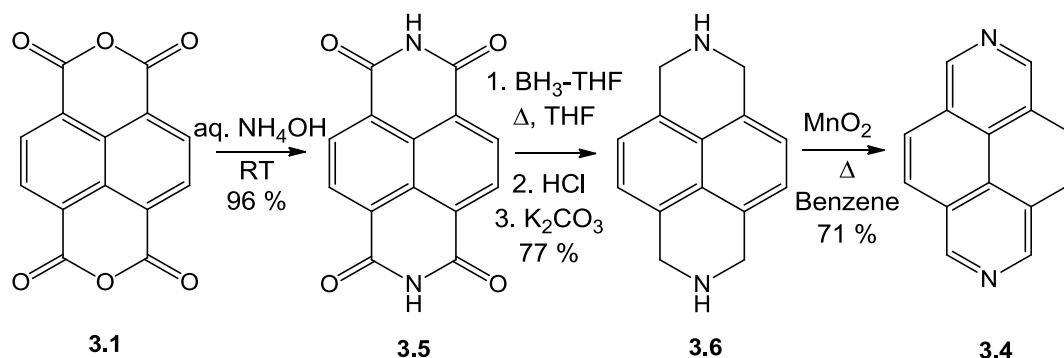

Scheme 3.1 The synthesis of 2,7 diazapyrene reported by Stang *et al.*[85]

An alternative synthesis, shown in Scheme 3.1, was published in 1995 by Stang *et al.*[85] and involves the reaction of 1,4,5,8-naphthalenetetracarboxylic dianhydride **3.1** with methylamine to give *N,N'*dimethyl-1,4,5,8-naphthalenetetracarboxylic diimide **3.2** in excellent yield. This was then reduced with lithium aluminium hydride to give 1,3,6,8-tetrahrydro-*N,N'*-dimethyl-2,7-diazaprene **3.3**, which was subsequently oxidised with 10 % Pd/C to give 2,7-diazapyrene **3.4**. This final oxidation step uses a large amount of Pd/C and involves three separate purifications, giving the final product in low yield. Alternative oxidation methods include the use of red selenium

as an oxidant in a high temperature melt. Although this method improves the yield of the reaction, a significant amount of hydrogen selenide is produced, which is extremely toxic (exposure limit 0.3 ppm over 8 hours) and highly malodorous.

A more recent method, published in 2000 by Sotiriou-Leventis *et al.*,[86] reported a high yielding three step synthesis of diazapyrene, as shown in Scheme 3.2.

Scheme 3.2 The synthesis of 2,7-diazapyrene by Sotiriou-Leventis *et al.*[86]

The first step involves the reaction of 1,4,5,8-naphthalenetetracarboxylic dianhydride **3.1** with aqueous ammonium hydroxide to give 1,4,5,8-naphthalenetetracarboxylic diimide **3.5** in excellent yield. This can then be reduced to 1,2,3,6,7,8-hexahydro-2,7-diazapyrene **3.6** with BH_3-THF in good yield. The final aromatisation step was achieved by refluxing the latter compound with MnO_2 in benzene to give a good yield of 2,7-diazapyrene **3.4**.

Whilst this synthesis appeared promising, the procedure required the use of copious amounts of benzene, which is a known carcinogen and not permitted on a large scale in the laboratory in which this work was undertaken. Attempts to repeat the synthesis using toluene in place of benzene proved unsuccessful. It was decided that several new potential routes to 2,7-diazapyrene **3.4** would be investigated, using a combination of the above syntheses and some procedures adapted from published reactions using similar substrates.
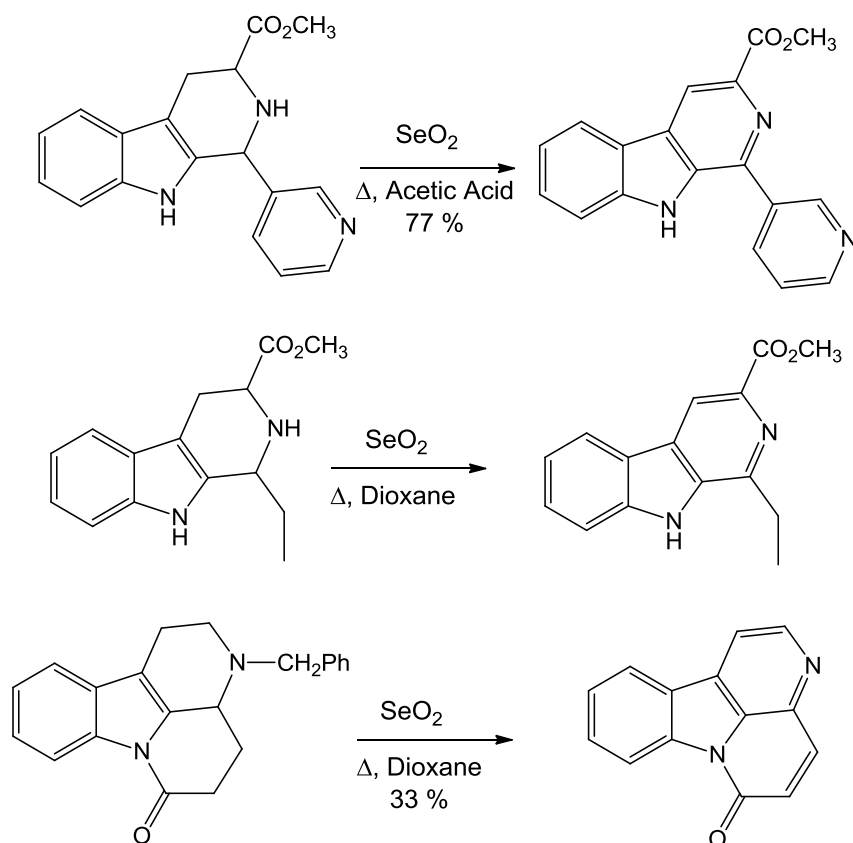
Figure 3.4 Examples of selenium-mediated oxidation.[87]

The first potential alternative is selenium dioxide-mediated oxidation; this was investigated in some detail by Cain *et al.* in 1983.[87] Some examples from their investigation are shown in Figure 3.4. This work suggested the potential to use reaction conditions analogous to those seen in the first 2 steps of Scheme 3.1 or 3.2, and then oxidise to the final product with selenium dioxide, as illustrated in Scheme 3.3.
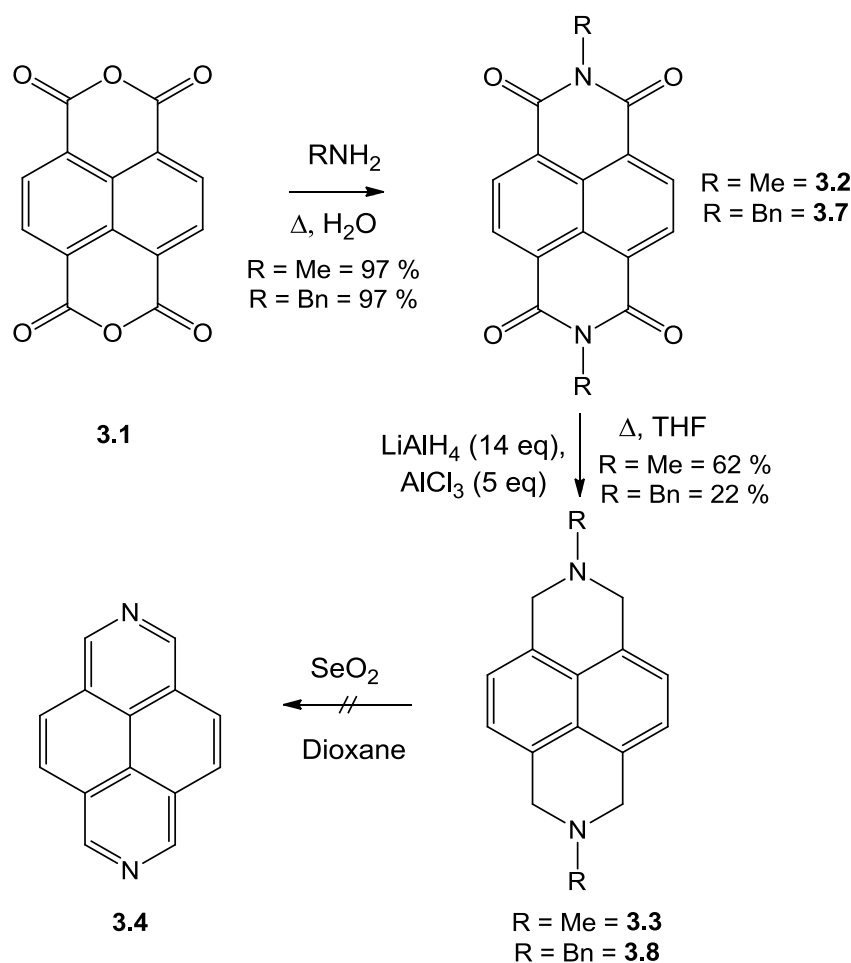
Scheme 3.3 Modified procedure for the attempted synthesis of 2,7-diazapyrene 3.4.

After careful consideration, we decided to attempt the synthesis using the benzyl- and methyl- amine/amide analogues (Scheme 3.3), since these should show an increased solubility in organic solvents compared to the secondary amine/amide reported by Sotiriou-Leventis *et al*. The first two steps in the synthesis of the methyl analogues **3.2** and **3.3** were identical to those used by Stang *et al*.,[82] and gave yields of 97 % and 62 % respectively. However, subsequent attempts to perform the oxidation using selenium dioxide in dioxane showed no trace of the final compound, as evidenced by ^{1}H NMR analysis.

The synthesis of benzylamide **3.7** was also straightforward, giving the desired material in 97 % yield. The reduction of this compound was attempted using both the BH_3-THF and $LiAlH_4$ conditions, with the latter proving the most successful. The product extracted from the BH_3-THF reaction appeared to be a mixture of a small amount of final product, and a partially reduced intermediate upon inspection of the ^{1}H NMR. The IR spectrum also showed a peak characteristic of a carbonyl group.

This mixture of products proved difficult to separate. The lithium aluminium hydride conditions, after some alteration of the literature work up, provided a disappointing yield of the reduced benzylamine **3.8**. However, we decided to determine whether the oxidation step in this synthesis was viable before attempting to optimise the reduction method. Unfortunately the oxidation of compound **3.8** using selenium dioxide proved unsuccessful.

Since it was desirable to functionalise the nitrogen atoms in this compound with a thioacetate end-capped alkyl chain, we decided to attempt the synthesis by installing the side chain at the beginning (Scheme 3.4). Naphthalenetetracarboxylic dianhydride **3.1** was treated with 6-aminohexan-1-ol, triethylamine and DMF in a microwave reactor to give compound **3.9** in 56% yield.[88] This could not be easily reduced using lithium aluminium hydride in the presence of the free hydroxyl groups, which were therefore protected with tetrahydropyran (THP) groups.
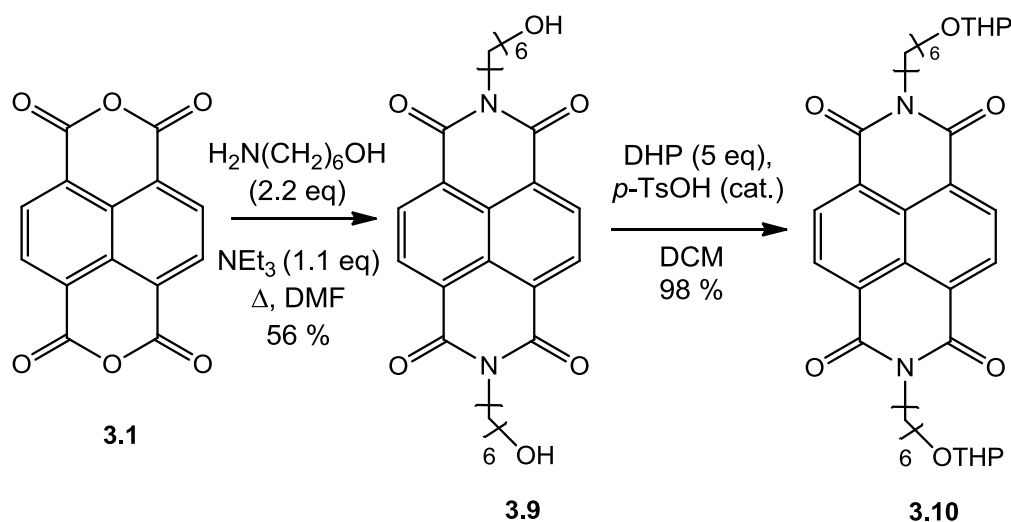

Scheme 3.4 Treatment of naphthalene tetracarboxylic acid 3.1 with 6-aminohexan-1-ol and subsequent protection with dihydropyan (DHP).

The reduction of protected compound **3.10** proceeded in a disappointing 27% yield (Scheme 3.5); however this provided enough material to test the viability of this route. The compound was treated with hydrochloric acid in order to remove the THP protecting groups, the resulting diol was highly insoluble and proved difficult to characterise. Attempts were made to oxidise both THP-protected compound **3.11**, and deprotected compound **3.12** using 2,3-dichloro-5,6-dicyano-1,4-benzoquinone (DDQ). Unfortunately no trace of oxidised material was seen in either of these reactions.
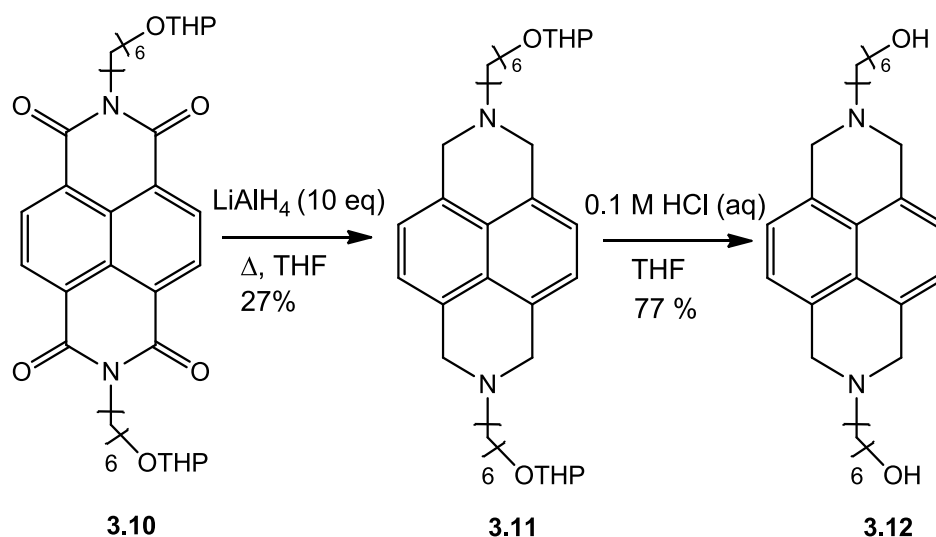
Scheme 3.5 Reduction of the carbonyl groups of compound 3.10 and subsequent deprotection of the hydroxy groups.

A relatively recent publication by Aksenov *et al.* reported a novel method for synthesising azapyrenes using triazine **3.14** in polyphosphoric acid (PPA).[89] They suggested the synthesis of 2,7-diazapyrene **3.4** from 2,3-dihydro-1*H*-benzo[*de*]isoquinoline **3.13** proceeded in 55 % yield (Scheme 3.6).
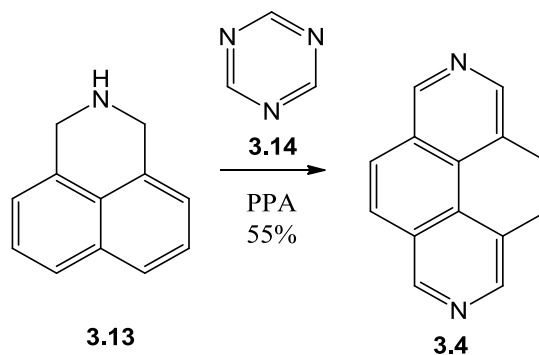
Scheme 3.6 Synthesis of 2,7-diazapyrene 3.4 as reported by Aksenov *et al.*[89]

Attempts to repeat this synthesis using commercially sourced 2,3-dihydro-1*H*-benzo[*de*]isoquinoline **3.13** did not yield any of the desired compound. It was therefore decided to freshly prepare the starting material from naphthalic anhydride **3.15** (Scheme 3.7). The latter compound was treated with benzylamine in water to give compound **3.16** in 86 % yield. This was then reduced with lithium aluminium hydride and aluminium chloride prior to debenzylation using catalytic palladium on carbon under a hydrogen atmosphere.
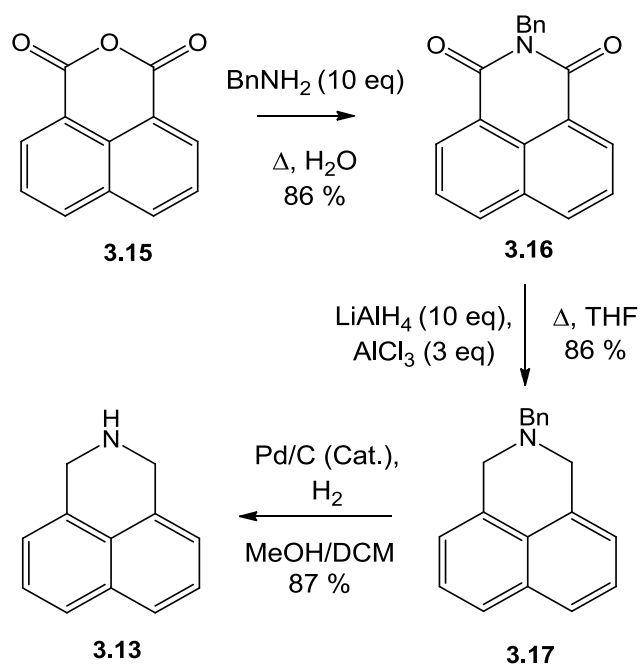
Scheme 3.7 Synthesis of 2,3-dihydro-1*H*-benzo[*de*]isoquinoline 3.13 from naphthalic anhydride.

Whilst the synthesis of diazapyrene did provide the desired compound, the yield was consistently less than 1 % and the isolated material was impure. This result was the same with both commercially sourced and freshly prepared PPA.

3.3 Synthesis and Reactions of Polyhalogenated 4,4'-bipyridines

During this work a publication by Abboud *et al.* reported a synthetic route to polyhalogenated 4,4'-bipyridines.[90] These were of interest for two reasons, firstly they are conformationally restricted, and secondly they have the potential to provide a novel route to 2,7-diazapyrene. The synthesis of these bipyridines is a straightforward dimerisation of commercially available dihalogenated pyridines, the study reported several high yielding examples (Scheme 3.8).
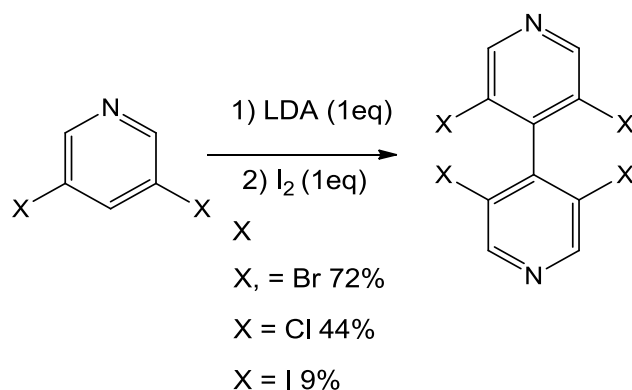
Scheme 3.8 Reported synthesis of polyhalogenated 4,4'-bipyridines.

The reported experimental conditions detail the use of one equivalent of both lithium diisopropylamine (LDA) and iodine in order to dimerise the substituted pyridines (Scheme 3.8)[90]. At first look this seemed unlikely, since one equivalent would see complete deprotonation of the starting pyridine. Indeed several attempts to repeat the synthesis of tetrachlorobipyridine **3.20** using one equivalent of the reagents did not yield any of the dimerised compound, instead giving dichloroiodopyridine **3.19** in 85% yield (Scheme 3.9). The reaction was repeated using half an equivalent of both reagents, this consistently provided the desired dimer **3.20** in around 35 % yield.
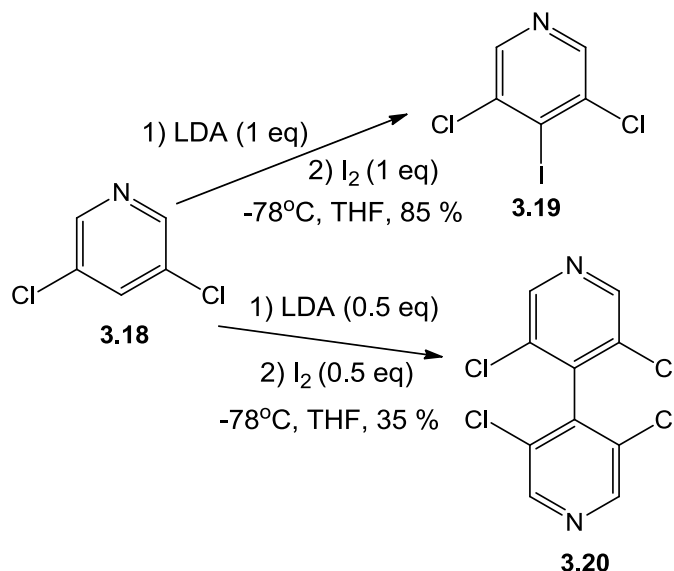
Scheme 3.9 Synthesis of dichloroiodopyridine during attempts to dimerise dichlorobipyridine.

We envisaged two plausible mechanisms for the dimerisation, these are shown in Figure 3.5; the purple arrows are mutual to both suggestions whilst the red and blue arrows detail the two separate mechanisms. Both mechanisms start with the

deprotonation of one pyridine unit. The resulting anion can then either attack the 4-position of a second pyridine unit to give intermediate **3.21b** directly, or donate a single electron into the π-system of a second pyridine unit, giving intermediates **3.21c** and **3.21d**. The latter two intermediates can then dimerise to give intermediate **3.21b**, which is then oxidised by iodine to give the bipyridine dimer. The final step is common to both mechanisms and is detailed with purple arrows. It can be seen that neither mechanism would require complete deprotonation of the pyridine monomer.
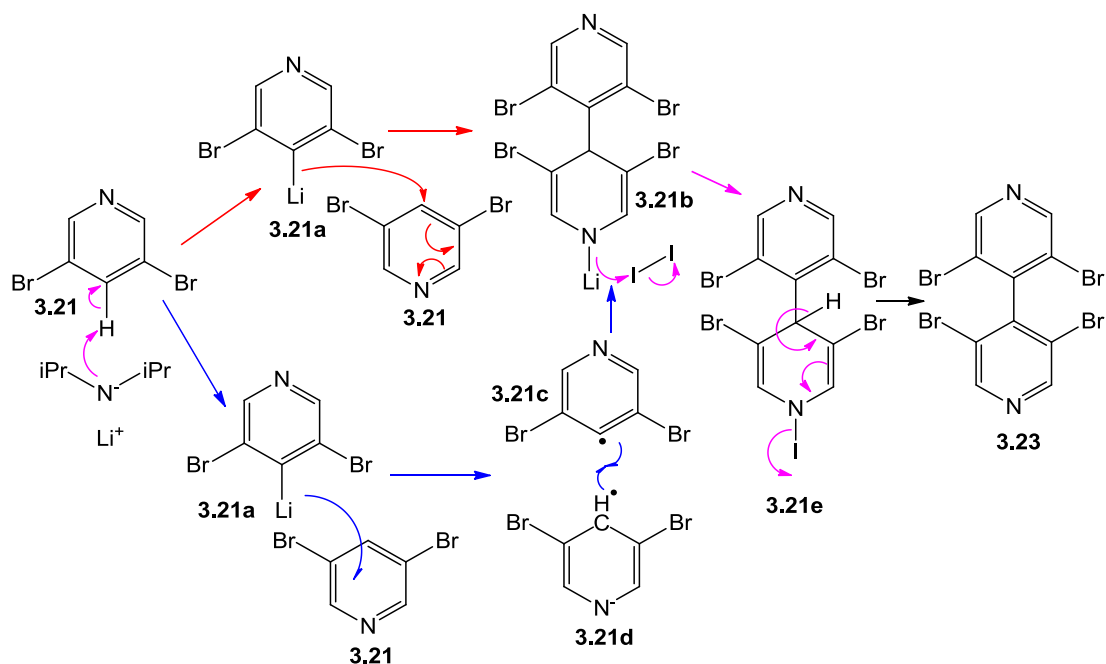
Figure 3.5 Two possible mechanisms for the dimerisation of dihalopyridines.

In order to confirm the presence of intermediate **3.21e**, the reaction using 3,5-dibromopyridine was repeated using acetic anhydride in place of iodine (Scheme 3.10). This provided compound **3.22**, which was stable and could be isolated and characterised. The restricted rotation about the amide bond in this molecule should render the environments of all the ring protons different. The NMR data did indeed show different shifts for each proton, moreover the peaks corresponding to these protons broaden considerably upon heating (Figure 3.6).
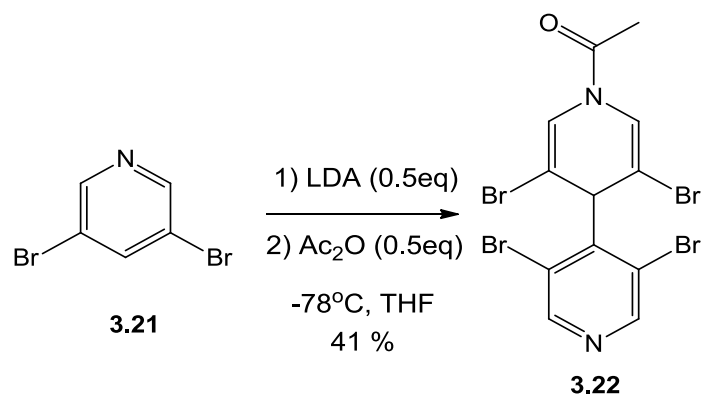
Scheme 3.10 Replacement of iodine with acetic anhydride to provide a stable analogue of intermediate 3.21e.

The presence of this intermediate supports both mechanisms detailed in Figure 3.5. To attempt to distinguish between the two possibilities the reaction was repeated as normal in the presence of 2,4,6-di-*tert*-butylphenol, which is a known radical trap. The selection of this compound was due to the use of LDA, which is known to react with many other radical traps. The presence of this compound completely shut down the reaction, providing good evidence for a radical mechanism.
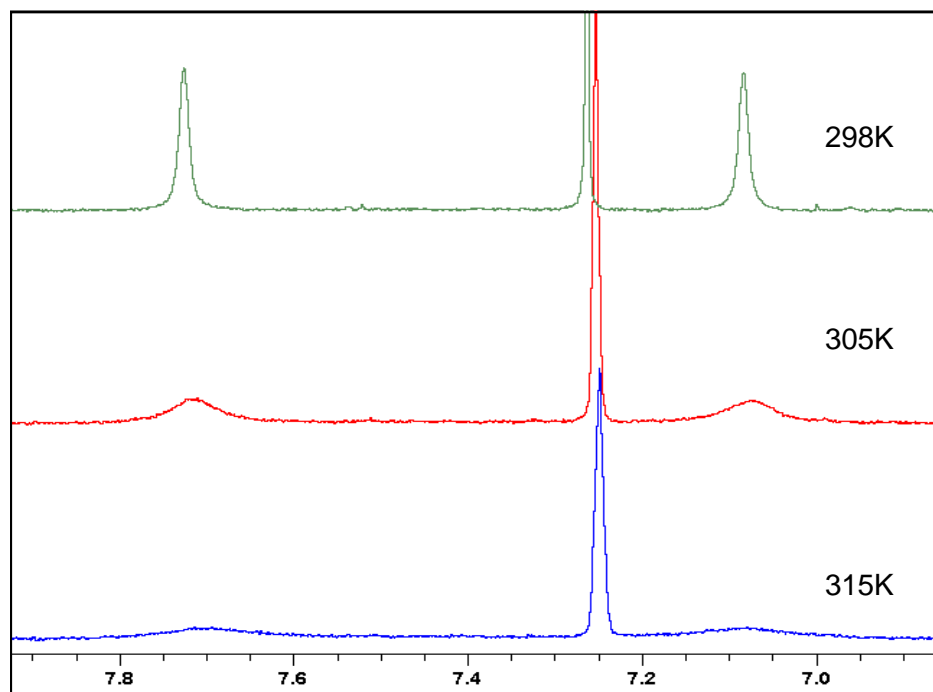

Figure 3.6 Variable temperature NMR spectra of compound 3.22, showing the broadening of the peaks corresponding to the two alkene protons.

With the optimised conditions in hand, the preparation of both tetrachlorobipyridine and tetrabromobipyridine could be achieved in reasonable yield. In order to be

91

useful for STM experiments under electrochemical control for comparison with 6V6, these compounds should be functionalised with thioacteate end-capped carbon chains on the nitrogen. However, in order to be suitable they must also exhibit reversible electrochemical behaviour. To probe their electrochemical behaviour they were reacted with methyl iodide to provide their dimethyl diiodide salts (Scheme 3.11). The electrochemical studies of these compounds are presented in Chapter 4.
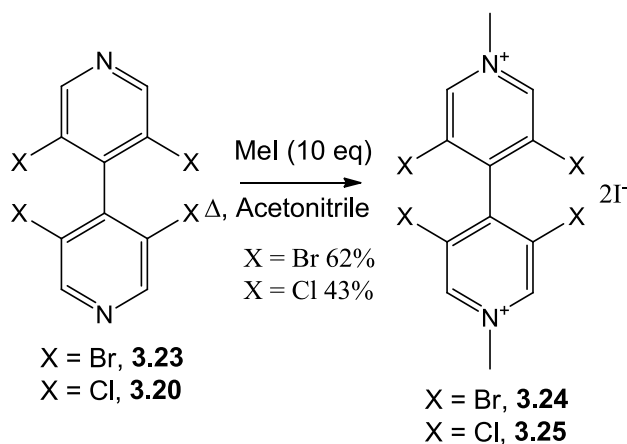
Scheme 3.11 Synthesis of the *N*-methyl diiodide salts of tetrachloro- and tetrabromobipyridine.

If either compound was found to be potentially suitable for EC STM, it would need to be functionalised with the appropriate sidechain in order to allow it to form metal-molecule-metal junctions.
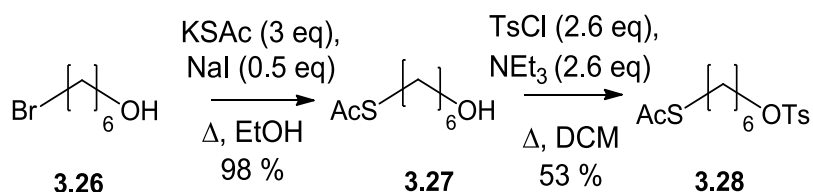
Scheme 3.12 Synthesis of a side chain to functionalize tetrahalobipyridines 3.20 and 3.23.

Scheme 3.12 shows the synthesis of the necessary side chain. Bromohexanol **3.26** was first treated with potassium thioacetate and a catalytic amount of sodium iodide in acetone to give compound **3.27**, which was then converted to tosylate **3.28** using tosyl chloride and triethylamine in DCM. Unfortunately, attempts to react this with tetrachlorobipyridine proved unsuccessful. The triflate analogue of compound **3.28** was subsequently synthesised and employed in this reaction, but also proved unsuccessful. Whilst this prevents the use of the functionalized compound for

electrochemical control, colleagues at Bristol University were able to measure the single molecule junction conductances of both of the unfunctionalized molecules using the STM break junction method; these results are discussed in Chapter 4.

3.3.1   Functionalizing Tetrahalobipyridines

The results of conductance studies performed on the two tetrahalobipyridines created a need for further analogues, more specifically a dihalobipyridine and a more electron rich, but rotationally restricted, analogue. The need for further analogues, and the potential for a novel synthesis of 2,7-diazapyrene, led to a study of the potential reactions of the tetrahalobipyridines.

One of the most effective methods of introducing new functionalities on pyridine rings is to employ palladium catalysed coupling reactions. Generally speaking bromo compounds tend to be more reactive than chloro compounds in these reactions, therefore tetrabromobipyrine was the substrate of choice for the next study.

The first coupling attempted was a Stille reaction employing two equivalents of tributylvinyl tin to try and install vinyl substituents (Scheme 3.13). If this first coupling proceeded as planned, continued exposure of the resulting product to Pd(0) could lead to an intramolecular Heck coupling giving 2,7-diazapyrene **3.4**. Unfortunately, several attempts at this reaction proved unsuccessful, with the starting material being isolated on all occasions. We varied the source of palladium, solvent, temperature and ligand.
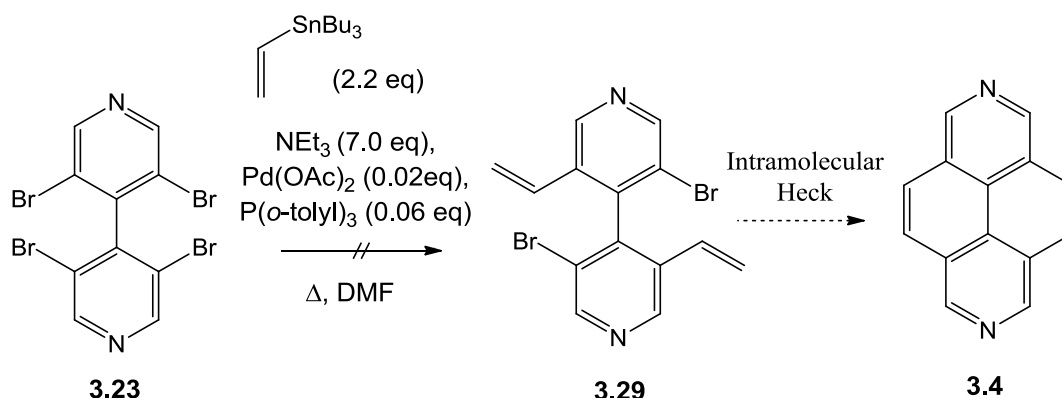
Scheme 3.13 Typical attempted Stille coupling of tetrabromobipyridine 3.23 with tributylvinyltin.

Analogous reactions were attempted using potassium vinyl trifluoroborate and a variety palladium sources, all proved unsuccessful.

Multiple attempts at Heck couplings also failed with a variety of substrates and ligands, as did attempts to employ Sonogashira chemistry. One possible reason for this is that the tetrabromobipyridine unit is too hindered to undergo oxidative addition with the palladium catalyst. This hypothesis is supported by a result subsequently published by Abboud *et al.* which saw preferential reaction at the 2 and 2' positions of 5,5'-dibromo-2,2'-dichloro-4,4'-bipyridine (Scheme 3.14).[91] This led us to attempt alternative methods of functionalizing these compounds.
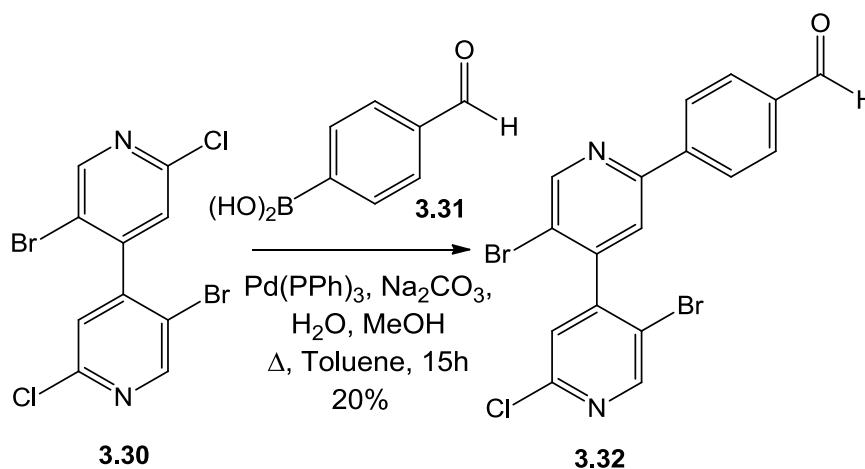

Scheme 3.14 Treatment of dibromodichlorobipyridine 3.30 with boronic acid 3.31 in the presence of palladium catalyst saw preferential reaction at the chloro-substituted position.

Organolithium chemistry can be used to introduce a wide variety of functionalities and seemed a promising prospect.[92] In order to determine if the substrate could undergo lithium-bromine exchange, a test reaction was performed using DMF to trap the resulting organolithium. Attempts to lithiate the tetrabromo compound using *n*-butyllithium were unsuccessful. However, when the tetrabromobipyridine was treated with one equivalent of *t*-butyllithium and the reaction quenched with DMF, monoformylated tribromobipyridine **3.33** was isolated in 55 % yield (Scheme 3.15).
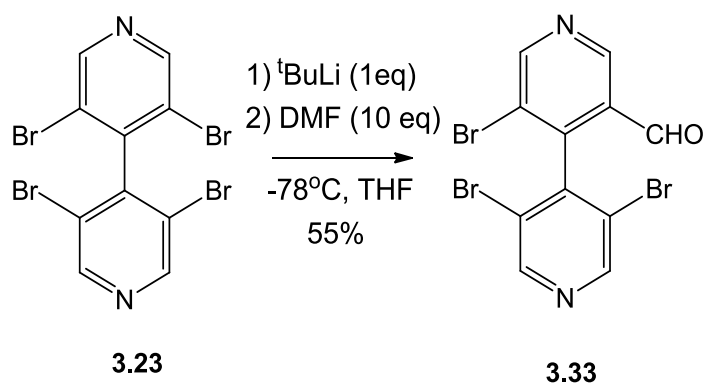
Scheme 3.15 Monolithiation of tetrabromobipyridine 3.23 and subsequent treatment with DMF gave monoformylated compound 3.33.

The success of this reaction led us to attempt to dilithiate the tetrabromobipyridine compound and introduce two formyl groups in one step. Upon treatment with two equivalents of *t*-butyllithium an unexpected result was achieved. A mass spectrum of the crude material from this reaction showed no presence of the desired product, but did indicate the presence of monobromo- and dibromobipyridines **3.35** and **3.34** (Scheme 3.16).
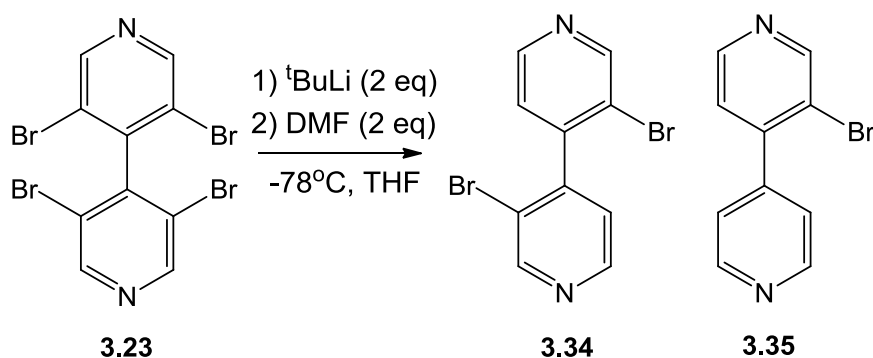
Scheme 3.16 Treatment of tetrabromobipyridine 3.23 with 2 equivalents of *t*-BuLi.

While somewhat unexpected, this result suggested that it is possible for multiple lithium-bromine exchanges to occur simultaneously on this molecule. The protonation of the lithiated species was presumably due to the presence of moisture in the reaction. This result provided a route to dibromobipyridine **3.34**, which is of interest for conductance measurements. This molecule cannot be synthesised using the previously described dimerisation procedure, which requires the presence of two halogen substituents in order to succeed. Attempts to employ an alternative procedure published by Durben *et al.*[93] had failed to yield the desired compound, instead consistently providing product **3.37** in low yield.
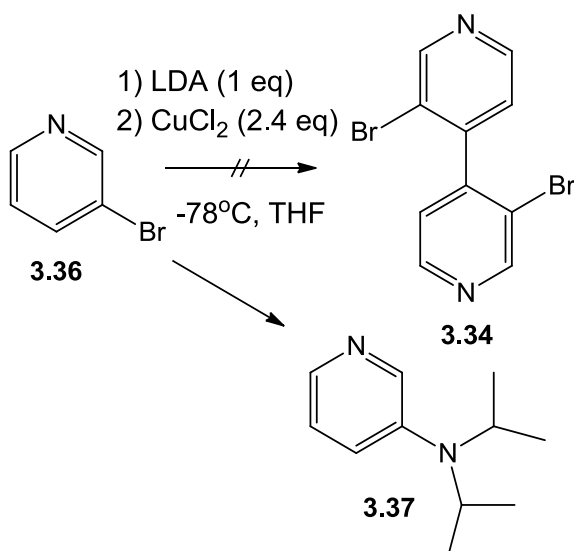
Scheme 3.17 Attempts to dimerize 3-bromopyridine 3.36 resulted in substitution product 3.37.

Upon treatment of tetrabromobipyridine **3.23** with two equivalents of *t*-BuLi, and subsequent quenching with H_2O, dibromobipyridine **3.34** was isolated in 53 % yield. With this promising result in hand we decided to test the extent to which the bipyridine unit could be lithiated. As previously stated a molecule bearing electron donating substituents was highly desirable, we therefore changed the electrophile used to trap the lithiated species to methyl iodide in attempt to introduce methyl substituents into the molecule. To our surprise, upon treatment with excess *t*-butyllithium and subsequent quench with methyl iodide, tetramethylbipyridine **3.38** was achieved in 44 % yield. Although this did contain a minor impurity it was pure enough for preliminary STM measurements. This result also highlights a new synthetic route to tetramethylbipyridine **3.38**, the only previous known synthesis of which is a low-yielding sodium-mediated coupling.[94]
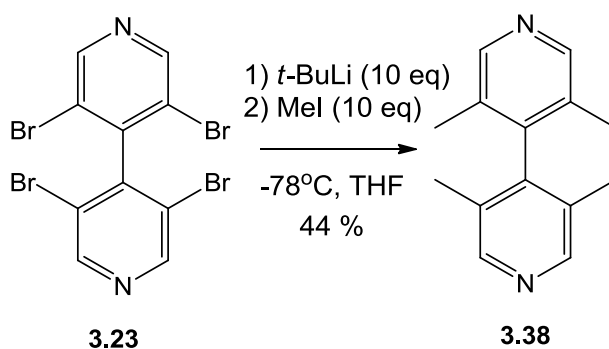
Scheme 3.18 Treatment of tetrabromobypryridine 3.23 with 10 equivalents of *t*-BuLi and subsequent addition of MeI yielded tetramethylbipyridine 3.38 in reasonable yield.

Having established a method for the lithiation of tetrabromobipyridine **3.23** we decided to apply the same conditions to tetrachlorobipyridine **3.20**. A simple test reaction using two equivalents of *t*-butyllithium and water as the electrophile saw the full recovery of starting material, thus suggesting that this compound does not undergo halogen-lithium exchange under similar conditions to the tetrabromo compound.

Since we had concluded that tetrabromobipyridine **3.23** was too hindered to undergo oxidative addition, we decided it was of interest to attempt some palladium catalysed coupling chemistry on dibromobipyridine **3.34**. Of particular interest was the previously mentioned tandem Stille/Heck sequence, which in this case would lead to 3,8-phenanthroline **3.39**. This analogue is another completely planar analogue of 4,4'-bipyridine, and would be of great interest for conductance measurements.
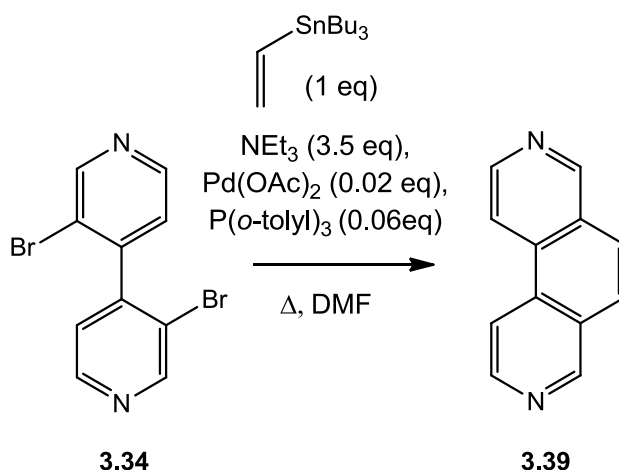
Scheme 3.19 Typical attempt at a tandem Stille-Heck reaction to synthesise phenanthroline 3.39.

Mass and NMR spectra of the crude reaction mixture of initial attempts at this reaction showed the correct molecular ion peak and chemical shifts for compound **3.39**. However attempts to isolate this provided only very low yields of approximately 2%. Furthermore, the isolated material was impure. This result shows that this is a potentially viable strategy for the synthesis of this important compound, but clearly requires much optimisation. Unfortunately time constraints did not allow further investigation.

3.4   Conclusion and Future Work

The aim of the synthetic work in this chapter was to provide analogues of 4,4'-bipyridine, both with and without functionalization at nitrogen, for use in STM experiments. Attempts were made to synthesise 2,7-diazapyrene by several synthetic routes. Whilst one route did provide this compound, the yield was very poor and the material impure.

A new method for the synthesis of tetrahalobipyridines was then studied and provided both 3,3',5,5'-tetrachloro-4,4'-bipyridine and 3,3',5,5'-tetrabromo-4,4'-bipyridine. The conductance measurements performed on these molecules is discussed in Chapter 4, along with the electrochemistry of their *N,N'*-dimethyl diiodide salts. Attempts were made to employ tetrabromobipyridine in a range of palladium-catalysed coupling reactions, all of which proved unsuccessful. However, subsequent attempts to perform lithium-bromine exchange reactions on this molecule proved it is possible to exchange all four bromines, providing a tetralithiated bipyridine unit. This chemistry highlights a powerful new method for the synthesis of highly functionalized 4,4'-bipyridines, and provided 3,3',5,5'-tetramethyl-4,4'-bipyridine and 3,3'-dibromobipyridine. The conductance measurements of these molecules are discussed in chapter 4. Further work is underway to probe the scope of this chemistry by varying the electrophile used to quench the lithiated species. One possibility is to trap the tetralithiated species with DMF, providing tetraformyl compound **3.40**. This could potentially be used in an intramolecular titanium mediated McMurry coupling to give 2,7-diazapyrene **3.4**.
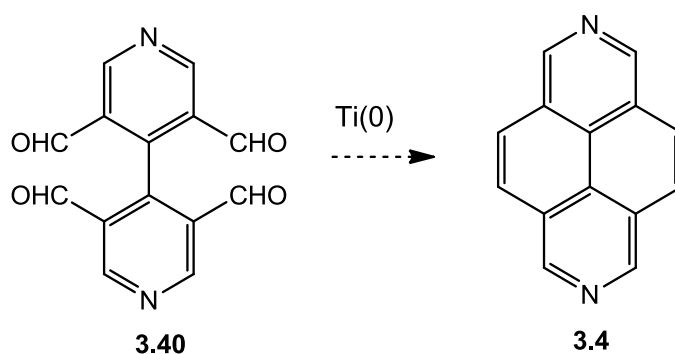
Scheme 3.20 Potential use of the McMurry Coupling to synthesise 2,7-diazapyrene 3.4.

Finally, attempts were made to employ 3,3'-dibromobipyridine in a palladium coupling reaction to synthesize 3,8-phenanthroline, which is a planar analogue of 4,4'-bipyridine. Initial attempts have shown that this reaction is potentially viable, but the product is isolated in very low yield and purity. Further work is needed to optimise this reaction, as well as investigate the scope.

Chapter 4

Electrochemical Behaviour and Conductance Studies of Novel Substituted 4,4'-Bipyridines

4.1   General Introduction and Aim

As discussed in the previous chapter, the conductance properties of 4,4'-bipyridines have raised questions regarding the role of torsion angle and ring twisting in conductance behaviour. It was therefore desirable to study the conductance properties of analogues of BIPY that are rotationally restricted.

The aims of this study were two-fold. Firstly, in collaboration with colleagues from Department of Physics, University of Bristol, we aimed to investigate the conductance behaviour of the four new BIPY analogues shown in Figure 4.1. The conductance measurements were undertaken by Doug Szumski using the STM BJ method. The torsion angles and energies of ring twisting in these molecules were qualitatively assessed using Spartan®.
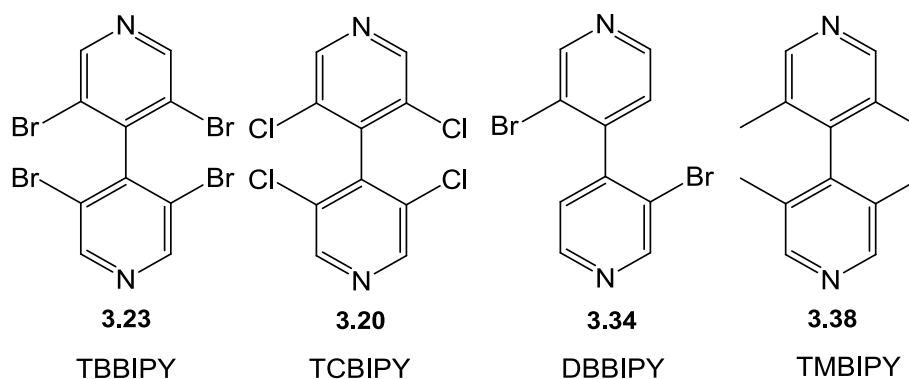
Figure 4.1 The structures of the four new analogues to be studied.

Secondly, the electrochemical behaviour of the dimethylpyridinium diiodide salts of tetrabromo- and tetrachlorobipyridines **3.23** and **3.20** were studied in order to determine if such systems can be employed in electrochemical STM experiments. In order to study conductance under electrochemical control, the molecule must exhibit electrochemically reversible redox switching. Furthermore, in an aqueous environment the potential window in which these occur is limited by hydrogen evolution at approximately -0.75 E/V *vs* SCE.

4.2   Torsion Angle and Ring Twisting

The torsion angles and energies of the ring twisting of each analogue have been qualitatively assessed. The Spartan® implementation of DFT was used to calculate the relative energies of 50 conformations of each analogue, each with a different torsion angle (Figure 4.2). A B3LYP hybrid exchange correlation function was used in conjunction with the 6-31G* basis set.

Figure 4.2 The highlighted atoms indicate those used to set the torsion angle of the bipyridine analogues in this study.

An energy minimization of each molecular conformation was performed using the molecular mechanics, Merck Molecular Force Field (MMFF) level of theory prior to the determination of the relative energy.
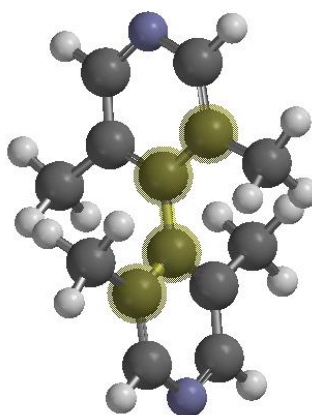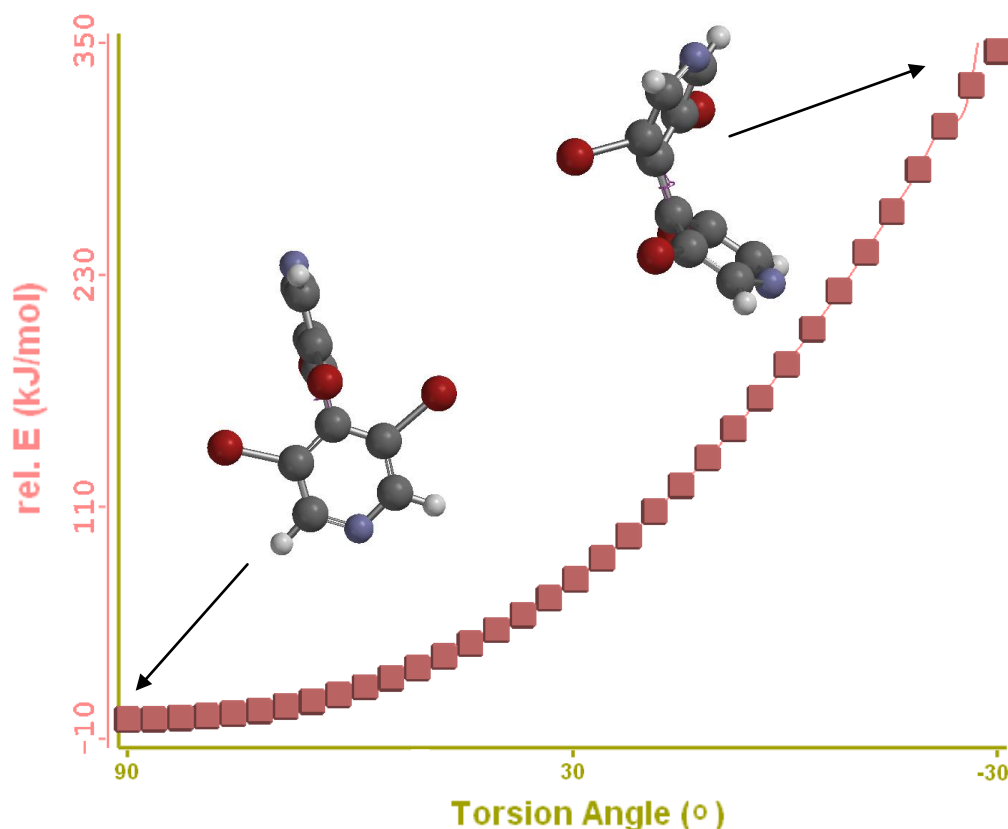

Figure 4.3 A plot of relative energy vs torsion angle for tetrabromobipyridine 3.23, starting at a torsion angle of 90° and sweeping through 120° to a torsion angle of -30°.

Figure 4.2 shows a plot of the energy of various conformations of tetrabromobipyridine **3.23** (TBBIPY). The torsion angle between the two rings was constrained to 90° and then swept through 180°, the conformation and energy was calculated at 50 points during this sweep. A sharp drop in relative energy was observed after 120°, this can be attributed to the minimization calculation changing the conformation to that of a much lower relative energy. The conformations after this point were therefore disregarded.

As would be predicted, the lowest value was observed for a torsion angle of 90°. As the angle decreases the molecule begins to bend as it twists, resulting in the very high energy conformation shown in Figure 4.3, which has a relative energy of 346 kJ/mol. This demonstrates that in this analogue the bulky bromine substituents result in the two rings being energetically locked out of the plane of each other, thus resulting in a dramatic decrease in the electronic interaction between the two π-

systems. This effective break in conjugation can be predicted to cause a dramatic decrease in the conductance of this molecule.
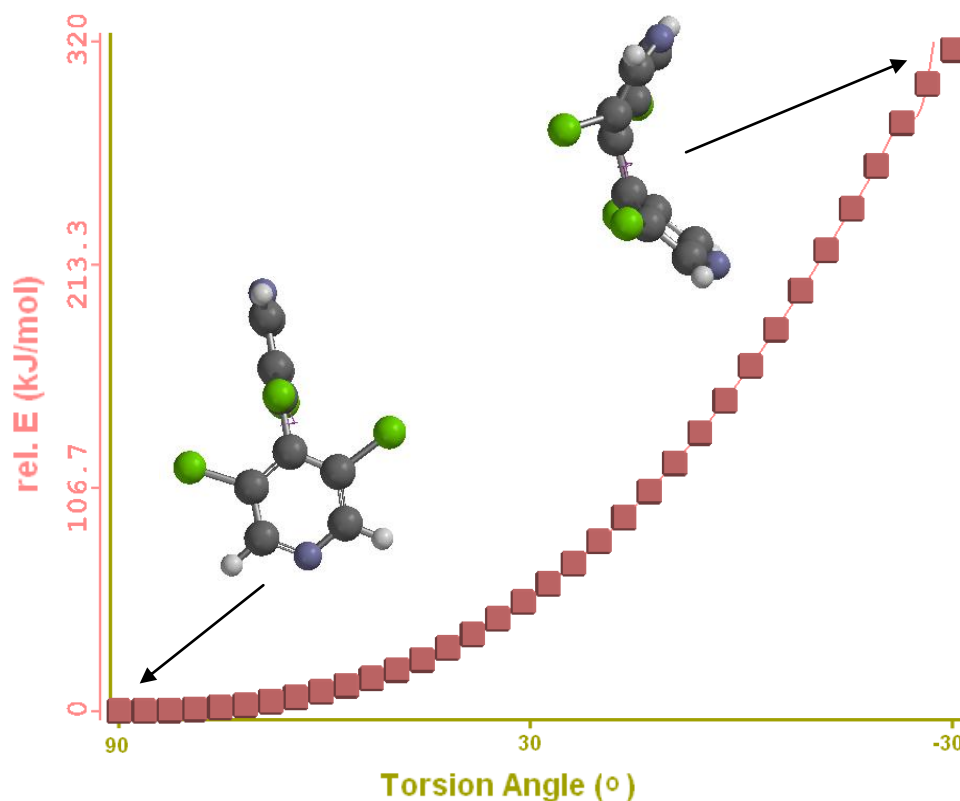
Figure 4.4 A plot of relative energy vs torsion angle for tetrachlorobipyridine 3.20.

A similar plot for tetrachlorobipyridine 3.20 (TCBIPY) is shown in Figure 4.4. It can be seen that this analogue exhibits the same behaviour, although the relative energy of the highest energy conformation is slightly lower, at 316 kJ/mol. This is in line with the behaviour that can be predicted when considering the relative sizes of bromine and chlorine atoms.

Similar experiments were performed for tetramethylbipyridine 3.38 (TMBIPY). In this case the torsion angle between the two rings was again constrained to 90°, and then swept through 270°; the conformation and energy was calculated at 50 points during this sweep. The resulting plot is shown in Figure 4.5. Again, a sharp drop in relative energy was observed after 120° and all results after this point were disregarded.
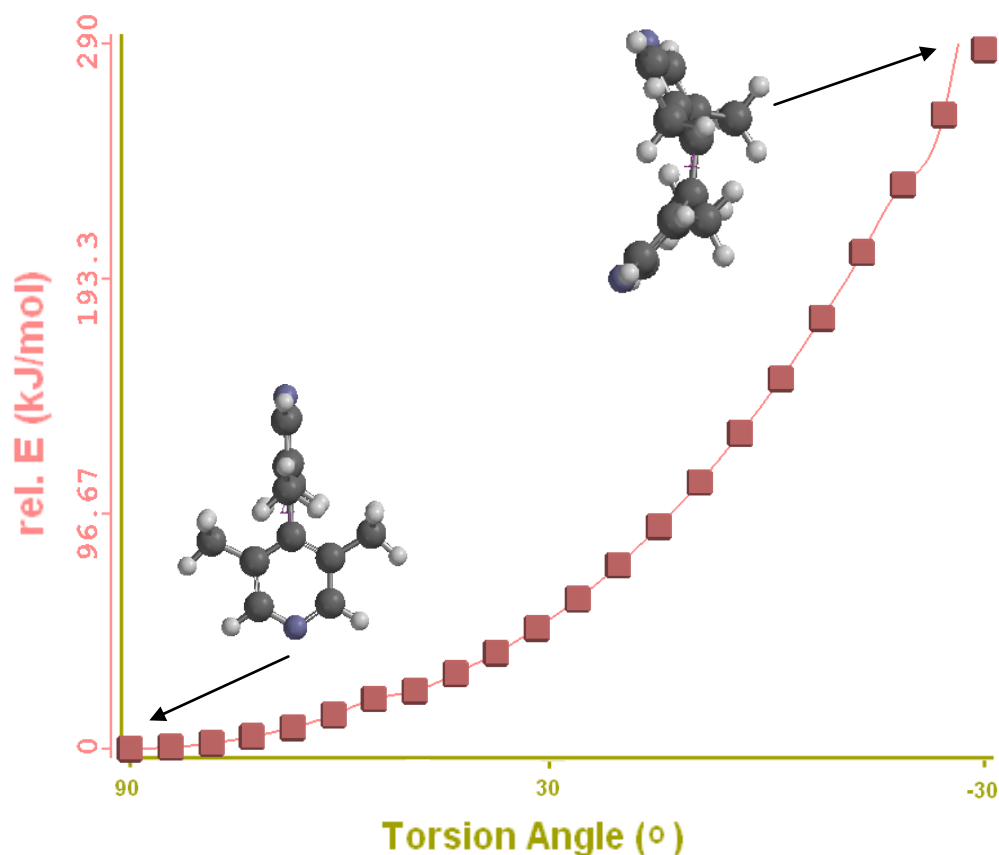
Figure 4.5 A plot of relative energy vs torsion angle for tetramethylbipyridine 3.38.

The behaviour is again similar to that of tetrabromobipyridine 3.23, with the two rings bending as the torsion angle decreases. The energy maximum in this case is 287 kJ/mol. This is much lower than that seen for the previous two analogues and suggests that factors other than size play a role in determining the rotational degrees of freedom. The extra repulsion seen in the two halogen containing analogues is possibly a result of the increased electron density in these atoms.

The final molecule to be studied was dibromobipyridine 3.34 (DBBIPY). In this case the torsion angle was set to 90° and swept through 180° in the same manner as the first two analogues. The resulting plot is shown in Figure 4.6.
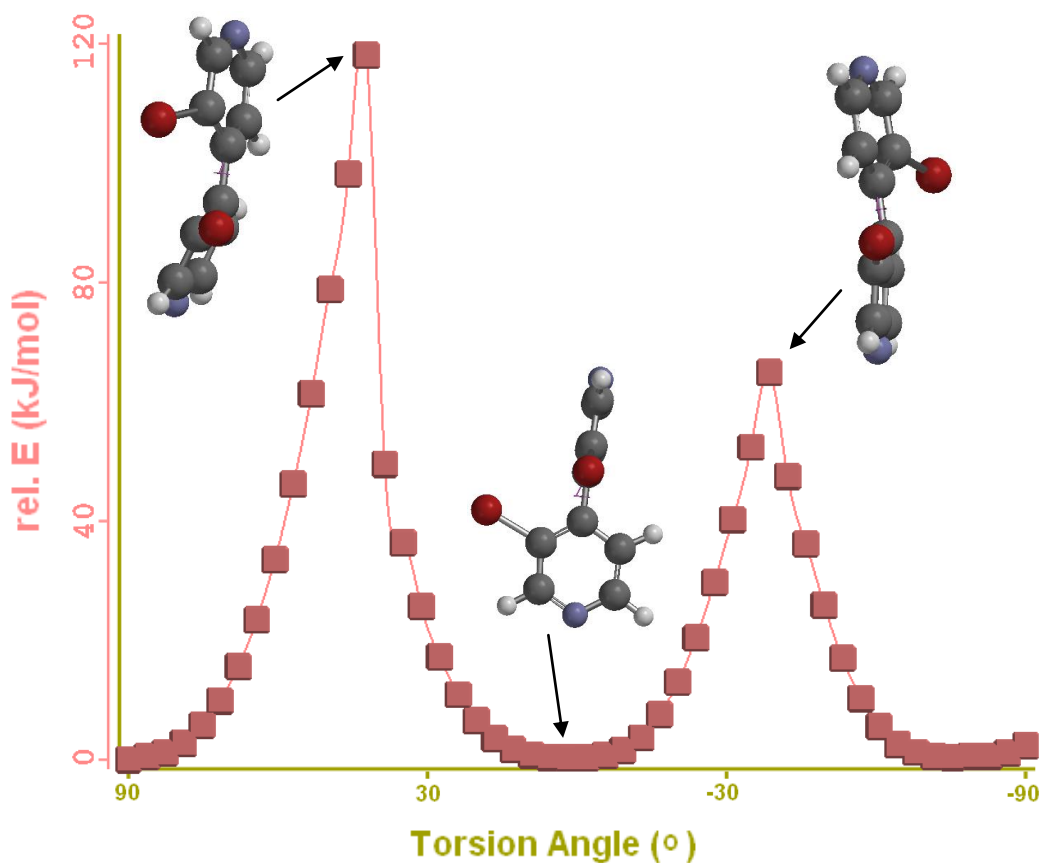
Figure 4.6 A plot of relative energy vs torsion angle for dibromobipyridine 3.34.

The plot for this molecule is very different from the previous three; two peaks of different energies can be seen. The larger of the two peaks corresponds to the conformation in which the two bromine atoms approach each other, and the smaller one corresponds with the case where a bromine and a hydrogen approach each other. These two peaks have relative energies of 118 and 65 kJ/mol respectively.

4.3   Conductance Measurements

The first molecule to be studied was tetrabromobipyridine **3.23**; the measurements were performed in mesitylene using the STM BJ method. As discussed in section 4.3, the torsion angle in this molecule is locked at 90° and the conductance would therefore be expected to be much lower than unsubstituted BIPY. Surprisingly, this molecule failed to form any molecular junctions. The acquired data is shown in Figure 4.7; the large signal to the left of the histogram (centred around 10^{-2} nA) is noise caused by the exponential decay of the current to zero. Several sharp peaks at high conductance values (the lowest can be seen at approximately 4 nA) can be seen in this histogram, corresponding to the quantum conductance of gold and multiples thereof, and proving that break junctions are indeed being formed in these experiments. Peaks showing molecular conductance are usually expected between 0 and 4 nA, and can be seen to be absent in this case. Since the binding of BIPY to a gold surface is widely accepted to be through the coordination of the pyridyl lone pair to gold, it was suggested that in this case the four bromine substituents deactivate the nitrogen and thus prevent the formation of molecular junctions. As the electronegativity of chlorine is greater than that of bromine, it can be predicted that TCBIPY should also fail to form molecular junctions.
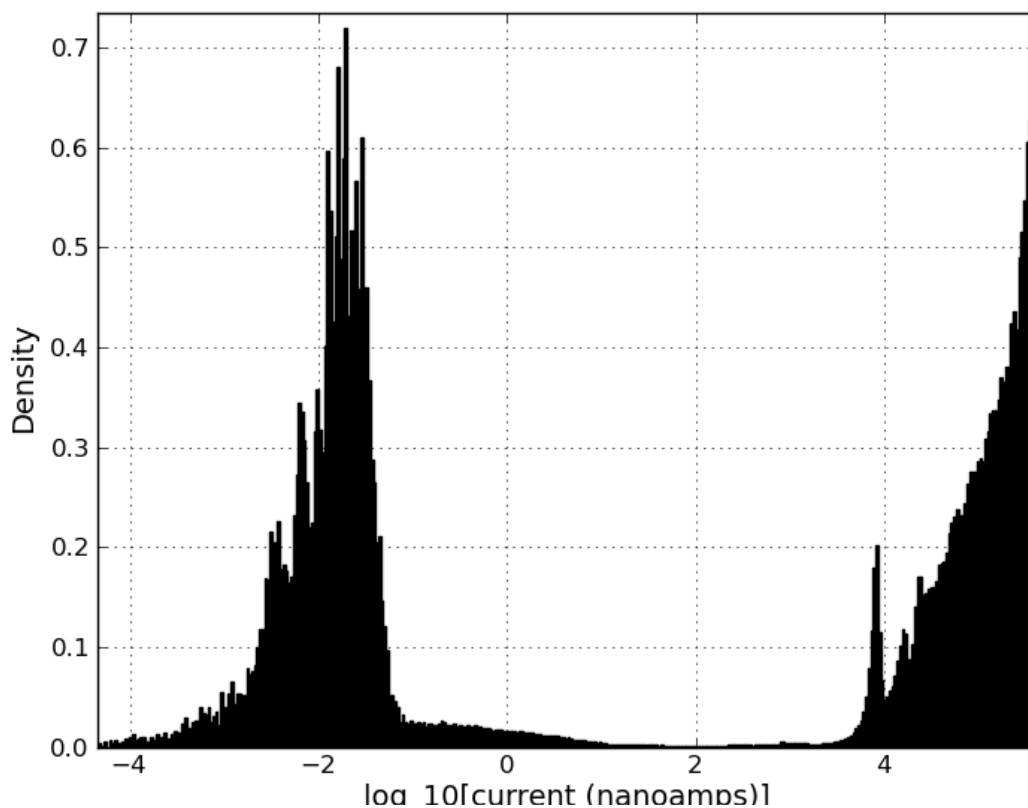

Figure 4.7 Histogram of approximately 1500 scans in the presence of TBBIPY 3.23 acquired using the STM BJ technique at a bias of 0.1 V, provided by Doug Szumski of Bristol University.

However, upon performing the same measurements with tetrachlorobipyridine **3.20** it was observed that this was not the case. This molecule did form molecular junctions, albeit with a much reduced probability compared with 4,4'-bipyridine. It is not clear why this analogue can form junctions when tetrabromobipyridine **3.23** cannot. The STM BJ data acquired for tetrachlorobipyridine **3.20** is shown in Figure 4.7 and suggests a conductance value of approximately 4.3 nS. In contrast to BIPY, only one conductance group was observed for TCBIPY **3.20**. As predicted in section 4.3, this value is much lower than that seen for BIPY; this could be attributed to the break in conjugation between the two aromatic rings. When considering this result it was suggested that the two conductance groups seen for BIPY could in fact be due to varying conformations of the molecule itself, as oppose to variation in the contact geometry of the nitrogen-gold bond. The higher of the two conductance groups would be observed when the conformation of the molecule allows the conjugation between the two ring π-systems to be partially or fully restored, which in the case of TCBIPY **3.20** could not occur.

Figure 4.8 Histogram of approximately 1500 scans for TCBIPY acquired using the STM BJ technique at a bias of 0.1 V, provided by Doug Szumski of Bristol University.

Previous measurements of BIPY under electrochemical control, which had shown an unusual gating as discussed in section 3.1, were performed in an aqueous sodium phosphate buffer at pH 6.8. Attempts to repeat these experiments for TCBIPY **3.20** were unsuccessful due to its insolubility in such solutions.
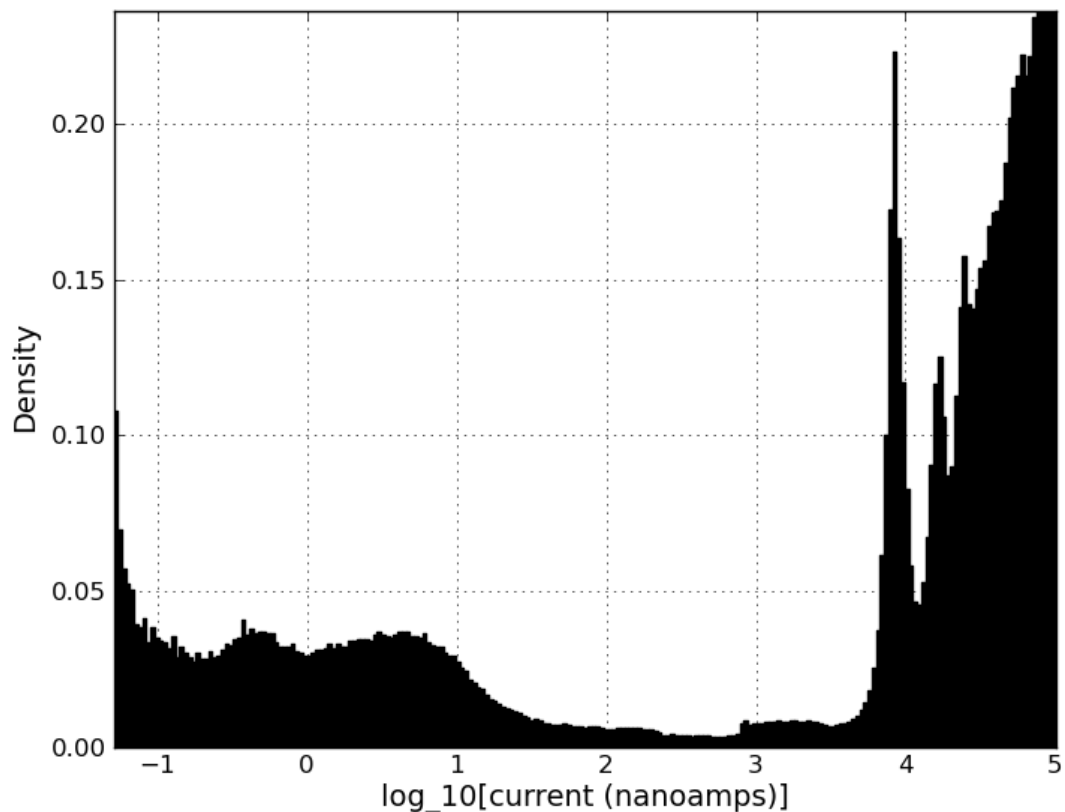
Figure 4.9 Histogram of approximately 1500 scans for DBBIPY acquired using the STM BJ technique at a bias of 0.1 V, provided by Doug Szumski of Bristol University.

Figure 4.8 shows the data acquired for dibromobipyridine **3.34** (DBBIPY); two clear conductance peaks can be seen and indicate conductance values of approximately 44 nS and 4.4 nS. Despite the steric bulk around this molecule being significantly reduced in comparison to TBBIPY **3.23**, the two rings are still unlikely to be even near to coplanar; the presence of two conductance values was therefore unexpected. This data suggests that the presence of high and low conductance groups is not due to variation in the conformation of the molecule.
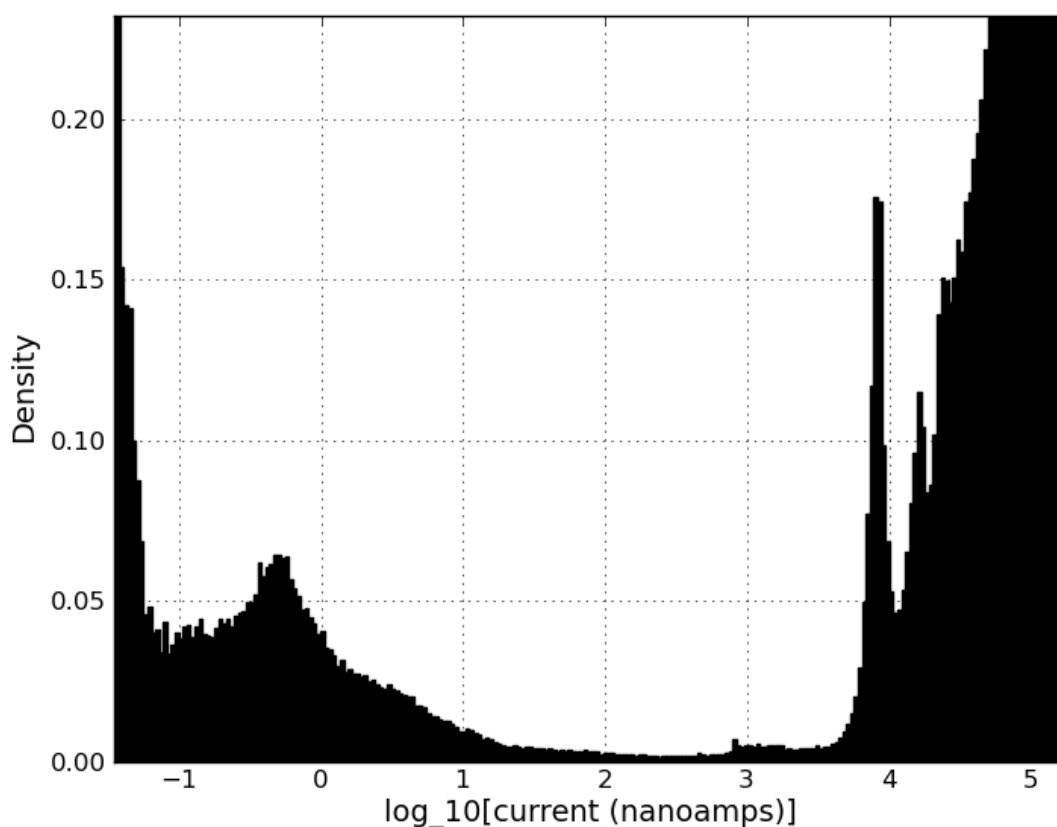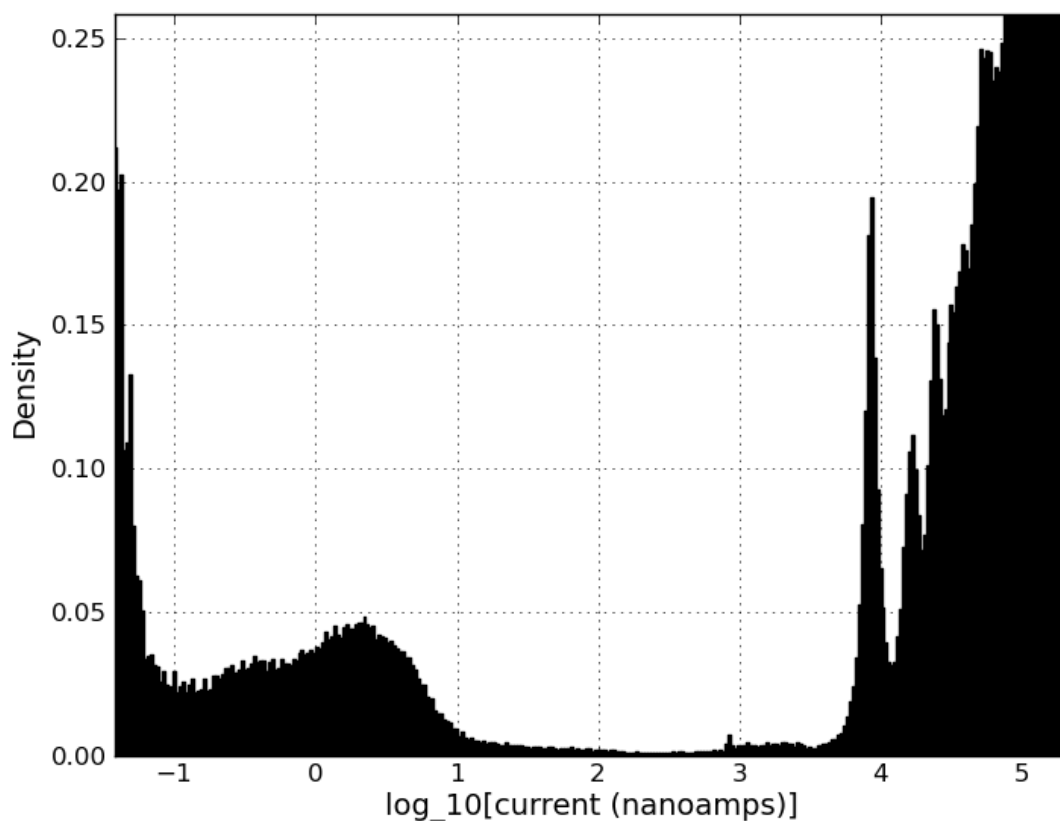
Figure 4.10 Histogram of approximately 700 scans for TMBIPY acquired using the STM BJ technique at a bias of 0.1V, provided by Doug Szumski of Bristol University.

The data acquired for TMBIPY **3.38** is shown in Figure 4.9; again two conductance peaks can be seen and indicate conductance values of approximately 23 nS and 3.4 nS. This final data set confirms that the presence of two conductance values is not due to varying torsion angles in the molecule. The magnitude of the conductance is significantly lower than observed for dibromobipyridine **3.34**. A summary of all the conductance data for these analogues is shown in Table 4.1.

	High Conductance (nS)	Low Conductance (nS)
BIPY	63	14
TCBIPY	-	4.3
DBBIPY	44	4.4
TMBIPY	23	3.4

Table 4.1 Summary of the conductance data.

Further investigation regarding the occurrence of the two separate conductance peaks observed for some analogues was required in order to study the relationship between them. Makk and coworkers recently introduced a novel statistical analysis method based on the two dimensional cross-correlation histogram analysis of conductance traces.[95] This type of analysis provides new information about the relationship of different conductance peaks that occur during the formation and evolution of single molecule junctions, and can provide both negative and positive correlations. A similar plot was produced from the conductance data of BIPY and is shown in Figure 4.11.
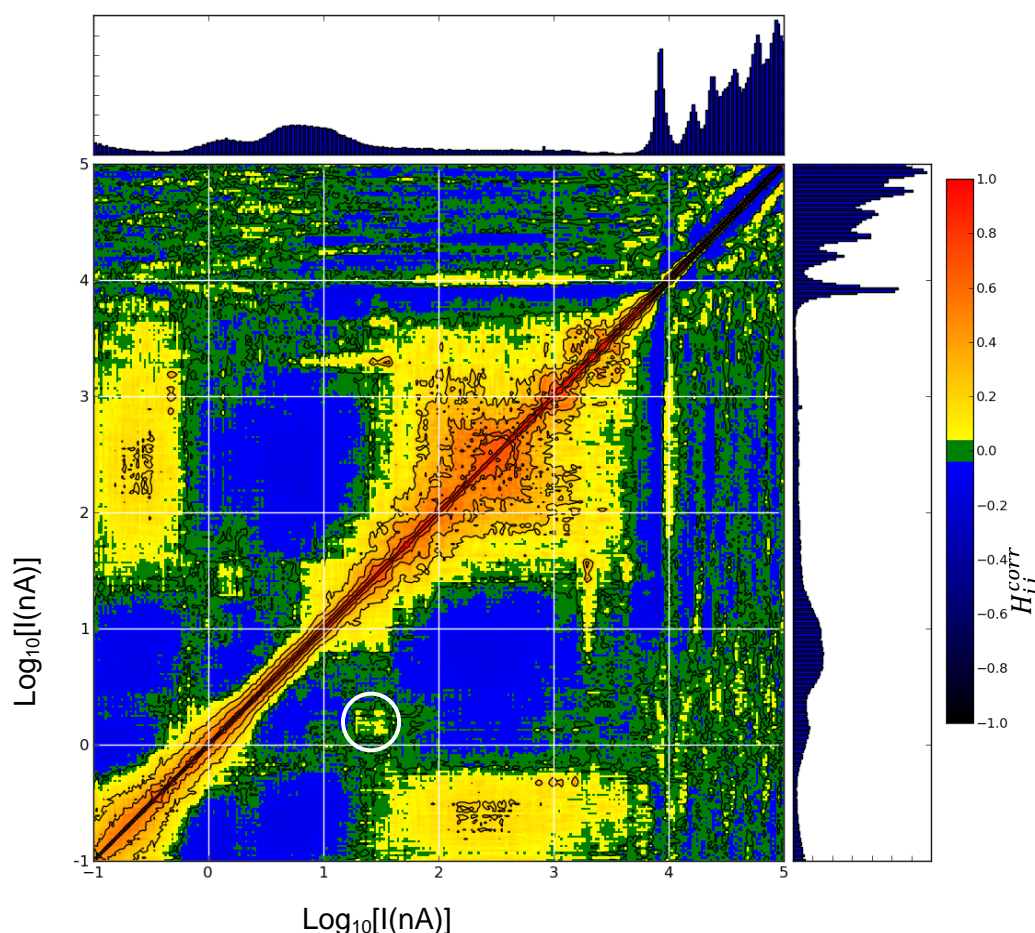
Figure 4.11 Correlation plot for the conductance data of BIPY, provided by Doug Szumski of Bristol University.

The scale to the right of this plot shows that negative correlations are represented with blue/black and positive correlations are represented by yellow/red. The area encased within the white circle highlights a positive correlation between the low conductance peak and the higher end of the high conductance peak; this suggests that the two conductance events often occur within a single conductance measurement. Whilst it is possible that the molecule is changing conformation during the individual measurements, this would likely produce one broad peak as

oppose to the two separate conductance peaks observed. This information led us to reconsider the theory of Venkataraman and coworkers, in which they attributed the two conductance groups to varying conformations of the Au-N bond. The higher of the two groups was attributed to increased coupling between the π-system of the molecule and the gold contact; it was therefore of interest to see if any correlation exists between the energies of the LUMO or HOMO orbitals and the conductance in these systems. The presence of substituents on an aromatic ring can have a dramatic effect on the electronic properties of a molecule, the substituted molecules presented in the current study therefore provide an excellent means of investigating any such correlation. The LUMO and HOMO energies were estimated using the Spartan® implementation of DFT; a B3LYP hybrid exchange correlation function in conjunction with 6-31G* basis set was employed (Table 4.2).

Molecule	Low Conductance (nS)	High Conductance (nS)	HOMO (eV)	LUMO (eV)
BIPY	14	63	-7.14	-1.87
TCBIPY	4.3	-	-7.36	-1.67
TMBIPY	3.4	23	-6.78	-0.74
DBBIPY	4.4	44	-7.16	-1.41

Table 4.2 Summary of the Spartan® and Conductance data of the BIPY analogues.

Plots of the low conductance data *vs.* both the HOMO and LUMO energies are shown in Figure 4.12; there does not appear to be any correlation of the conductance data to the energies of either of these frontier orbitals.
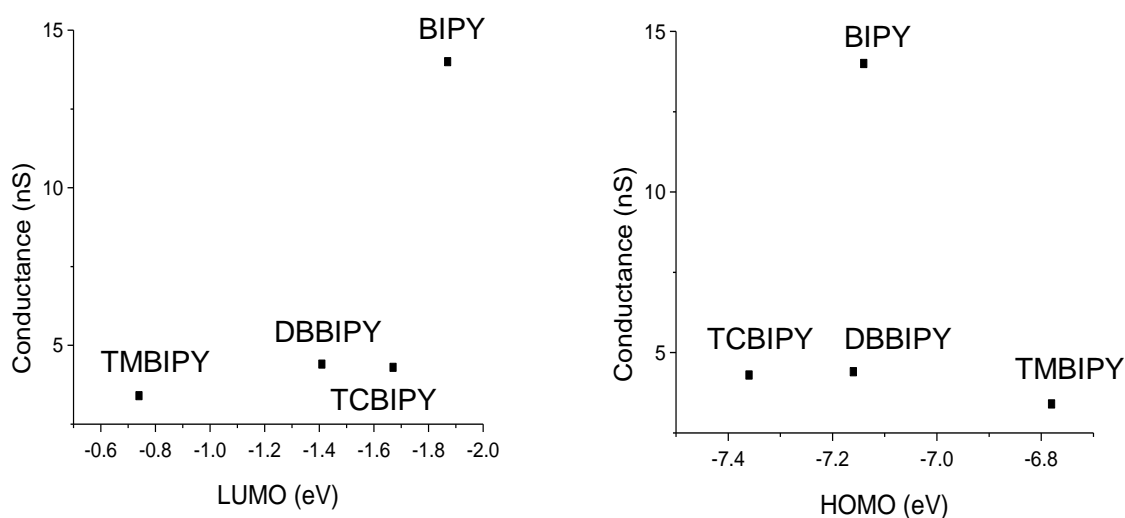
Figure 4.12 Plots of the frontiers orbitals of each analogue *vs* the lowest conductance values.

Plots of the high conductance values of BIPY, DBBIPY and TMBIPY *vs* both the LUMO and HOMO energies are shown in Figure 4.13; while no correlation can be seen in the HOMO plot, a clear correlation can be seen in the plot against LUMO energy. Several theoretical studies of gold-BIPY junctions have been reported, they consistently find that charge transport in such a system occurs *via* the LUMO of the molecule.[96-98] Since the orbital density of the LUMO lies largely on the π-system this correlation supports the idea that this particular conductance peak can be attributed to charge transport through the π-system. However, in order to confirm this correlation further data points are necessary. Further polyhalogenated bipyridine analogues, alongside analogues containing methoxy groups, would be of particular interest.

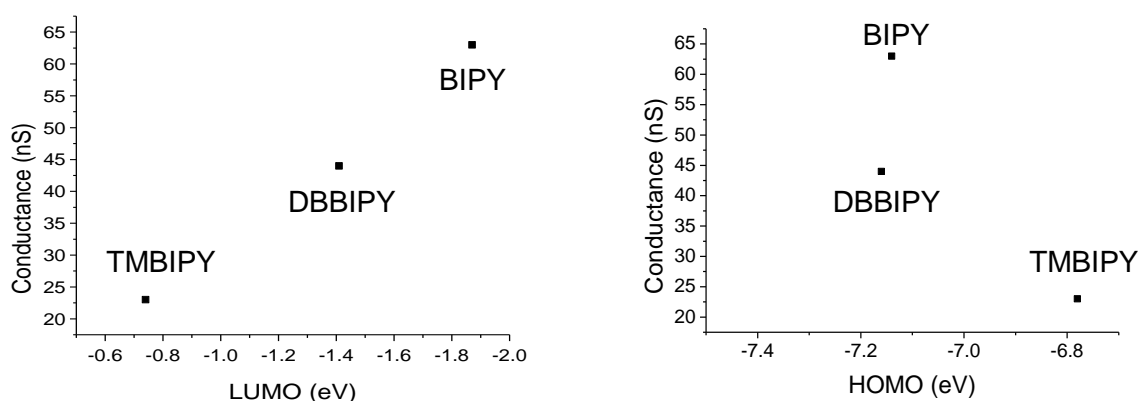**Figure 4.13 Plots of the frontiers orbitals of each analogue *vs* the higher conductance values.**

While the data presented provides further evidence regarding the nature of the junctions formed by BIPY and its analogues, it is still unclear as to why TCBIPY **3.20** only exhibits one conductance value and TBBIPY **3.23** fails to form molecular junctions.

4.4   Electrochemistry

Cyclic voltammetry experiments were performed in order to assess the suitability of the diiodide salts of dimethyltetrabromobipyridine (MBBIPY) **4.1** and dimethyltetrachlorobipyridine (MCBIPY) **4.2** for EC STM measurements. In order to perform as a 'switching molecule' these two analogues need to exhibit a clear and reversible redox state switching in their voltammograms. The electrochemistry of these analogues has not been studied previously. However, it is assumed that the redox reaction occuring is analogous to that previously seen for the unsubstituted bipyridine analogue, and is shown in Figure 4.13.

4.1   **4.1a**
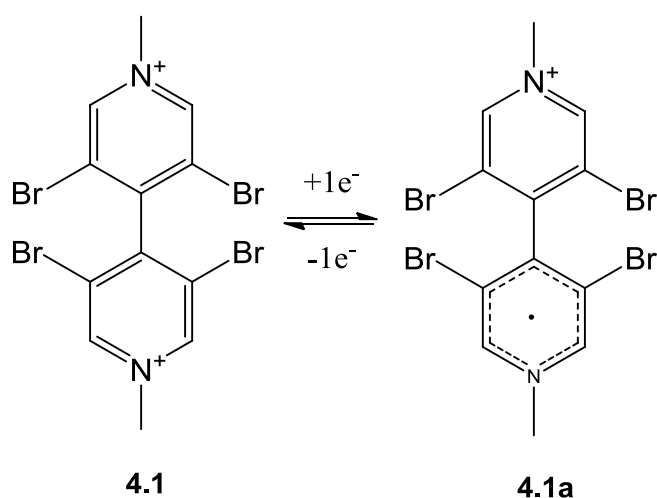
Figure 4.14 The MBBIPY^{2+}/MBBIPY$^{+\cdot}$ redox couple.

Initial voltammetry experiments for MBBIPY **4.1** were performed in an aqueous phosphate buffer and referenced to a saturated calomel electrode (SCE); Figure 4.15 shows a representative voltammogram. The negative potential window in this medium is limited to -0.75 E *vs* SCE due to hydrogen evolution at more negative potentials. A sample voltammogram is shown in Figure 4.15; no trace of a redox peak can be seen. A variety of sweep rates were employed in attempt to reveal a peak, but this proved unsuccessful. It was postulated that the potential window in these experiments was not sufficient to allow a redox transition in this molecule.
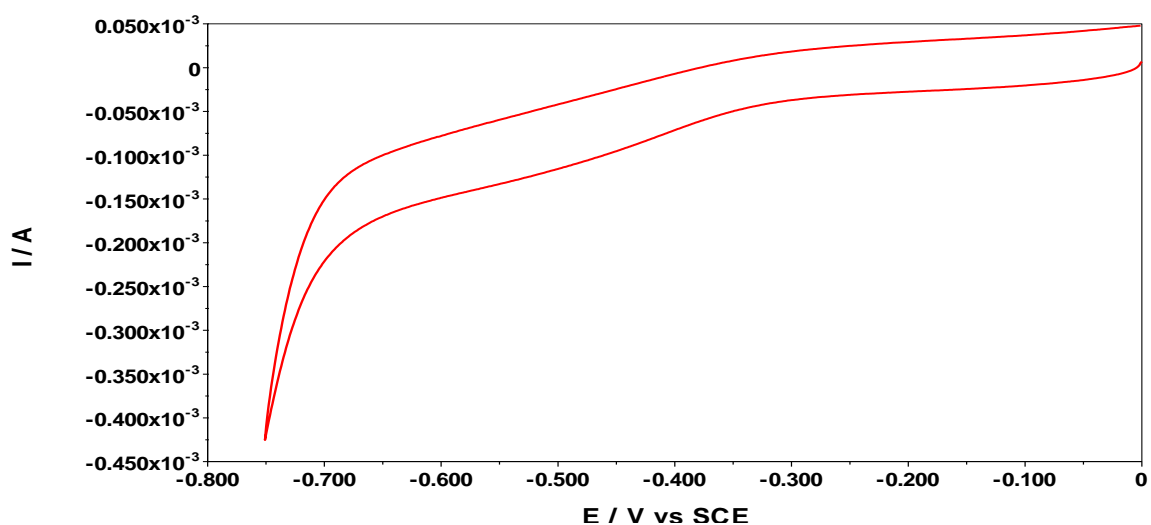
Figure 4.15 Cyclic voltammogram of MBBIPY 4.1 in aqueous phosphate buffer at pH 6.8 with a scan rate of 0.1 Vs^{-1}.

The voltammetry was repeated in freshly distilled dimethylformamide (DMF) with tetrabutylammonium hexafluorophosphate (TBAHFP) as an electrolyte; the potential can be swept to more negative values than in aqueous medium as hydrogen evolution is not a factor. Figure 4.16 shows the voltammogram acquired with a sweep rate of 0.05 Vs^{-1}.

Figure 4.16 Cyclic Voltammogram of MBBIPY 4.1 in dry DMF with TBAHFP electrolyte using a sweep rate of 0.05 Vs^{-1}.

A much clearer reduction peak can be seen at approximately -0.75 E/V vs. SCE (Figure 4.15) than in aqueous electrolytes (Figure 4.14), however a reverse peak for

114

this reduction cannot be clearly seen. A very broad peak can be seen in the reverse sweep at around -0.85 to -0.9 E/V *vs* SCE; this suggests a second reduction peak may occur at the negative end of the potential scan in Figure 4.15. It was noted at this point that although a dry organic solvent was employed the reference electrode itself is aqueous. If the reduced species is very labile it is possible that the electrode is acting as a source of water. A polypyrrole quasi reference electrode (PPy QRE)[99] was therefore employed in order to ensure the system was completely anhydrous.
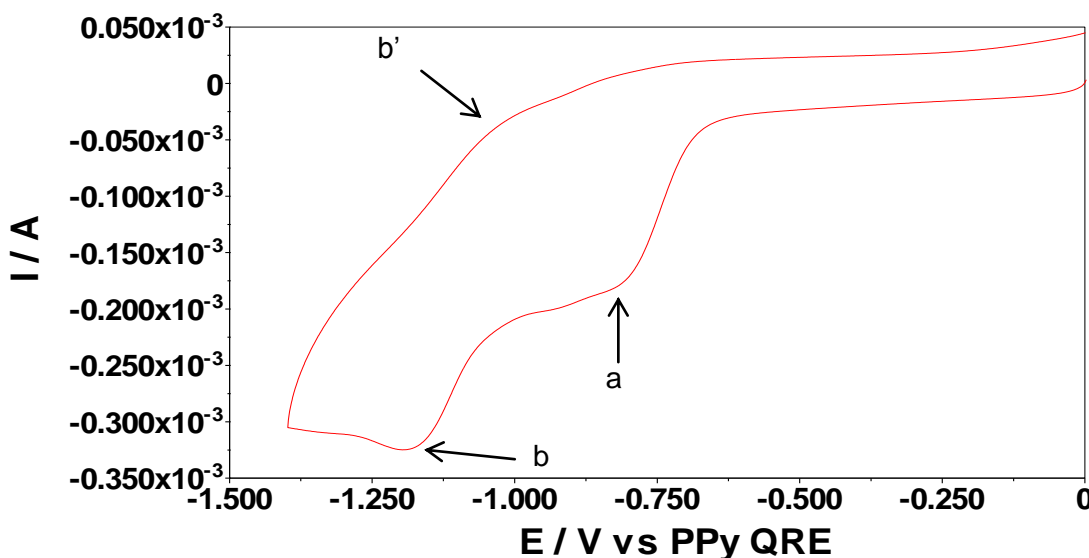
Figure 4.17 Cyclic voltammogram of MBBIPY in dry DMF with TBAHFP electrolyte referenced to a polypyrrole quasi reference electrode using a sweep rate of 0.05 Vs^{-1}.

The potential was swept even more negative in these experiments in order to try and observe a second reduction peak. Figure 4.17 shows the voltammogram acquired using a sweep rate of 0.05 Vs^{-1}. Two clear reduction peaks, a and b, can be seen at approximately -0.8 and -1.2 E/V *vs* PPy QRE respectively. A very weak and broad reverse peak, b', at approximately -1.0 E/V *vs* PPy QRE can also be seen; however there does not appear to be a reverse peak for the first reduction. This discounts the hypothesis of a reaction between the reduced species and the aqueous environment. It is not clear whether the irreversibility of the electrochemistry of this system is due to an EC type mechanism or slow electron transfer (see section 1.5.2). One possibility is the electrochemical reductive cleavage of a carbon-bromine bond; this has previously been reported in polyhalogenated benzenes.[100] Further electrochemical experiments are necessary to probe this system but are outside of the scope of this work. It can be concluded, however, that the system is not suitable for EC STM experiments.
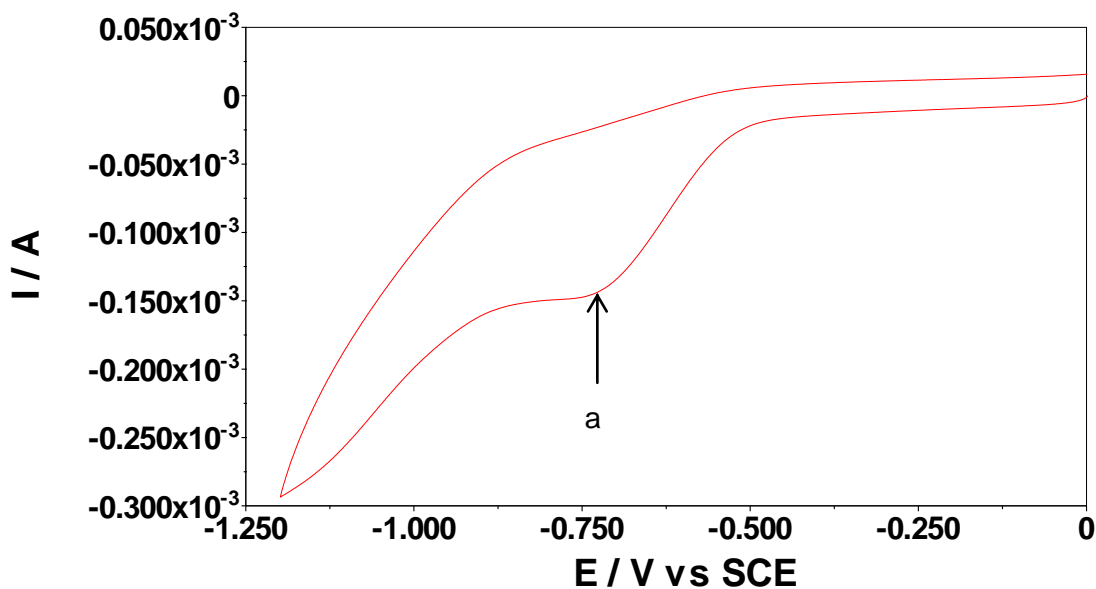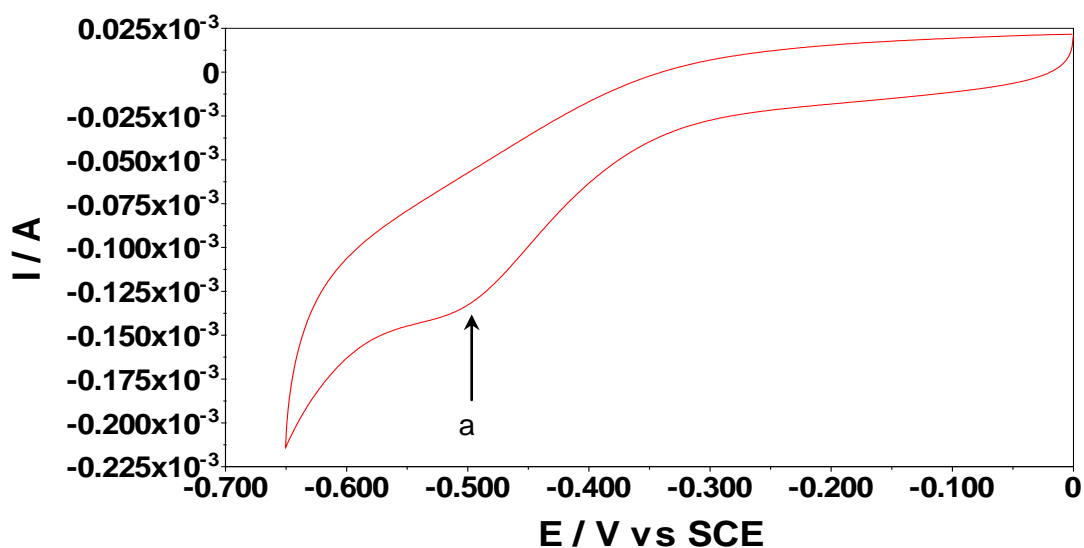
Figure 4.18 Cyclic voltammogram of MCBIPY in aqueous phosphate buffer at pH 6.8 with a scan rate of 0.05 Vs⁻¹.

Similar experiments were performed for MCBIPY **4.2**. A voltammogram acquired in aqueous phosphate buffer is shown in Figure 4.18. A clear reduction peak can be seen at approximately -0.5 E/V *vs* SCE. This peak is much more prominent than the analogous peak for MBBIPY **4.1**. A reverse peak, however, is again absent.
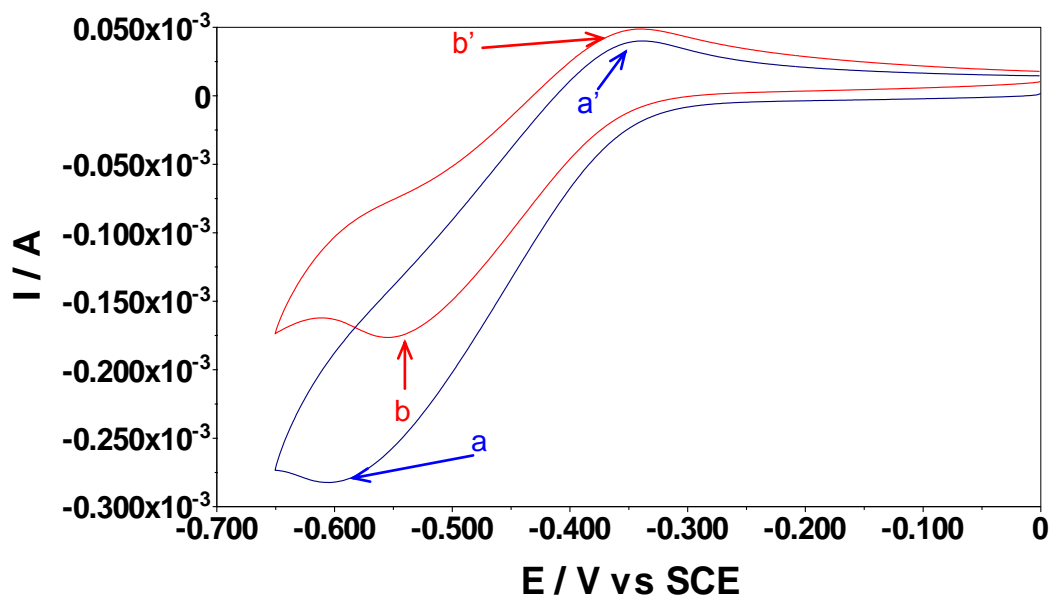
Figure 4.19 Cyclic Voltammogram of MCBIPY in dry DMF with TBAHFP electrolyte using sweep rates of 0.1 Vs⁻¹ (blue line) and 0.05Vs⁻¹ (red line).

The voltammetry was repeated in dry DMF with the TBAHFP electrolyte; Figure 4.19 shows the voltammograms acquired at sweep rates 0.1 and 0.05 Vs⁻¹. At the faster

sweep rate the reduction peak (a), at around -0.55 E/V *vs* SCE, is broad, but a clear reverse peak (a') can be seen at around -0.35 E/V *vs* SCE. Upon lowering the sweep rate the voltammogram becomes much more resolved and, more importantly, displays a clear oxidation peak (b'). As mentioned in section 1.5.3.1, one of the characteristics of a reversible voltammogram is the peak separation is independent of sweep rate, and is equal to 59/n mV at room temperature, where n is the number of electrons transferred. Analysis of the voltammograms shown in Figure 4.18 provides a non integer value of n. Furthermore, analysis of the magnitude of the peaks indicated that the oxidation peak was much smaller than the reduction peak. There are several explanations for such results:

- The rate of electron transfer is relatively slow, resulting in quasi reversible voltammetry.

- An ECE mechanism. This would involve an initial electrochemical reduction of MCBIPY **4.2**, followed by a chemical reaction and subsequent oxidation of the species thus formed.

- A combination of an EC mechanism and quasi-reversible behavior (for an explanation of this latter term see section 1.5.3.1). In this case the MCBIPY would be electrochemically reduced, and some of the resulting compound would undergo a further chemical reaction to a non-redox active product. The remainder is reoxidised, thus giving the reoxidation peaks a' and b'.

Since this system does not display the straightforward reversible behaviour required for EC STM it can be concluded that it is not suitable for this purpose. As in the case of MBBIPY **4.1**, further electrochemical experiments are necessary in order to determine the nature of the electrochemistry of this system, but are outside of the scope of this work.

4.5   Conclusions and Future Work

The single molecule conductance data of 4,4'-bipyridine (BIPY) and its analogues, along with a theoretical study of their conformations and orbital energies, has provided new insights into the structure-property relationships in this system. A correlation between the LUMO energy and the magnitude of the higher conductance value seen in some of the analogues has been demonstrated. This showed that the conductance increased as the LUMO energy approached the Fermi level of gold (-5.2 eV). However, the conductance data of more analogues is required in order to confirm this correlation. To this end the new synthetic route to substituted analogues of BIPY presented in Chapter 3 of this work could be employed.   Analogues containing differing levels of halogenation, as well as methoxy substituents, would be of particular interest since they would have a significant effect on the HOMO and LUMO energies.

The inability of TBBIPY **3.23** to form molecular junctions along with the lack of a second, high conductance peak for TCBIPY **3.20**, are thus far unexplained. The reduction in propensity to form Au-N bonds in BJ experiments is unlikely to be due to the deactivation of nitrogen by the relatively electronegative bromine, since this would also result in a complete lack of formation of TCBIPY molecular junctions. Since the size of a methyl group is similar to that of a bromine atom, the bulky nature of the bromine atoms is also unlikely to be the cause.

The electrochemistry of the dimethyl diiodide salts MBBIPY **4.1** and MCBIPY **4.2** has been studied in order to test the suitability of these redox units for STM conductance measurements under electrochemical control. The cyclic voltammetry of MBBIPY exhibited irreversible behaviour, thus proving the molecule to be unsuitable for this purpose. The voltammetry of MCBIPY showed similar behaviour in an aqueous environment, although oxidation peaks could be seen when the experiments were performed in dry DMF. As discussed, analysis of the voltammograms acquired   showed that this system is not fully reversible at the sweep rates used, and is therefore unsuitable for STM measurements. Determination of the nature of the redox processes occurring in these systems is outside of the scope of this work; however one possible way would be to isolate and characterise the reduced species.

Chapter 5

Conclusion

The development of small scale, silicon-based electronic components has revolutionized the world of electronics. The ability to incorporate thousands of components into one integrated circuit has allowed us to create devices of a size and complexity previously unimaginable. As we approach the limits of silicon-based electronics, it is essential that we are prepared to investigate new ideas in order to move forwards. The scale of current technology means that advances in this area will be reaching the molecular scale, and it is therefore imperative that we gain a thorough understanding of the principles of charge transport at this level.

The work presented herein has centred around two studies. The first sought to probe the relationship between conductance and molecular length in a series of straight chain alkanes containing a central phenyl ring. Prior to the work in this thesis one such molecule, and various substituted analogues thereof, had shown behaviour similar to what would be expected of a molecular equivalent of a double tunnelling barrier. The data presented demonstrates a remarkably low, and somewhat unexpected, dependence of this system on molecular length; this result contradicts the behaviour expected of a coherent transport mechanism. Moreover, the study of the orbital energies and densities of these molecules provides further evidence of a mechanism of conduction that is very different to that previously suggested for this system. Further, more detailed theoretical calculations are currently underway, as well as conductance experiments of a second, similar system. These new studies aim to provide new evidence regarding the nature of the charge transport mechanism in this type of molecular architecture.

The second study detailed the investigation of the conductance behaviour of 4,4'-bipyridine and some substituted analogues thereof; this study was presented in two parts. The first part reported the synthesis of a variety of analogues of 4,4'-bipyridine. This work highlights the potential of novel synthetic routes to polysubstituted bipyridines using both palladium and organolithium chemistry. There are few alternative synthetic routes to such compounds, and those that do exist tend

to use brutal reagents and conditions. The second part reported conductance data, electrochemical studies and theoretical calculations of properties of these molecules. The data presented provides new information regarding the relationship between electronic structure and conductance behaviour in this type of system. The apparent correlation between the LUMO and the higher of the two conductance values of these analogues is of particular interest, and support previous suggestions of conductance through the π-system; further data points to confirm this correlation are currently being sought.

Chapter 6

Experimental

6.1 General Experimental Procedures

6.1.1 Purification of reagents

All reactions that are air or moisture sensitive were performed in degassed and/or dry solvents in oven dried glassware. Solvents were degassed by bubbling with dry nitrogen for at least 15 minutes. All reagents were used as purchased or purified according to Perrin and Perrin.[101]

Acetic anhydride was dried over P_2O_5 and distilled under nitrogen.

Diethyl ether and THF were freshly distilled from sodium/benzophenone ketyl radical intermediate, under an anhydrous nitrogen atmosphere.

Dichloromethane was freshly distilled from calcium hydride under an anhydrous nitrogen atmosphere.

Di*iso*propylamine was distilled from sodium hydroxide and used immediately.

DMF was dried over $MgSO_4$ and distilled under reduced pressure.

n-Butyllithium and *t*-butyllithium were purchased from Sigma Aldrich as 1.6 M in hexanes and 1.7 M in pentane solutions respectively. Both were titrated against benzylbenzamide to a blue endpoint according to literature procedure.[102]

p-Toluene sulfonylchloride (tosyl chloride) was dissolved in the minimum amount of $CHCl_3$, filtered and diluted five times with petroleum ether (b.p. 40-60). The resulting solution was filtered and the filtrate reduced to very small volume *in vacuo*; the white crystals of pure tosyl chloride thus formed were collected by filtration and dried under vacuum.

Triphenylphosphine was recrystallised from DCM/hexanes.

6.1.2 Chromatography

Thin layer chromatography was performed on Merck silica gel 60 F-254 plates, compounds were visualized under UV where possible. UV inactive compounds were stained using iodine or aqueous $KMnO_4$ solution. Flash column chromatography was carried out using a variety of solvents on Aldrich technical grade silica gel; an air line or bellows were used to apply pressure.

6.1.3 Analytical Data

NMR spectra were recorded on a Bruker AMX 400 or Bruker DPX 400 (^{1}H, 400 MHz; ^{13}C, 100 MHz) and referenced to an internal standard of tetramethylsilane. Mass spectra were recorded on a Fisons Trio-1000 spectrometer using electron or chemical ionization. IR spectra were acquired neat on a Bruker FTIR in the range 4000-600cm^{-1}.

6.2   Synthesis

Preparation of 1,4-bis(6-chlorohex-1-yn-1-yl)benzene (2.2)
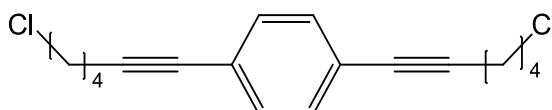
DIPA (50 ml) was degassed by bubbling N_2 through for 20 mins prior to the addition of 1,4-diiodobenzene (0.75 g, 2.30 mmol), [PdCl$_2$(MeCN)$_2$] (0.03 g, 0.12 mmol), triphenylphosphine (0.06 g, 0.23 mmol) and copper (I) iodide (0.01 g, 0.05 mmol). After flushing with N_2 for a further 10 mins, 6-chlorohex-1-yne (0.73 ml, 6.00 mmol) was added and the reaction was heated to reflux for 18 hours. The resulting suspension was cooled to room temperature and the solvent removed *in vacuo*. The residue was then redissolved in DCM (40 ml) and filtered under vacuum. The filtrate was purified by flash column chromatography (10-20% DCM/pet. ether) to yield the title compound as a yellow oil, which contained some inseparable impurities but was used directly for the next step (0.54 g, 76 %). ^{1}H NMR (CDCl$_3$, 400 MHz) δ: 7.30 (s, 4H, *aromatic*), 3.60 (t, J = 6.6Hz, 4H, C***H***$_2$Cl), 2.46 (t, J = 7.0Hz, 4H, CCC***H***$_2$), 2.01-1.91 (m, 4H), 1.82-1.71 (m, 4H); ^{13}C NMR (CDCl$_3$, 100 MHz) δ: 131.8 (*aromatic*),

123.5 (*aromatic*), 91.3 (*alkyne*), 81.4 (*alkyne*), 45.0 (*C*H$_2$Cl), 32.0, 26.2, 19.2; IR (neat) v$_{max}$: 2881 (ArC-H stretch), 1030 (s, C-Cl stretch) cm^{-1}; MS (CI+ (NH$_3$)) *m/z* 324.2 ([M+NH$_4$]$^+$, (^{35}Cl + ^{35}Cl) 100%), 326.1 ([M+NH$_4$]$^+$, (^{35}Cl + ^{37}Cl) 86%), 328.3 ([M+NH$_4$], (^{37}Cl + ^{37}Cl), 18%).

Preparation of 1,4-bis(6-chlorohexyl)benzene (2.3)
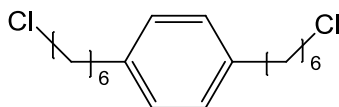
A solution of 1,4-bis(6-chlorohex-1-yn-1-yl)benzene **2.2** (0.53 g, 1.73 mmol) and Pd/C (10% by weight, catalytic) in MeOH (50 ml) was stirred under a H$_2$ atmosphere for 2 hours. The resulting suspension was filtered through a bed of celite and the filtrate concentrated under vacuum to give the desired product as a yellow oil (0.52 g, 94 %). ^{1}H NMR (CDCl$_3$, 400 MHz) δ: 7.08 (s, 4H, *aromatic*), 3.53 (t, J = 6.7Hz, 4H, C*H$_2$*Cl) 2.58 (t, J = 7.7Hz, 4H, C$_6$H$_5$-C*H$_2$*CH$_2$), 1.82-1.72 (m, 4H), 1.67-1.54 (m 4H), 1.51-1.41 (m, 4H), 1.41-1.30 (m, 4H); ^{13}C NMR (CDCl$_3$, 100 MHz) δ: 139.86 (*aromatic*), 128.3 (*aromatic*), 45.2 (*C*H$_2$Cl), 35.4, 32.3, 31.4, 28.6, 26.8; IR (neat) v$_{max}$: 2931 (ArC-H stretch) cm^{-1}; MS (CI+ (NH$_3$)) *m/z* 332.4 ([M+NH$_4$]$^+$, (^{35}Cl + ^{35}Cl) 100%), 334.4 ([M+NH$_4$]$^+$, (^{35}Cl + ^{37}Cl) 64%), 336.4 ([M+NH$_4$], (^{37}Cl + ^{37}Cl), 11%).

Preparation of S,S'-(1,4-phenylenebis(hexane-1,6-diyl))diethanethioate (2.4)
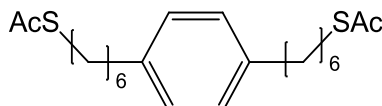
A stirred mixture of 1,4-bis(6-chlorohexyl)benzene **2.3** (0.55 g, 1.70 mmol), sodium iodide (0.26 g, 0.17 mmol) and potassium thioacetate (0.58 g, 5.10 mmol) in acetone (40 ml) was heated to reflux for 48 hours. The resulting brown solution was allowed to cool to room temperature and concentrated *in vacuo.* The residue was dissolved in DCM (40 ml), filtered and the filtrate purified by flash column chromatography (50% DCM/pet. ether) to yield the desired product as a brown solid (0.55 g, 85 %). ^{1}H NMR (CDCl$_3$, 400 MHz) δ: 7.07 (s, 4H, *aromatic*), 2.86 (t, J = 7.3Hz, 4H, C*H$_2$*SAc) 2.56 (t, J = 7.8Hz, 4H, C$_6$H$_5$-C*H$_2$*CH$_2$), 2.32 (s, 6H, C(O)C*H$_3$*), 1.64-1.51 (m, obs ass 8H), 1.43-1.28 (m, 8H); ^{13}C NMR (CDCl$_3$, 100 MHz) δ: 196.11 (*C*=O), 139.90 (*aromatic*), 128.26 (*aromatic*), 35.44 (*C*H$_2$SAc), 31.38, 30.68, 29.44, 29.14, 28.81, 28.69; IR (neat) v$_{max}$: 2924 (ArC-H stretch), 2854 (C-H stretch), 1685

(s, C=O stretch) cm^{-1}; MS (CI+ (NH$_3$)) *m/z* 412 ([M+NH4] 100%); Anal. Calcd. for C$_{22}$H$_{34}$O$_2$S$_2$ (394.12): C, 66.96%; H, 8.68%; Found: C, 66.50%; H, 8.83%.

Preparation of 4,4'-(1,4-phenylene)bis(but-3-yn-1-ol) (2.6)
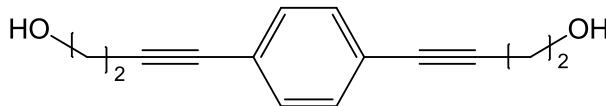

A solution of [PdCl$_2$(MeCN)$_2$] (0.03 g, 0.02 mmol), triphenylphosphine (0.06 g, 0.23 mmol) and copper iodide (0.01 g, 0.05 mmol) in DIPA (50 ml) was degassed with N$_2$ for 20mins before the addition of 1,4-diiodobenzene (0.75 g, 2.30 mmol). 3-Butyn-1-ol (0.45 ml, 6.00 mmol) was then added and the mixture refluxed overnight under N$_2$. The resulting black mixture was cooled to room temperature and the solvent removed *in vacuo*. The residue was treated with DCM (40 ml) and filtered before purification by flash column chromatography, eluting with 2.5% MeOH/DCM. The desired product was obtained as a yellow solid (0.38 g, 78 %). M.p. 122-125°C; ^{1}H NMR (CDCl$_3$, 400 MHz) δ 7.33 (s, 4H, *aromatic*), 3.82 (dd, J = 6.0, 6.3Hz, 4H, CH$_2$C**H$_2$**OH), 2.7 (t, J = 6.2Hz, 4H, CC**H$_2$**CH$_2$), 1.82 (t, J = 6.3Hz, 2H, O**H**); ^{13}C NMR (CDCl$_3$, 100 MHz) δ 131.6 (*aromatic*), 122.9 (*aromatic*), 88.1 (**C**CCH$_2$), 82.14 (C**C**CH$_2$), 61.1 (**C**H$_2$OH), 23.9 (**C**H$_2$CH$_2$OH); IR (neat) ν$_{max}$: 3301 (b, O-H stretch); 2979 (ArC-H stretch); 1037 (C-O stretch) cm^{-1}; MS (CI, +ve, NH$_3$) *mz* 215 ([M+H]$^+$, 100%).

Preparation of 4,4'-(1,4-phenylene)bis(butan-1-ol) (2.8)
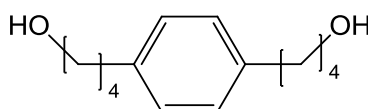
To a solution of 4,4'-(1,4-phenylene)bis(but-3-yn-1-ol) **2.6** (0.35 g, 1.60 mmol) in methanol (50 ml) was added Pd/C (10% by weight, catalytic), the reaction was then stirred under an atmosphere of H$_2$ for 3 hours. After this time the mixture was filtered through a bed of celite and the solvent removed under reduced pressure to give the title compound as a yellow solid (0.35 g, 97 %). M.p. 35-37°C; ^{1}H NMR (CDCl$_3$, 400 MHz) δ 7.10 (s, 4H, aromatic), 3.65 (t, J = 6.2Hz, 4H, C**H$_2$**OH), 2.60 (t, J = 7.4Hz, 4H, C**H$_2$**(CH$_2$)$_3$), 1.74-1.54 (m, 8H, C**H$_2$**C**H$_2$**CH$_2$OH); ^{13}C NMR (CDCl$_3$, 100 MHz) δ 140.1 (*aromatic*), 128.9 (*aromatic*), 63.3 (**C**H$_2$-OH), 35.6, 32.8, 28.0; IR (neat) ν$_{max}$: 3398 (b, O-H stretch); 2935 (ArC-H stretch); 1049, (C-O stretch) cm^{-1}; MS (CI, +ve, NH$_3$) *m/z* 240 ([M+NH$_4$]$^+$, 100%), 223 ([M+H]$^+$, 20%).

Preparation of 1,4-bis(bromobutyl)benzene (2.11)
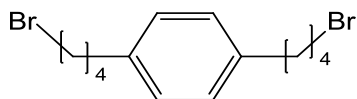
To a solution of DPPE (0.48 g, 1.20 mmol) in THF (40 ml) under N_2 was added dibromotetrachloroethane (0.78 g, 2.40 mmol). To the resulting white suspension was added 4,4'-(1,4-phenylene)bis(butan-1-ol) **2.8** (0.26 g, 1.20 mmol), after a short time the white solid had dissolved. The reaction was stirred overnight, after which time a white solid had precipitated. The suspension was filtered through a bed of celite and the solvent removed. The residue was purified by flash column chromatography (0-5%EtOAc/Pet. Ether) to yield the title compound as a white solid (0.31 g, 73 %). M.p. 37-39°C; ^{1}H NMR (CDCl$_3$, 400 MHz) δ 7.09 (s, 4H, *aromatic*), 3.42 (t, J = 6.8Hz, 4H, C***H***$_2$Br), 2.61 (t, J = 7.3Hz, 4H, C***H***$_2$(CH$_2$)$_3$), 1.94-1.85 (m, 4H, CH$_2$C***H***$_2$CH$_2$OH), 1.81-1.71 (m, 4H, Ar-CH$_2$C***H***$_2$-); ^{13}C NMR (CDCl$_3$, 100 MHz) δ 141.5 (*aromatic*), 130.6 (*aromatic*), 36.7 (***C***H$_2$-Br), 35.8, 34.4, 32.1; ν$_{max}$ (neat)/cm^{-1}: 2978 (ArC-H stretch), 640 (C-Br stretch); m/z (CI, +ve, NH$_3$) 346 ([M+H]$^+$, (^{79}Br + ^{79}Br), 28%), 348 ([M+H]$^+$, (^{79}Br + ^{81}Br), 50%), 350 ([M+H]$^+$, (^{81}Br + ^{81}Br), 25%); Anal. Calcd. for C$_{14}$H$_{20}$Br$_2$ (348.12): C, 48.30%; H, 5.79%;. Found: C, 48.54%; H, 5.70%.

Preparation of S,S'-(1,4-phenylenebis(butane-1,4-diyl))diethanethioate (2.12)
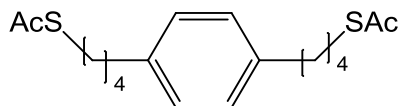
A solution of 1,4-bis(bromobutyl)benzene **2.11** (0.20 g, 0.58 mmol), sodium iodide (0.01 g, 0.06 mmol) and potassium thioacetate (0.20 g, 1.74 mmol) in acetone (20 ml) was refluxed under a N_2 atmosphere for 24 hours. The solvent was then removed under reduced pressure and the residue treated with DCM (20 ml) and filtered. The title compound was obtained by flash column chromatography (DCM, 100%) as a dark yellow oil (0.15 g, 77 %). ^{1}H NMR (CDCl$_3$, 400 MHz) δ 7.07 (s, 4H, *aromatic*), 2.89 (t, J = 6.9Hz, 4H), 2.58 (t, J = 7.3Hz, 4H), 2.32 (s, 6H, COC***H***$_3$), 1.74-1.58 (m, 8H); ^{13}C NMR (CDCl$_3$, 100 MHz) δ 196.3 (***C***=O), 139.9 (*aromatic*), 128.7 (*aromatic*), 35.3, 31.0, 30.9, 29.5, 29.4; ν$_{max}$ (neat)/cm^{-1}: 2935 (ArC-H stretch), 1689, (s, C=O stretch); m/z (CI, +ve, NH$_3$) 340 ([M+H]$^+$, 100%).

Preparation of 3, 3'-(1,4-phenylene)bis(prop-2-yn-1-ol) (2.5)

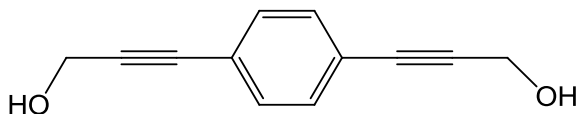DIPA (50 ml) was degassed by bubbling N_2 through for 20 mins prior to the addition of 1,4-diiodobenzene (0.75 g, 2.30 mmol), $[PdCl_2(MeCN)_2]$ (0.03 g, 0.12 mmol), triphenylphosphine (0.06 g, 0.23 mmol) and copper (I) iodide (0.01 g, 0.05 mmol). After flushing with N_2 for a further 10 mins, propargyl alcohol (0.35 ml, 6.00 mmol) was added and the reaction was heated to reflux for 18 hours. The resulting suspension was cooled to room temperature, filtered under vacuum and the residue washed with DCM (40 ml). The filtrate was then concentrated under vacuum and purified by flash column chromatography (50% EtOAc/Pet. Ether) to yield the title compound as yellow crystals (0.37 mg, 86 %). M.p. 108-111°C; ^{1}H NMR (CDCl$_3$, 400 MHz) δ: 7.38 (s, 4H, *aromatic*), 4.50 (s, 4H, C**H**$_2$OH); ^{13}C NMR (CDCl$_3$, 100 MHz) δ: 131.6 (*aromatic*), 122.7 (*aromatic*), 89.0 (*alkyne*), 85.26 (*alkyne*), 51.7 (**C**H$_2$OH); IR (neat) v_{max}: 3359 (br, O-H stretch), 1030 (s, C-O stretch) cm^{-1}; MS (CI+ (NH$_3$)) *m/z* 187.2 ([M+H]$^+$, 31%), 186.1 ([M+H-H]$^+$, 100%).

Preparation of 3, 3'-(1,4-phenylene)bis(propan-1-ol) (2.7)
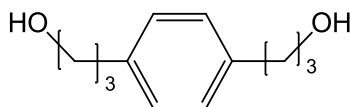
A solution of 3, 3'-(1,4-phenylene)bis(prop-2-yn-1-ol) **2.5** (0.35 g, 1.88 mmol) and Pd/C (10% by weight, catalytic) in EtOAc (50 ml) was stirred under a H$_2$ atmosphere for 96 hours. The resulting suspension was filtered through a bed of celite and the filtrate concentrated under vacuum to give the desired product as a yellow powder (0.36 g, 97 %). M.p. 47-50°C; ^{1}H NMR (CDCl$_3$, 400 MHz) δ: 7.13 (s, 4H, *aromatic*), 3.68 (t, J = 6.4Hz, 4H, C**H**$_2$OH) 2.68 (t, J = 7.7Hz, 4H, CC**H**$_2$CH$_2$), 1.93-1.84 (m, 4H, CH$_2$C**H**$_2$CH$_2$); ^{13}C NMR (CDCl$_3$, 100 MHz) δ: 139.31 (*aromatic*), 128.5 (*aromatic*), 62.4 (**C**H$_2$OH), 34.28 (CH$_2$**C**H$_2$CH$_2$), 31.65 (C**C**H$_2$CH$_2$); IR (neat) v_{max}: 3329 (br, O-H stretch), 2931 (ArC-H stretch), 1061 (s, C-O stretch) cm^{-1}; MS (CI+ (NH$_3$)) *m/z* 212 ([M+NH$_4$]$^+$, 100%).

Preparation of 1,4-phenylenebis(propane-3,1-diyl) bis(4-methylbenzensulfonate) (2.10)
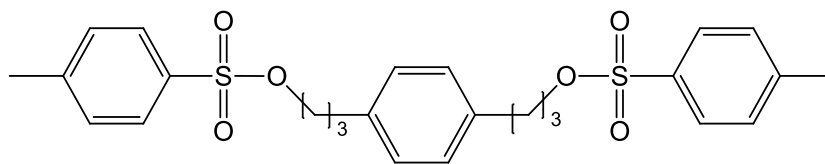

Triethylamine (0.17 ml, 1.2 mmol) and 4-toluenesulfonylchloride (0.23 g, 1.2 mmol) were added to a solution of 3, 3'-(1,4-phenylene)bis(propan-1-ol) **2.7** (0.09 g, 0.46 mmol) in dry DCM (10 ml) under N_2 at 0°C. The reaction was then allowed to warm to room temperature and stirred overnight. The crude reaction mixture was purified by flash column chromatography (100% DCM). The resulting product contained trace triethylamine and was therefore redissolved in DCM and washed with water. The combined organics were dried over $MgSO_4$ and concentrated *in vacuo* to yield the desired product as an off white solid (0.08 g, 36 %).^{1}H NMR ($CDCl_3$, 400 MHz) δ: 7.79 (d, J = 8.1Hz, 4H, Ar-**H** *(ortho)*), 7.35 (d, J = 8.1Hz, 4H, Ar-**H** *(meta)*), 6.95 (s, 4H, *aromatic*), 4.02 (t, J = 6.3Hz, 4H, CH_2C**H_2**OTs), 2.60 (t, J = 7.7Hz, 4H, C_6H_4C**H_2**), 2.50 (s, 6H, tosyl C**H_3**), 1.97-1.88 (m, 4H, CH_2C**H_2**CH_2); ^{13}C NMR ($CDCl_3$, 100MHz) δ: 144.8 (*aromatic*), 138.2, 133.1, 129.9, 128.5, 127.9, 69.6 (C**H_2**-OH), 31.0, 30.5, 21.7 (**C**H_3); IR (neat) v_{max}: 2900 (ArC-H stretch), 1103 (s, C-O stretch) cm^{-1}; MS (ES+ (MeOH)) *m/z 525* ([M+Na]+, 100%).

Preparation of S,S"-(1,4-phenylenebis(propane-3,1-diyl)) diethanethioate (2.9)
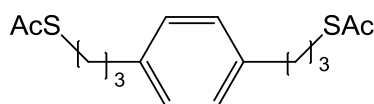
A solution of 1,4-phenylenebis(propane-3,1-diyl) bis(4-methylbenzensulfonate) **2.10** (0.08 g, 0.16 mmol), sodium iodide (0.01 g, 0.06mmol) and potassium thioacetate (0.04 g, 0.36 mmol) in acetone (25 ml) was refluxed under a N_2 atmosphere for 72 hours. The solvent was then removed under reduced pressure and the residue treated with DCM (20 ml) and filtered. The title compound was obtained by flash column chromatography (DCM, 100%) as a light brown oil (0.03 g, 66 %). ^{1}H NMR ($CDCl_3$, 400 MHz) δ: 7.07 (s, 4H, *aromatic*), 2.88 (t, J = 7.3Hz, 4H, C**H_2**SAc) 2.65 (t, J = 7.6Hz, 4H, C_6H_4C**H_2**), 2.34 (s, 6H, COC**H_3**), 1.94-1.82 (m, 4H, CH_2C**H_2**CH_2); ^{13}C NMR ($CDCl_3$, 100 MHz) δ: 195.9 (**C**=O), 138.8 (*aromatic*), 128.5 (*aromatic*), 34.4, 31.1, 30.7, 28.6; IR (neat) v_{max}: 2924 (ArC-H stretch), 1689 (s, C=O stretch) cm^{-1}; MS (CI+ (NH_3)) *m/z* 328.1 ([M+NH_4]+, 100%), 311.1 ([M+H]+, 20%).

Preparation of ((8-bromooctyl)oxy)(*tert*-butyl)diphenylsilane (2.25)
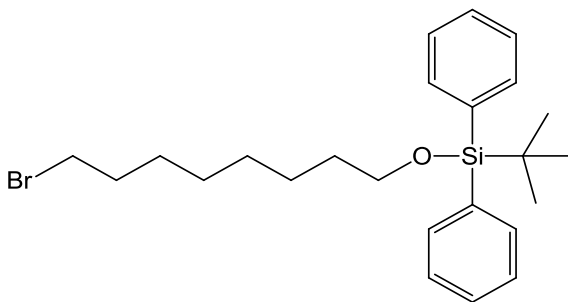
A solution of 1*H*-imidazole (1.50 g, 5.60 mmol), DMAP (0.96 g, 0.20 mmol) and 8-bromooct-1-ol (2.36 ml, 2.80 mmol) in DCM (30 ml) was cooled to 0°C under N_2 prior to the dropwise addition of TBDPSCl (4.4 ml, 4.20 mmol). The solution was allowed to warm to room temperature and stirred for 2 hours, during this time a white precipitate formed. The mixture was then diluted with DCM (20 ml), washed with water and dried over $MgSO_4$. The residue was purified by column chromatography (0-5% EtOAc/Pet. Ether) to yield the title compound as a colourless oil (0.72 g, 15 %). ^{1}H NMR (CDCl$_3$, 400 MHz) δ: 7.70-7.64 (m, 4H, *aromatic*), 7.45-7.34 (m, 6H, *aromatic*), 3.65 (t, J = 6.5Hz, 2H, C*H*$_2$O), 3.40 (t, J = 6.8Hz, 2H, C*H*$_2$Br), 1.89-1.79 (m, 2H), 1.59-1.51 (m, 2H), 1.45-1.23 (m, 8H), 1.05 (s, 9H, 3 x CC*H*$_3$); ^{13}C NMR (CDCl$_3$, 100 MHz) δ: 136.0, 134.6, 130.0, 127.0, 64.3 (*C*H$_2$O), 34.4, 33.2, 32.9, 29.5, 29.1, 28.5, 27.3, 26.1, 19.6.

Preparation of 8-(benzyloxy)octan-1-ol (2.14)
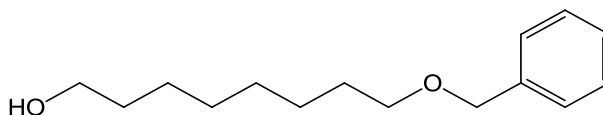
To a suspension of NaH (60% dispersion in mineral oil, 0.33 g, 13.70 mmol) in dry THF (50 ml) at 0°C was added 1,8-octanediol (2.00 g, 13.70 mmol). Benzyl bromide (1.60 ml, 13.70 mmol) was then added dropwise and the reaction allowed to warm to room temperature. After heating to reflux for approximately 12 hours the reaction was cooled, water (40 ml) added and the aqueous extracted with DCM (3 x 50 ml). The combined organics were dried over $MgSO_4$ and the solvent removed. The residue was purified by flash column chromatography (10-50% EtOAc/Pet. Ether) to yield the title compound as a clear oil (1.03 g, 32 %). ^{1}H NMR (CDCl$_3$, 400 MHz) δ: 7.38-7.24 (m, 5H, *aromatic*), 4.50 (s, 2H, CH$_2$OC*H*$_2$), 3.67-3.59 (m, 2H), 3.46 (t, J = 6.6Hz, 2H, C*H*$_2$OCH$_2$C$_6$H$_5$), 1.70-1.20 (m, 12H); ^{13}C NMR (CDCl$_3$, 100 MHz) δ: 138.7, 128.3, 127.6, 127.5, 72.9, 70.5, 63.0, 32.8, 29.7, 29.4, 29.4, 26.1, 25.7; IR

(neat) v_{max}: 3424 (br, O-H stretch), 2931 (s, C-H stretch), 2858 (s, C-H stretch), 1099 (s, C-O stretch) cm^{-1}.

Preparation of (((8-bromooctyl)oxy)methyl)benzene (2.15)
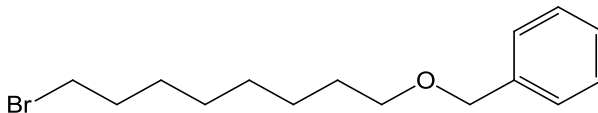
To a solution of DPPE (0.42 g, 1.05 mmol) in THF (20 ml) under N_2 was added dibromotetrachloroethane (0.68 g, 2.10 mmol). To the resulting white suspension was added 8-(benzyloxy)octan-1-ol **2.14** (0.50 g, 2.10 mmol), after a short time the white solid had dissolved. The reaction was stirred overnight, after which time a white solid had precipitated. The suspension was filtered through a bed of celite and the solvent removed. The residue was purified by flash column chromatography (20%EtOAc/Pet. Ether) to yield the title compound as a colourless oil (0.42 g, 67 %). ^{1}H NMR (CDCl$_3$, 400 MHz) δ: 7.36-7.32 (m, 4H, *aromatic*), 7.31-7.25 (m, 1H, *aromatic*), 4.50 (s, 2H, CH$_2$OC**H**$_2$C$_6$H$_5$), 3.46 (t, 2H, J = 6.7Hz), 3.40 (t, J = 6.9Hz, 2H), 1.89-1.80 (m, 2H) 1.66-1.57 (m, 2H), 1.48-1.25 (m, 8H); ^{13}C NMR (CDCl$_3$, 100 MHz) δ: 138.7, 128.4, 127.6, 127.5, 72.9, 70.4, 34.0, 32.8, 29.7, 29.3, 28.7, 28.1, 26.1; IR (neat) v_{max}: 2931 (ArC-H stretch), 2854 (C-H stretch), 1103 C-O stretch), 736 (C-Br stretch cm^{-1}; MS (CI+ (NH$_3$)) *m/z* 316.3 ([M+NH$_4$]$^+$, (^{79}Br), 79%), 318.1 ([M+NH$_4$]$^+$, (^{81}Br) 100%).
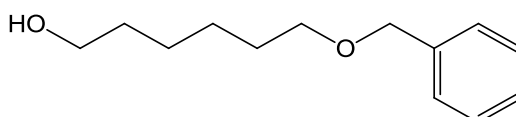
Synthesis of 6-(benzyloxy)hexan-1-ol (2.21)

To a suspension of NaH (60% dispersion in mineral oil, 0.34 g, 8.5 mmol) in dry THF (50 ml) at 0°C was added 1,6-hexanediol (1.00 g, 8.5 mmol). Benzyl bromide (1.1 ml, 8.5 mmol) was then added dropwise and the reaction allowed to warm to room temperature. After heating to reflux for approximately 12 hours the reaction was cooled, water added and the aqueous extracted with DCM. The combined organics were dried over MgSO$_4$ and the solvent removed. The residue was purified by flash column chromatography (30-50% EtOAc/Pet. Ether) to yield the title compound as a clear oil (0.80g, 45%). ^{1}H NMR (CDCl$_3$, 400 MHz) δ: 7.35-7.32 (m, 4H, *aromatic*), 7.31-7.25 (m, obs, assume 1H, *aromatic*), 4.50(s, 2H, CH$_2$OC**H**$_2$C$_6$H$_5$), 3.63 (t, J = 6.4Hz, 2H), 3.47 (t, J = 6.5Hz, 2H), 1.67-1.53 (m, 4H) 1.45-1.33 (m, obs, assume

4H); ^{13}C NMR (CDCl$_3$, 100 MHz) δ: 139.1, 128.8, 128.0, 127.9, 73.3, 70.7, 63.3, 33.1, 30.1, 26.4, 26.0; IR (neat) ν_{max}: 3267 (O-H stretch), 2976 (ArC-H stretch), 1095 (C-O stretch) cm^{-1}; MS (CI+ (NH$_3$)) *m/z* 226.3 ([M+NH$_4$]$^+$, 94%) 209.2 ([M+H]$^+$, 100%).

Preparation of (((6-bromohexyl)oxy)methyl)benzene (2.22)
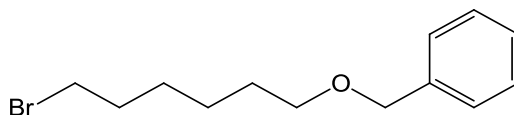
To a solution of DPPE (1.00 g, 2.40 mmol) in THF (30 ml) under N$_2$ was added dibromotetrachloroethane (1.56 g, 4.80 mmol). To the resulting white suspension was added 6-(benzyloxy)hexan-1-ol **2.21** (1.00 g, 4.80 mmol), after a short time the white solid had dissolved. The reaction was stirred overnight, after which time a white solid had precipitated. The suspension was filtered through a bed of celite and the solvent removed. The residue was purified by flash column chromatography (0-5 % EtOAc/Pet. Ether) to yield the title compound as a colourless oil (0.96 g, 64 %). ^{1}H NMR (CDCl$_3$, 400 MHz) δ: 7.38-7.26 (m, 5H, *aromatic*), 4.50 (s, 2H, CH$_2$OC***H***$_2$C$_6$H$_5$), 3.47 (t, 2H, J = 6.3Hz), 3.41 (t, J = 6.9Hz, 2H), 1.90-1.82 (m, 2H) 1.67-1.57 (m, 2H), 1.50-1.35 (m, 4H); ^{13}C NMR (CDCl$_3$, 100 MHz) δ: 139.0, 128.8, 128.1, 127.9, 73.3, 70.6, 34.3, 33.2, 30.0, 28.4, 25.8; IR (neat) ν_{max}: 2978 (ArC-H stretch), 1099 C-O stretch), 737 (C-Br stretch) cm^{-1}; MS (CI+ (NH$_3$)) *m/z* 288.3 ([M+NH$_4$]$^+$, (^{79}Br), 100%), 290.3 ([M+NH$_4$]$^+$, (^{81}Br) 98%).

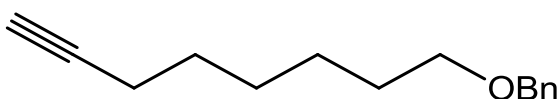## Preparation of ((oct-7-yn-1-yloxy)methyl)benzene (2.24)

n-BuLi (8.50 ml, 9.30 mmol) was added to trimethylsilylacetylene (1.30 ml, 9.30 mmol) in dry THF (50 ml) at -78°C and stirred for 30 mins. HMPA (2.20 ml, 12.40 mmol), and (((6-bromohexyl)oxy)methyl)benzene **2.22** (1.50 g, 5.50 mmol) were added and the solution allowed to warm to room temperature. NH$_4$Cl (30ml) was added and the solution extracted with hexanes (2 x 100 ml). The combined organics were dried over MgSO$_4$ and concentrated under vacuum to give a pale yellow oil. This was dissolved in MeOH (40ml), K$_2$CO$_3$ (3.00 g) added and the mixture stirred overnight. Water (30 ml) was then added and the aqueous extracted with EtO$_2$/hexanes (1:1), the combined organics were dried over MgSO$_4$ and the solvent removed *in vacuo*. Purification by flash column chromatography (50% DCM/Pet.

Ether) yielded the title compound as a clear oil (0.80 g, 67 %). ^{1}H NMR (CDCl$_3$, 400 MHz) δ: 7.38-7.25 (m, 5H, *aromatic),* 4.50 (s, 2H, CH$_2$OC**H***$_2$*C$_6$H$_5$), 3.47 (t, 2H, J = 6.6Hz), 2.19 (dt, J = 2.9Hz, 7.0Hz, 2H), 1.94 (t, J = 2.7Hz, 1H, **H**CCCH2), 1.66-1.49 (m,4H) 1.46-1.33 (m, 4H); ^{13}C NMR (CDCl$_3$, 100 MHz) δ: 139.0, 128.8, 128.0, 127.9, 85.1, 73.3, 70.7, 68.6, 30.0, 29.0, 28.8, 26.1, 18.8.

Preparation of 2,7-dimethylbenzo[*lmn*][3,8]phenanthroline-1,3,6,8(2*H*,7*H*)-tetraone (3.1)[82]
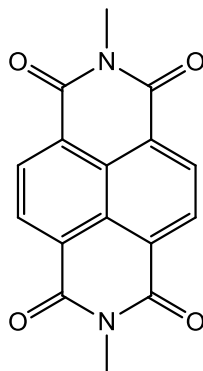
1,4,5,8-naphthalinetetracarboxylicacid dianhydride (7.50 g, 25.50 mmol) was slowly added to stirred methylamine (40% aq, 240 ml), the resulting suspension was heated at reflux for 3 hours. After cooling to room temperature, the suspension was filtered and the residue washed with methanol to yield the product as a pink powder (7.2g, 96%). ^{1}H NMR (CDCl$_3$, 400 MHz) δ: 8.83 (s, 4H, aromatic), 3.61 (s, 6H, C**H***$_3$*). ^{13}C NMR (CDCl$_3$, 100MHz) δ: 184.10, 163.50, 131.41, 126.99, 27.85 (**C**H$_3$); IR (neat) v$_{max}$: 2977 (ArC-H stretch), 1658 (s, C=O stretch) cm^{-1}.

Preparation of 2,7-dimethyl-1,2,3,6,7,8-hexahydrobenzo[*lmn*][3,8] phenanthroline (3.3)[82]
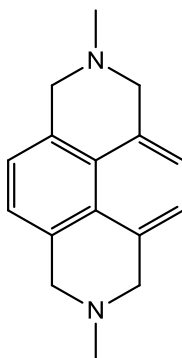
LiAlH$_4$ (3.70 g, 97.90 mmol) was added slowly to a stirred solution of AlCl$_3$ (4.30 g, 32.60 mmol) in dry THF (70 ml) under nitrogen in an ice bath. The resulting solution was allowed to warm to room temperature and 2,7-dimethylbenzo[*lmn*][3,8]phenanthroline-1,3,6,8(2*H*,7*H*)-tetraone (4.00 g, 13.60 mmol) was added portionwise so that the solution gently boiled. The resulting green suspension was heated to reflux and after a short time turned yellow. After heating at reflux for a further 4 hours it was cooled to 0°C by slowly pouring onto ice in THF. This was then left for such a time that the THF evaporated (~48 hours). The resulting solid was then washed with boiling methanol until no more colour washed out. The methanol washings were then combined and concentrated under vacuum. The precipitated product was then collected by filtration and dried under vacuum to give the title compound as a light beige solid. (2.03g, 62%). ^{1}H NMR (CDCl$_3$, 400MHz) δ: 7.13 (s, 4H, aromatic), 3.89 (s, 8H, C*H$_2$*), 2.58 (s, 6H, C*H$_3$*); ^{13}C NMR (CDCl$_3$, 100MHz) δ: 131.1, 127.1, 121.9, 58.2, 44.9; IR (neat) v$_{max}$: 2978 (C-H stretch).

Preparation of 2,7-dibenzylbenzo[*lmn*][3,8]phenanthroline-1,3,6,8(2H,7H)-tetraone (3.7)
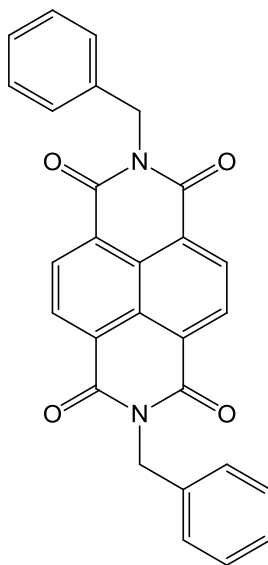
To a stirred solution of benzylamine (19.60 ml, 180.00 mmol) in water (150 ml) was slowly added 1,4,5,8-Napthalenetetracarboxylicacid dianhydride (5.00g, 18.60 mmol). The resulting suspension was refluxed for ~2 hours, cooled to room temperature and filtered under vacuum to yield the product as a pink powder, which was dried over P_2O_5 overnight (8.00 g, 96%). ^{1}H NMR (400 MHz, CDCl$_3$) δ = 8.80 (s, 4H), 7.57 (d, *J* = 3.2Hz, 4H), 7.38-7.27 (obs, assume 6H, m), 5.40 (s, 4H, C*H₂*); ^{13}C NMR (100 MHz, CDCl$_3$) δ = 162.86, 136.51, 129.17, 128.61, 127.89, 126.74, 126.68, 44.03 (*C*H₂); IR (neat) v$_{max}$: 2977 (ArC-H stretch), 1658 (s, C=O stretch) cm^{-1}; MS (CI+ (NH$_3$)) *m/z* 464 ([M+NH$_4$]$^+$, 97%;. Anal. Calcd. for $C_{28}H_{18}N_2O_4$ (446.5):C, 75.33; H,4.06 %; N; 6.27 %; Found: C, 75.48; H, 4.03 %; N, 6.32 %

Preparation of 2,7-dibenzyl-1,2,3,6,7,8-

hexahydrobenzo[*lmn*][3,8]phenanthroline (3.8)
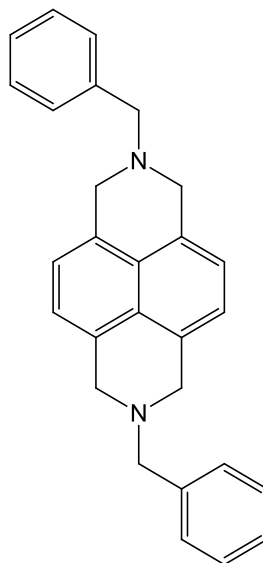
LiAlH$_4$ (3.70 g, 97.90 mmol) was added slowly to a stirred solution of anhydrous AlCl$_3$ (4.30 g, 32.60 mmol) in dry THF (50 ml) under moisture free conditions in an ice bath. The flask was then removed from the ice bath and 2,7-dibenzylbenzo[*lmn*][3,8]phenanthroline-1,3,6,8(2*H*,7*H*)-tetraone (**7**) (3.05 g, 6.80 mmol) was added in portions so that the mixture gently boiled. The resulting red suspension was heated at reflux and quickly turned green. It was then heated at reflux overnight, after which time it was cooled to room temperature and aqueous KOH (10%, 10 ml) was added very cautiously. The mixture was then stirred at room temperature for 30 mins, followed by 1 hour at reflux. The white suspension was filtered whilst hot and the residue boiled in THF for 1 hour, before filtering again. The THF extracts were combined and the solvent removed under vacuum. The residue was dissolved in DCM, dried over Na$_2$SO$_4$ and the solvent removed under vacuum. The resulting solid was triturated in methanol, then filtered and dried under vacuum to give title compound as a dark beige solid (0.583g, 22%). ^{1}H NMR (400 MHz, CDCl$_3$) δ = 7.4-7.26 (m, 10H), 7.08 (m, 4H), 3.96 (s, 8H, ring C*H$_2$*), 3.77 (s, 4H, C*H$_2$*). ^{13}C NMR (100 MHz, CDCl$_3$) δ = 131.88, 129.68, 128.77, 127.64, 122.23, 56.72. IR (neat) ν$_{max}$: 2977 (s, ArC-H stretch) cm^{-1}; MS (ES+ (MeOH)) *m/z* 391 ([M+H]$^+$, 100%).

Preparation of 2,7-bis(hydroxyhexyl)benzo[*lmn*][3,8]phenanthroline-1,3,6,8(*2H, 7H*)-tetraone (3.9)[85]
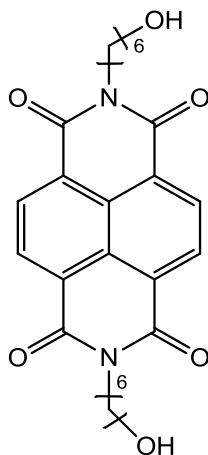
A suspension of 6-aminohexan-1-ol (0.34 g, 2.87 mmol) and triethylamine (0.2 ml) in degassed DMF (15 ml) was subjected to microwave radiation at 140°C for 15 minutes. Once cooled the precipitated product was filtered off and washed with cold DMF (10 ml). The resulting solid was dried under vacuum overnight (0.34 g, 56 %). ^{1}H NMR (400 MHz, CDCl$_3$) δ: 8.76 (s, 4H, aromatic), 4.21 (t, J = 7.5Hz, 4H), 3.65 (t, J = 6.4Hz, 4H), 1.85-1.75 (m, 4H), 1.68-1.4 (m, 12H); ^{13}C NMR (100 MHz CDCl$_3$) δ: 162.9, 131.1, 126.7, 62.8, 40.8, 32.6, 28.0, 26.7, 25.3; IR (neat) v_{max}: 3320 (O-H stretch), 2931 (s, ArC-H stretch), 1653 (C=O stretch) cm^{-1}; MS (ES+ (MeOH)) *m/z* 489 ([M+Na]$^+$, 100%); Anal. Calcd. for C$_{26}$H$_{30}$N$_2$O$_6$ (466.53):C, 66.94 %; H, 6.48 %; N; 6.00 %; Found C, 66.64 %; H, 6.48 %; N, 5.99 %.

Preparation of 2-benzyl-1*H*-benzo[*de*]isoquinoline-1,3(2*H*)-dione (3.16)
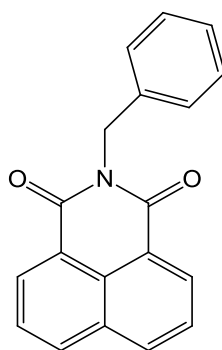
A mixture of naphthalic anhydride (1.00 g, 5.00 mmol) and benzylamine (5.50 ml, 50.00 mmol) in water (50 ml) was heated to reflux for 3 hours, after which time it was allowed to cool to room temperature and filtered under vacuum. The residue was washed with water (50 ml) and dried over P_2O_5 to yield the title compound as an off white powder (1.24 g, 86 %). M.p. 173-175°C; ^{1}H NMR (CDCl$_3$, 400 MHz) δ: 8.58 (d, J = 7.7Hz, 2H, *aromatic*), 8.16 (d, J = 8.3Hz, 2H, *aromatic*), 7.72 (t, J = 7.9Hz, 2H, aromatic), 7.55 (d, J = 7.1Hz, 2H, *aromatic*), 7.34-7.20 (m, 3H, *aromatic*), 5.38 (s, 2H, C*H*$_2$); ^{13}C NMR (CDCl$_3$, 100 MHz) δ: 164.2 (***C**=O), 137.3, 134.0, 131.6, 131.4, 129.0, 128.5, 128.1, 127.5, 127.0, 122.6, 43.6 (***C**H$_2$); IR (neat) v$_{max}$: 1693 (s, C=O st), 1651 (s, C=O) cm^{-1}; MS (CI+, (NH$_3$)) *m/z* 305 ([M+NH$_4$]$^+$, 288 ([M+H]$^+$; Anal. Calcd. for C$_{22}$H$_{34}$O$_2$S$_2$ (287.09): C, 79.43%; H, 4.56%; N, 4.88%;. Found: C, 79.52%; H, 4.59%; N, 4.85%.

Preparation of 2-benzyl-2,3-dihydro-1*H*-benzo[*de*]isoquinoline (3.17)[103]
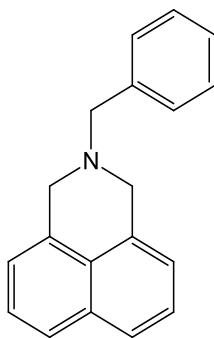
Lithium aluminium hydride (2 M in THF) (8.50 ml, 17.00 mmol) was added dropwise to a stirred solution of aluminium chloride (0.68 g, 5.10 mmol) in THF (30 ml) at -78°C. The resulting solution was allowed to warm to room temperature prior to the dropwise addition of 2-benzyl-1*H*-benzo[*de*]isoquinoline-1,3(2*H*)-dione (0.50 g, 1.70 mmol) in THF. The bright green solution was then heated to reflux for 12 hours, after which time it had turned yellow and a precipitate had formed. The mixture was allowed to cool to room temperature prior to the cautious addition of aqueous potassium hydroxide (5.00 ml, 10% by weight). After stirring for 30 mins at room temperature, the mixture was heated to reflux for 1 hour and then filtered whilst hot. The residue was heated to reflux for 1 hour with a further 40 ml of THF prior to hot filtration. The THF extracts were combined and the solvent removed *in vacuo*. The residue was purified by flash column chromatography (DCM) to yield the title compound as an off white solid (0.35 g, 80 %). M.p. 84-86°C; ^{1}H NMR (CDCl$_3$, 400 MHz) δ: 7.70 (d, J = 8.4Hz, 2H, *aromatic*), 7.44-7.27 (m, 7H, *aromatic*), 7.16 (d, J = 6.5Hz, 2H, aromatic), 4.00 (s, 4H, 2 x C*H$_2$*), 3.80 (s, 2H, C*H$_2$*); ^{13}C NMR (CDCl$_3$, 100 MHz) δ: 138.1, 133.4, 133.2, 129.3, 128.4, 128.3, 127.3, 126.1, 125.7, 122.1, 62.1, 56.6; IR (neat) ν$_{max}$: 3039 (Ar C-H stretch), 2923 (ArC-H stretch), 2846 (C-H stretch) cm^{-1}; MS (CI+, (NH$_3$)) *m/z* 260 ([M+H]$^+$;. Anal. Calcd. for C$_{19}$H$_{17}$N (259.14): C, 87.99%; H, 6.61%; N, 5.40%;. Found: C, 87.28%; H, 6.97%; N, 5.03%.

Preparation of 2,3-dihydro-1*H*-benzo[*de*]isoquinoline (3.13)[100]
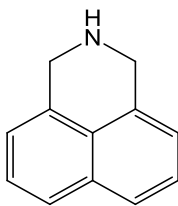
A mixture of 2-benzyl-2,3-dihydro-1*H*-benzo[*de*]isoquinoline (0.78 g, 3.00 mmol) and Pd/C (catalytic, 10% by weight) in MeOH/DCM (25 ml/25 ml) was stirred under an atmosphere of H_2 for 72 hours. The reaction mixture was filtered through a bed of celite and reduced *in vacuo* to give the title compound as a light brown solid (0.44 g, 87 %). ^{1}H NMR (CDCl$_3$, 400 MHz) δ: 7.71 (d, J = 8.3Hz, 2H, *aromatic*), 7.40 (dd, J = 7.0, 8.2Hz, 2H, CHC*H*CH), 7.18 (d, J = 7.0Hz, 2H, *aromatic*), 4.32 (s, 4H, 2 x C*H*$_2$).

Preparation of 3,3',5,5'-tetrabromo-4,4'-bipyridine (3.23)[87]
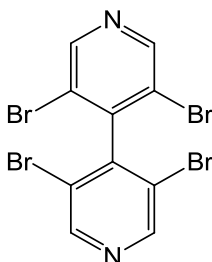
n-BuLi (3.80 ml, 5.00 mmol) was added to a solution of DIPA (0.75 ml, 5.00 mmol) in dry THF (40 ml) at -40°C under N_2. A solution of 3,5-dibromopyridine (2.37 g, 10.00 mmol) in THF (5 ml) was added and the reaction stirred for 1 hour at -40°C. The solution was cooled to -78°C prior to the addition of iodine (1.30 g, 0.50 mmol) in THF (5 ml). The resulting dark brown solution was allowed to warm to room temperature. A saturated solution of $Na_2S_2O_4$ was added until the reaction mixture was almost colourless, and the product was then extracted with EtOAc. The combined organics were dried over $MgSO_4$ and evaporated to dryness. The residue was purified by flash column chromatography (15% EtOAC/Pet. Ether 40/60) to give the title compound as an off white solid (0.91 g, 38 %). M.p. 135-138°C; ^{1}H NMR (CDCl$_3$, 400 MHz) δ: 8.82 (s, 4H) ^{13}C NMR (CDCl$_3$, 100 MHz) δ: 150.8, 146.7, 120.8; MS (ES+, (MeOH + 0.1% Formic acid)) *m/z* 469 ([M+H]$^+$, (^{79}Br), 18%); 471 ([M+H]$^+$, (^{79}Br + ^{79}Br + ^{79}Br + ^{81}Br) 23%); 473 ([M+H]$^+$, (^{79}Br + ^{79}Br + ^{81}Br + ^{81}Br), 100%); 475 ([M+H]$^+$, (^{79}Br + ^{81}Br + ^{81}Br + ^{81}Br), 23%); 477 ([M+H]$^+$, (^{81}Br) Anal. Calcd. for C$_{10}$H$_4$Br$_4$N$_2$ (467.8): C, 25.46%; H, 0.85%; N, 5.94%. Found: C, 25.75%; H, 0.91%; N, 5.97%.

Preparation of 1-(3,3',5,5'-tetrabromo-[4,4'-bypyridin]-1(4H)-yl)ethanone (3.22)
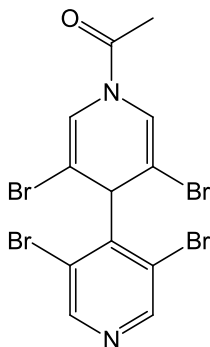

n-BuLi (0.95 ml, 1.00 mmol) was added to a solution of DIPA (0.15 ml, 1.00 mmol) in dry THF (20 ml) at -40°C under N_2. A solution of 3,5-dibromopyridine (0.48 g, 2.00 mmol) in THF (5 ml) was added and the reaction stirred for 1 hour at -40°C. The solution was cooled to -78°C prior to the addition of acetic anhydride (0.09 g, 1.00 mmol) in THF (5 ml). The resulting dark brown solution was allowed to warm to room temperature. A saturated solution of $Na_2S_2O_4$ was added until the reaction mixture was almost colourless, and the product was then extracted with EtOAc. The combined organics were dried over $MgSO_4$ and evaporated to dryness. The residue was purified by flash column chromatography (15% EtOAC/Pet. Ether) to give the title compound as an off white solid (0.21 mg, 40 %). ^{1}H NMR (CDCl$_3$, 400 MHz) δ: 8.72 (s, 1H), 8.65 (s, 1H), 7.73 (s, 1H, NC**H**), 7.08 (s, 1H, NC**H**), 5.85 (s, 1H), 2.33 (s, 3H, COC**H$_3$**); ^{13}C NMR (CDCl$_3$, 100 MHz) δ: 165.4 (**C**=O), 153.5, 151.4, 151.2, 143.1, 126.7, 125.0, 102.2, 100.4, 55.2, 21.7: IR (neat) v$_{max}$: 3093 (ArC-H stretch), 1273 (s, C-O stretch), 1697 (s, C=O) cm^{-1}; MS (ES+, (MeOH + 0.1% Formic acid)) *m/z* 513 ([M+H]$^+$, (^{79}Br), 18%); 515 ([M+H]$^+$, (^{79}Br + ^{79}Br + ^{79}Br + ^{81}Br) 74%); 517 ([M+H]$^+$, (^{79}Br + ^{79}Br + ^{81}Br + ^{81}Br), 100%); 519 ([M+H]$^+$, (^{79}Br + ^{81}Br + ^{81}Br + ^{81}Br), 65%); 521 ([M+H]$^+$, (^{81}Br), 17%).

Preparation of 3,3',5'-tribromo-[4,4'-bipyridine]-5-carbaldehyde (3.33)
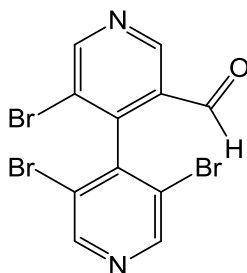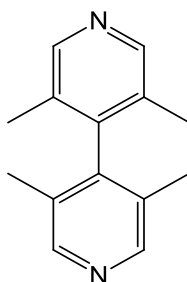

A solution of 3,3',5,5'-tetrabromo-4,4'-bipyridine (0.10 g, 0.20 mmol) in THF (10 ml) was cooled to -78°C under N_2 prior to the addition of *t*-BuLi (0.15 ml, 0.20 mmol). The resulting orange solution was stirred for 1 hour at -78°C. After the addition of anhydrous DMF (0.15 ml, 2.00 mmol) the solution was allowed to warm to room temperature and the solvent removed under reduced pressure. The residue was dissolved in DCM (10 ml) and washed with water (10 ml). The organic phase was dried over $MgSO_4$ and the volume of the solution reduced under vacuum prior to purification by column chromatography (0-2% MeOH/DCM) to yield the title compound as a sticky white solid (0.45 g, 54 %). ^{1}H NMR (CDCl$_3$, 400 MHz) δ: 9.83 (, s, 1H, C*H*O), 9.14, (s, 1H), 9.13 (s, 1H), 8.82 (s, 2H); ^{13}C NMR (CDCl$_3$, 100 MHz) δ: 188.0 (*C*=O), 157.0 (), 151.1, 150.6, 146.4, 144.9, 128.9, 122.4, 120.6; IR (neat) v_{max}: 2977 (ArC-H stretch), 1701 (s, C=O stretch) cm^{-1}; MS (ES+, (MeOH + 0.1% Formic acid)) *m/z* 419 ([M+H]$^+$, (^{79}Br + ^{79}Br + ^{79}Br), 34%); 421 ([M+H]$^+$, (^{79}Br + ^{79}Br + ^{81}Br) 97%); 423 ([M+H]$^+$, (^{79}Br + ^{81}Br + ^{81}Br), 100%); 425 ([M+H]$^+$, (^{81}Br + ^{81}Br + ^{81}Br), 31%); 391 ([M+H-CHO]$^+$, (^{79}Br + ^{79}Br + ^{79}Br), 16%); 393 ([M+H-CHO]$^+$, (^{79}Br + ^{79}Br + ^{81}Br) 45%); 395 ([M+H-CHO]$^+$, (^{79}Br + ^{81}Br + ^{81}Br), 44%); 397 ([M+H-CHO]$^+$, (^{81}Br + ^{81}Br + ^{81}Br), 13%).

Preparation of 3,3'-dibromo-4,4'-bipyridine (3.34)[90]
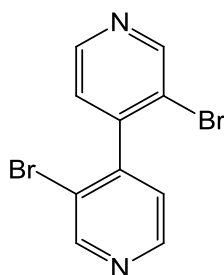
To a solution of 3,3',5,5'-tetrabromo-4,4'-bipyridine (0.52 g, 1.10 mmol) in THF (30 ml) at -78°C under N_2 was added *t*-BuLi (1.70 ml, 2.20 mmol) dropwise. The resulting yellow solution was stirred for 10mins prior to the addition of H_2O (2mL). After warming to room temperature further H_2O (10 ml) was added and the aqueous extracted with DCM (2 x 20 ml). The combined organics were dried over $MgSO_4$ and concentrated *in vacuo*. Purification by flash column chromatography (50% EtOAc/Pet. Ether) yeded the title compound as a white solid (0.20 g, 58 %). ^{1}H NMR (CDCl$_3$, 400 MHz) δ: 8.88 (s, 2H), 8.65 (d, J = 4.9 Hz, 2H), 7.19 (d, J = 4.6, 2H); ^{13}C NMR (CDCl$_3$, 100 MHz) δ: 152.8, 148.7, 147.8, 125.0, ; MS (EI+) *m/z* 312 ([M+H]$^+$, (^{79}Br + ^{79}Br), 32%); 314 ([M+H]$^+$, (^{79}Br + ^{81}Br) 68%); 316 ([M+H]$^+$, (^{81}Br + ^{81}Br), 30%); 154 ([M+H-2Br]$^+$, 100%); Anal. Calcd. for $C_{10}H_6Br_2N_2$ (313.98): C, 38.25%; H, 1.93%; N, 8.92%. Found: C, 38.55%; H,1.74%, N, 8.81%.

Preparation of 3,3',5,5'-tetramethyl-4,4'-bipyridine (3.38)[91]

To a solution of 3,3',5,5'-tetrabromo-4,4'-bipyridine (0.10 g, 0.22 mmol) in THF (20 ml) at -78°C under argon was added *t*-BuLi (1.90 ml, 2.10 mmol) dropwise. The resulting yellow solution was stirred for 10mins prior to the addition of MeI (0.26 ml, 4.20 mmol). After warming to room temperature H_2O (20 ml) was added and the aqueous extracted with DCM (2 x 20 ml). The combined orgaincs were dried over $MgSO_4$ and concentrated *in vacuo*. Purification by flash column chromatography (0-2% MeOH/DCM) yielded the title compound as a white solid (0.03 g, 67%); a minor impurity co-eluted with this compound. ^{1}H NMR (CDCl$_3$, 400 MHz) δ: 8.55 (s, 4H,

aromatic), 2.00 (s, 12H, CH_3); ^{13}C NMR (CDCl$_3$, 100 MHz) δ: 148.5, 146.2, 130.4, 16.8; MS (CI+) m/z 213 ([M+H]$^+$.

Preparation of 3,3',5,5'-tetrabromo-1,1'-dimethyl-[4,4'-bipyridine]-1,1'-diium iodide (3.24)
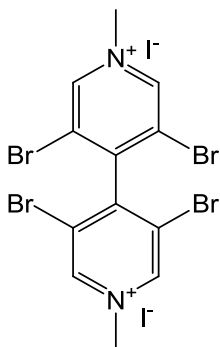
A solution of 3,3',5,5'-tetrabromo-4,4'-bipyridine (0.10 g, 0.21 mmol) and methyl iodide (5.00 ml, 80.00 mmol) in acetonitrile (10 ml) was heated to reflux for 24 hours. The resulting orange suspension was chilled in an ice bath prior to filtering under vacuum. The residue was washed with cold acetonitrile and dried under vacuum to yield the title compound as a bright orange solid (0.08 g, 49%). ^{1}H NMR (CDCl$_3$, 400 MHz) δ: 9.90 (s, 4H), 4.42 (s, 6H); ^{13}C NMR (CDCl$_3$, 100 MHz) δ: 151.6, 148.9, 121.4, 49.3.

Preparation of 3,3',5,5'-tetrachloro-4,4'-bipyridine[87]
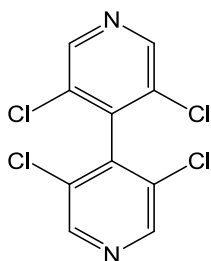
n-BuLi (1.00 ml, 1.00 mmol) was added to a stirred solution of DIPA (0.15 ml, 1.00 mmol) in dry THF (40 ml) at -40°C under N$_2$. A solution 3,5-dichloropyridine (0.30 g, 2.00 mmol) in THF (5 ml) was added and the reaction stirred for 1 hour at -40°C. The solution was cooled to -78°C prior to the addition of iodine (0.25 g, 1.00 mmol) in THF (5 ml). The resulting dark brown solution was allowed to warm to room temperature. A saturated solution of Na$_2$S$_2$O$_4$ was added until the solution became almost colourless, and the product was then extracted with EtOAc. The combined organics were dried over MgSO$_4$ and evaporated to dryness. The residue was purified by flash column chromatography (80%DCM/Pet. Ether) to give the title

compound as an off white solid (0.10 g, 34 %). M.p. 89-92°C; ^{1}H NMR (CDCl$_3$, 400 MHz) δ: 8.68 (s, 4H); ^{13}C NMR (CDCl$_3$, 100 MHz) δ: 147.9, 140.0, 131.2; MS (ES+, (MeOH + 0.1% formic acid)) *m/z* 293 ([M+H]$^+$, (^{35}Cl), 78%); 295 ([M+H]$^+$, (^{35}Cl + ^{35}Cl + ^{35}Cl + ^{37}Cl 100%); 297 ([M+H]$^+$, (^{35}Cl + ^{35}Cl + ^{37}Cl + ^{37}Cl), 40%); 299 ([M+H]$^+$, (^{35}Cl + ^{37}Cl + ^{37}Cl + ^{37}Cl, 10%); Anal. Calcd. for C$_{10}$H$_4$Cl$_4$N$_2$ (467.8): C, 40.86%; H, 1.37%; N, 9.53%. Found: C, 40.56%; H, 1.56%; N, 9.20%.

Preparation of 3,3',5,5'-tetrachloro-1,1'-dimethyl-[4,4'-bipyridine]-1,1'-diium iodide (3.25)
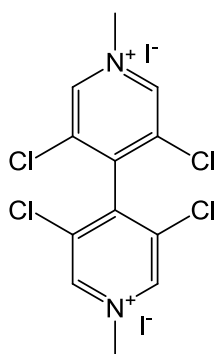
A solution of 3,3',5,5'-tetrabromo-4,4'-bipyridine (0.08 g, 0.28 mmol) and methyl iodide (5 ml, 80.00 mmol) in acetonitrile (25 ml) was heated to reflux for 24 hours. The resulting orange suspension was chilled in an ice bath prior to filtering under vacuum. The residue was washed with cold acetonitrile and dried under vacuum to yield the title compound as a bright yellow solid (0.07 g, 43 %). ^{1}H NMR (DMSO, 400 MHz) δ: 9.93 (s, 4H, *aromatic*), 4.50 (s, 6H, C*H$_3$*); ^{13}C NMR (DMSO, 100 MHz) δ: 146.8, 144.3, 132.6, 49.64.
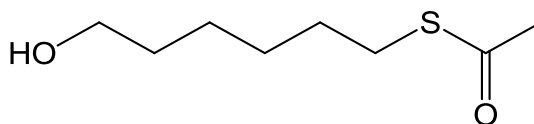
Preparation of *S*-(6-hydroxhexyl) ethanothioate (3.27)

A solution of 6-bromohexanol (1.00 g, 5.60 mmol) and potassium thioacetate (0.64 g, 5.80 mmol) in ethanol (50 ml) was heated to reflux for 4 hours, during which time a white solid precipitated. The solution was cooled to room temperature, diluted with chloroform (50 ml) and washed with water (50 ml). The organic phase was dried over MgSO$_4$ and evaporated to dryness to yield the title compound as a pale yellow oil (0.97 g, 98 %). ^{1}H NMR (CDCl$_3$, 400 MHz) δ: 3.64 (t, J = 6.7Hz, 2H, C*H$_2$*OH), 2.87 (t, J = 6.8Hz, 2H, AcS-C*H$_2$*), 2.34 (s, 3H, C*H$_3$*), 1.64-1.51 (m, 4H), 1.44-1.33 (m,

4H); ^{13}C NMR (CDCl$_3$, 100 MHz) δ: 196.1 (**C**=O), 62.9 (**C**H$_2$OH), 32.9, 30.7, 29.5, 29.0, 28.5, 25.2; IR (neat) ν$_{max}$: 3367 (s, O-H stretch), 2931, 2858, 1689 (s, C=O) cm^{-1}; MS (CI+, (NH$_3$)) *m/z* 194 ([M+NH$_4$]$^+$, 100%); 177 ([M+H]$^+$, 12%).

Preparation of *S*-(6-(tosyloxyl)hexyl) ethanethioate (3.28)
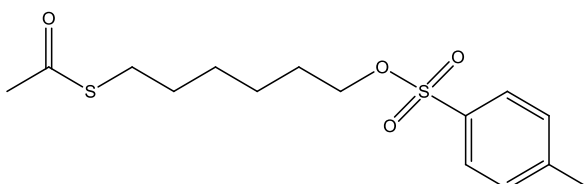
A stirred solution of *S*-(6-hydroxhexyl) ethanothioate (0.50 g, 2.80 mmol), triethylamine (0.50 ml, 3.64 mmol) and *p*-toluenesulfonyl chloride (0.70 g, 3.64 mmol) in DCM (50 ml) was heated to reflux for 4 hours under nitrogen. The resulting solution was washed with water (50 ml) and the organic phase dried over MgSO$_4$ and concentrated under vacuum. Purification by flash column chromatography (DCM, 100 %) gave the title compound as a colourless oil (0.51 g, 55 %). ^{1}H NMR (CDCl$_3$, 400 MHz) δ: 7.79 (t, J = 8.3Hz, 2H, *aromatic*), 7.35 (t, J = 8.2Hz, 2H, *aromatic*), 4.01 (t, J = 6.4Hz, 2H, C**H**$_2$-OTs), 2.82 (t, J= 7.3Hz, 2H, C**H**$_2$-SAc), 2.46 (s, 3H), 2.32 (s, 3H), 1.69-1.59 (m, 2H), 1.56-1.44 (m, 2H), 1.39-1.24 (m, 4H); ^{13}C NMR (CDCl$_3$, 100 MHz) δ: 196.0 (**C**=O), 144.7, 133.1, 129.8, 127.9, 70.4 (**C**H$_2$OTs), 30.7, 29.3, 28.9, 28.7, 28.1, 24.9, 21.7; IR (neat): 2978 (ArC-H), 1689 (C=O), 1358, 1176, 953 cm^{-1}; MS (CI+, (NH$_3$)) *m/z* 348 ([M+NH$_4$]$^+$, 100%).

6.3   STM Measurements

All experiments were performed using an Agilent 2500 or 5500 STM controller and Agilent PicoScan 5.3.3 software. STM tips were prepared from 0.25 mm gold wire (99.99%, Goodfellows), which was electrochemically etched in a 1:1 solution of HCl:Ethanol at approximately +7.0V. Commercial gold-on-glass substrates (Arrandee®) were flame annealed for several minutes prior to use. Monolayers were formed by immersing the substrate in a 1 mM solution of the molecule in DCM for 2 minutes, except in the case of BDMT where the immersion time was raised to 3 minutes. The substrate was then rinsed with ethanol and dried under nitrogen.

The STM *I*(*s*) method was used for these measurements with various set point currents, but all at a bias of + 0.6V. The measurements were made by performing

scans for 0 to +4 nm relative to the set point current, with a duration of 0.1 seconds. The resulting data was plotted in a histogram in order to determine the conductance. The S_0 calibration distance was determined using the method described in Chapter 1 of this work.

6.4   PM-IRRAS

PM-IRRAS was performed using a Bruker IFS 66v/S spectrophotometer with a Bruker PMA 37 module. A liquid nitrogen cooled Infra-red Associates Inc. mercury cadmium telluride detector, model D313/6 was used with a Hinds instrument PEM-90 photoelastic-modulator and results were corrected against a spline function.

6.5   Cyclic voltammetry

All experiments were performed on Ecochemie Autolab potentiostats (PGSTAT20 or PGSTAT30 model) using the AutoLab GPES software. The experiments employed a three electrode set up; unless otherwise stated a glassy carbon working electrode, platinum mesh counter electrode and saturated calomel reference electrode were used. The counter electrode was flame annealed prior to use. The cell was rinsed with MilliQ® water and acetone and dried with a flow of nitrogen. All solvents and electrolytes were degassed by bubbling with nitrogen for 20 mins to remove oxygen. For dry experiments the cell was dried in the oven for 12 hours prior to use. Electrolytes were made with MilliQ® water. All solvents and electrolytes were degassed by bubbling with nitrogen for 20 mins to remove oxygen.

Aqueous experiments were performed in a 10mM Na_2HPO_4/NaH_2PO_4 buffer solution, which had a pH of 6.8. Dry experiments were performed in freshly distilled DMF, which contained 0.01 M TBAHFP as the electrolyte.

The polypyrrole quasi reference electrode was prepared by modification of literature procedure.[99] The polypyrrole film was electrodeposited onto platinum wire in a solution containing 0.1 M TBAHFP and 0.01 M pyrrole in acetonitrile. SCE reference, platinum wire working and platinum mesh counter electrodes were used. The potential was swept between -0.6 and +1.1 V, at 100 mV.s^{-1}, for 50 cycles. A potential of +0.4 V was applied for ~10 s, and the electrode removed from the solution while applying the potential.

6.6   Spartan Calculations

All calculations were performed using Spartan® '08 software. The molecules required were built using construction tools within Spartan, energy minimization calculations were performed using the molecular mechanics, Merck Molecular Force Field (MMFF) level of theory.

HOMO/LUMO energies and densities were calculated using DFT; a B3LYP hybrid exchange correlation function in conjunction with 6-31G* basis set was used. The core gold orbitals were represented by pseudopotentials where necessary. All other settings were left at default.

Energy profile calculations were performed using DFT; a B3LYP hybrid exchange correlation function in conjunction with 6-31G* basis set was used. The dihedral angle was constrained to 90°; this angle was then varied by up to 270°. The energy of 50 conformations were calculated and the results plotted as relative energy *vs.* dihedral angle.

References

(1) Moore, G. E. *Electronics* **1965**, *38*.

(2) Feynman, R. P. *Engineering and Science* **1960**, *23*, 22.

(3) Aviram, A.; Ratner, M. A. *Chem. Phys. Lett.* **1974**, *29*, 277.

(4) Reed, M. A.; Zhou, C.; Muller, C. J.; Burgin, T. P.; Tour, J. M. *Science* **1997**, *278*, 252.

(5) Xiao, X. Y.; Xu, B. Q.; Tao, N. J. *Nano Lett.* **2004**, *4*, 267.

(6) Ulrich, J.; Esrail, D.; Pontius, W.; Venkataraman, L.; Millar, D.; Doerrer, L. H. *Journal of Physical Chemistry B* **2006**, *110*, 2462.

(7) Sergueev, N.; Tsetseris, L.; Varga, K.; Pantelides, S. *Physical Review B* **2010**, *82*, 4.

(8) Kim, Y.; Pietsch, T.; Erbe, A.; Belzig, W.; Scheer, E. *Nano Lett.* **2011**, *11*, 3734.

(9) Akkerman, H. B.; de Boer, B. *Journal of Physics-Condensed Matter* **2008**, *20*, 1.

(10) Nichols, R. J.; Haiss, W.; Higgins, S. J.; Leary, E.; Martin, S.; Bethell, D. *Physical Chemistry Chemical Physics* **2010**, *12*, 2801.

(11) Binnig, G.; Rohrer, H. *Helv. Phys. Acta* **1982**, *55*, 726.

(12) Landauer, R. *IBM Journal of Research and Development* **1957**, *1*, 223.

(13) Haiss, W.; van Zalinge, H.; Higgins, S. J.; Bethell, D.; Hobenreich, H.; Schiffrin, D. J.; Nichols, R. J. *Journal of the American Chemical Society* **2003**, *125*, 15294.

(14) Sedghi, G.; Sawada, K.; Esdaile, L. J.; Hoffmann, M.; Anderson, H. L.; Bethell, D.; Haiss, W.; Higgins, S. J.; Nichols, R. J. *Journal of the American Chemical Society* **2008**, *130*, 8582.

(15) Haiss, W.; Nichols, R. J.; van Zalinge, H.; Higgins, S. J.; Bethell, D.; Schiffrin, D. J. *Physical Chemistry Chemical Physics* **2004**, *6*, 4330.

(16) Xu, B. Q.; Tao, N. J. J. *Science* **2003**, *301*, 1221.

(17) Nitzan, A.; Ratner, M. A. *Science* **2003**, *300*, 1384.

(18) Simmons, J. G.; Unterkofler, G. J. *J. Appl. Phys.* **1963**, *34*, 1828.

(19) Kiziroglou, M. E.; Li, X.; Zhukov, A. A.; de Groot, R. A. J.; de Groot, C. H. *Solid-State Electronics* **2008**, *52*, 1032.

(20) Choi, S. H.; Kim, B.; Frisbie, C. D. *Science* **2008**, *320*, 1482.

(21) Beebe, J. M.; Kim, B.; Gadzuk, J. W.; Frisbie, C. D.; Kushmerick, J. G. *Phys. Rev. Lett.* **2006**, *97*, 4.

(22) Vericat, C.; Vela, M. E.; Benitez, G. A.; Gago, J. A. M.; Torrelles, X.; Salvarezza, R. C. *Journal of Physics-Condensed Matter* **2006**, *18*, R867.

(23) Nuzzo, R. G.; Allara, D. L. *Journal of the American Chemical Society* **1983**, *105*, 4481.

(24) Jin, Q.; Rodriguez, J. A.; Li, C. Z.; Darici, Y.; Tao, N. J. *Surface Science* **1999**, *425*, 101.

(25) Bencini, A.; Rajaraman, G.; Totti, F.; Tusa, M. *Superlattices and Microstructures* **2009**, *46*, 4.

(26) Noh, J.; Park, H.; Jeong, Y.; Kwon, S. *Bulletin of the Korean Chemical Society* **2006**, *27*, 403.

(27) Poirier, G. E.; Pylant, E. D. *Science* **1996**, *272*, 1145.

(28) Fenter, P.; Eberhardt, A.; Eisenberger, P. *Science* **1994**, *266*, 1216.

(29) Woodruff, D. P. *Physical Chemistry Chemical Physics* **2008**, *10*, 7211.

(30) Vericat, C.; Vela, M. E.; Benitez, G.; Carro, P.; Salvarezza, R. C. *Chem. Soc. Rev.* **2010**, *39*, 1805.

(31) Maksymovych, P.; Sorescu, D. C.; Yates, J. T. *Phys. Rev. Lett.* **2006**, *97*, 4.

(32) Kankate, L.; Turchanin, A.; Goelzhaeuser, A. *Langmuir* **2009**, *25*, 10435.

(33) Venkataraman, L.; Klare, J. E.; Tam, I. W.; Nuckolls, C.; Hybertsen, M. S.; Steigerwald, M. L. *Nano Lett.* **2006**, *6*, 458.

(34) Lortscher, E.; Cho, C. J.; Mayor, M.; Tschudy, M.; Rettner, C.; Riel, H. *ChemPhysChem* **2011**, *12*, 1677.

(35) Chen, F.; Li, X. L.; Hihath, J.; Huang, Z. F.; Tao, N. J. *Journal of the American Chemical Society* **2006**, *128*, 15874.

(36) Kim, B.; Beebe, J. M.; Jun, Y.; Zhu, X. Y.; Frisbie, C. D. *Journal of the American Chemical Society* **2006**, *128*, 4970.

(37) Cheng, Z. L.; Skouta, R.; Vazquez, H.; Widawsky, J. R.; Schneebeli, S.; Chen, W.; Hybertsen, M. S.; Breslow, R.; Venkataraman, L. *Nature Nanotechnology* **2011**, *6*, 353.

(38) Chen, W. B.; Widawsky, J. R.; Vazquez, H.; Schneebeli, S. T.; Hybertsen, M. S.; Breslow, R.; Venkataraman, L. *Journal of the American Chemical Society* **2011**, *133*, 17160.

(39) Cao, H.; Jiang, J.; Ma, J.; Luo, Y. *Journal of the American Chemical Society* **2008**, *130*, 6674.

(40) Leary, E.; Hobenreich, H.; Higgins, S. J.; van Zalinge, H.; Haiss, W.; Nichols, R. J.; Finch, C. M.; Grace, I.; Lambert, C. J.; McGrath, R.; Smerdon, J. *Phys. Rev. Lett.* **2009**, *102*, 86801.

(41) Nakashima, S.; Takahashi, Y.; Kiguchi, M. *Beilstein J. Nanotechnol.* **2011**, *2*, 755.

(42) Fuentes, N.; Martin-Lasanta, A.; de Cienfuegos, L. A.; Ribagorda, M.; Parra, A.; Cuerva, J. M. *Nanoscale* **2011**, *3*, 4003.

(43) Gittins, D. I.; Bethell, D.; Schiffrin, D. J.; Nichols, R. J. *Nature* **2000**, *408*, 67.

(44) Li, Z. H.; Pobelov, I.; Han, B.; Wandlowski, T.; Blaszczyk, A.; Mayor, M. *Nanotechnology* **2007**, *18*, 8.

(45) Li, C.; Mishchenko, A.; Pobelov, I.; Wandlowski, T. *Chimia* **2010**, *64*, 383.

(46) Pobelov, I. V.; Li, Z.; Wandlowski, T. *Journal of the American Chemical Society* **2008**, *130*, 16045.

(47) Kolivoska, V.; Gal, M.; Pospisil, L.; Valasek, M.; Hromadova, M. *Physical Chemistry Chemical Physics* **2011**, *13*, 11422.

(48) Li, Z.; Han, B.; Meszaros, G.; Pobelov, I.; Wandlowski, T.; Blaszczyk, A.; Mayor, M. *Faraday Discussions* **2006**, *131*, 121.

(49) Liu, B.; Blaszczyk, A.; Mayor, M.; Wandlowski, T. *Acs Nano* **2011**, *5*, 5662.

(50) Han, B.; Li, Z.; Wandlowski, T.; Blaszczyk, A.; Mayor, M. *Journal of Physical Chemistry C* **2007**, *111*, 13855.

(51) Haiss, W.; van Zalinge, H.; Hobenreich, H.; Bethell, D.; Schiffrin, D. J.; Higgins, S. J.; Nichols, R. J. *Langmuir* **2004**, *20*, 7694.

(52) Leary, E.; Higgins, S. J.; van Zalinge, H.; Haiss, W.; Nichols, R. J.; Nygaard, S.; Jeppesen, J. O.; Ulstrup, J. *Journal of the American Chemical Society* **2008**, *130*, 12204.

(53) Xiao, X. Y.; Nagahara, L. A.; Rawlett, A. M.; Tao, N. J. *Journal of the American Chemical Society* **2005**, *127*, 9235.

(54) Vedova-Brook, N.; Matsunaga, N.; Sohlberg, K. *Chem. Phys.* **2004**, *299*, 89.

(55) Venkataraman, L.; Park, Y. S.; Whalley, A. C.; Nuckolls, C.; Hybertsen, M. S.; Steigerwald, M. L. *Nano Lett.* **2007**, *7*, 502.

(56) Leary, E.; Higgins, S. J.; van Zalinge, H.; Haiss, W.; Nichols, R. J. *Chem. Commun.* **2007**, 3939.

(57) Fatemi, V.; Kamenetska, M.; Neaton, J. B.; Venkataraman, L. *Nano Lett.* **2011**, *11*, 1988.

(58) Venkataraman, L.; Klare, J. E.; Nuckolls, C.; Hybertsen, M. S.; Steigerwald, M. L. *Nature* **2006**, *442*, 904.

(59) Hong, W. J.; Valkenier, H.; Meszaros, G.; Manrique, D. Z.; Mishchenko, A.; Putz, A.; Garcia, P. M.; Lambert, C. J.; Hummelen, J. C.; Wandlowski, T. *Beilstein J. Nanotechnol.* **2011**, *2*, 699.

(60) Folkers, J. P.; Laibinis, P. E.; Whitesides, G. M. *Langmuir* **1992**, *8*, 1330.

(61) Ulman, A.; Eilers, J. E.; Tillman, N. *Langmuir* **1989**, *5*, 1147.

(62) Angelova, P. N.; Hinrichs, K.; Kostova, K. V.; Tsankov, D. T. *Journal of Physical Chemistry C* **2008**, *112*,17683.

(63) Bryant, M. A.; Pemberton, J. E. *Journal of the American Chemical Society* **1991**, *113*, 8284.

(64) Li, X. L.; He, J.; Hihath, J.; Xu, B. Q.; Lindsay, S. M.; Tao, N. J. *Journal of the American Chemical Society* **2006**, *128*, 2135.

(65) Engelkes, V. B.; Beebe, J. M.; Frisbie, C. D. *Journal of the American Chemical Society* **2004**, *126*, 14287.

(66) Cui, X. D.; Primak, A.; Zarate, X.; Tomfohr, J.; Sankey, O. F.; Moore, A. L.; Moore, T. A.; Gust, D.; Harris, G.; Lindsay, S. M. *Science* **2001**, *294*, 571.

(67) Wang, W. Y.; Lee, T.; Reed, M. A. *Physical Review B* **2003**, *68*, 7.

(68) Fujihira, M.; Suzuki, M.; Fujii, S.; Nishikawa, A. *Physical Chemistry Chemical Physics* **2006**, *8*, 3876.

(69) Haiss, W.; Martin, S.; Leary, E.; van Zalinge, H.; Higgins, S. J.; Bouffier, L.; Nichols, R. J. *Journal of Physical Chemistry C* **2009**, *113*, 5823.

(70) Choi, S. H.; Risko, C.; Delgado, M. C. R.; Kim, B.; Bredas, J. L.; Frisbie, C. D. *Journal of the American Chemical Society* **2010**, *132*, 4358.

(71) Schneebeli, S. T.; Kamenetska, M.; Cheng, Z. L.; Skouta, R.; Friesner, R. A.; Venkataraman, L.; Breslow, R. *Journal of the American Chemical Society* **2011**, *133*, 2136.

(72) O'Neil, I. A.; Thompson, S.; Murray, C. L.; Kalindjian, S. B. *Tetrahedron Letters* **1998**, *39*, 7787.

(73) Pollastri, M. P.; Sagal, J. F.; Chang, G. *Tetrahedron Letters* **2001**, *42*, 2459.

(74) Zhou, D.; Chen, Y. W.; Chen, L.; Li, F.; Yao, K. *Synthetic Metals* **2010**, *160*, 892.

(75) Krasinski, A.; Radic, Z.; Manetsch, R.; Raushel, J.; Taylor, P.; Sharpless, K. B.; Kolb, H. C. *Journal of the American Chemical Society* **2005**, *127*, 6686.

(76) Haiss, W.; Martin, S.; Scullion, L. E.; Bouffier, L.; Higgins, S. J.; Nichols, R. J. *Physical Chemistry Chemical Physics* **2009**, *11*, 10831.

(77) Boon, E. M.; Barton, J. K. *Current Opinion in Structural Biology* **2002**, *12*, 320.

(78) Berlin, Y. A.; Burin, A. L.; Ratner, M. A. *Journal of the American Chemical Society* **2001**, *123*, 260.

(79) Haiss, W.; van Zalinge, H.; Bethell, D.; Ulstrup, J.; Schiffrin, D. J.; Nichols, R. J. *Faraday Discussions* **2006**, *131*, 253.

(80) Quek, S. Y.; Kamenetska, M.; Steigerwald, M. L.; Choi, H. J.; Louie, S. G.; Hybertsen, M. S.; Neaton, J. B.; Venkataraman, L. *Nature Nanotechnology* **2009**, *4*, 230.

(81) Schwarzacher, W. *unpublished results.*

(82) Blake, A. J.; Baum, G.; Champness, N. R.; Chung, S. S. M.; Cooke, P. A.; Fenske, D.; Khlobystov, A. N.; Lemenovskii, D. A.; Li, W. S.; Schroder, M. *Journal of the Chemical Society-Dalton Transactions* **2000**, 4285.

(83) Sehnal, P.; Holy, P.; Tichy, M.; Zavada, J.; Cisarova, I. *Collection of Czechoslovak Chemical Communications* **2002**, *67*, 1236.

(84) Jenny, W.; Holzrich.H *Chimia* **1968**, *22*, 247.

(85) Stang, P. J.; Cao, D. H.; Saito, S.; Arif, A. M. *Journal of the American Chemical Society* **1995**, *117*, 6273.

(86) Sotiriou-Leventis, C.; Mao, Z. *J. Heterocycl. Chem.* **2000**, *37*, 1665.

(87) Cain, M.; Campos, O.; Guzman, F.; Cook, J. M. *Journal of the American Chemical Society* **1983**, *105*, 907.

(88) Mullen, K. M.; Davis, J. J.; Beer, P. D. *New J. Chem.* **2009**, *33*, 769.

(89) Aksenov, A. V.; Borovlev, I. V.; Aksenova, I. V.; Pisarenko, S. V.; Kovalev, D. A. *Tetrahedron Letters* **2008**, *49*, 707.

(90) Abboud, M.; Mamane, V.; Aubert, E.; Lecomte, C.; Fort, Y. *J. Org. Chem.* **2010**, *75*, 3224.

(91) Abboud, M.; Kadimi, A.; Mamane, V.; Aubert, E. *Acta Crystallogr. Sect. C-Cryst. Struct. Commun.* **2010**, *66*, O381.

(92) *The Chemistry of Organolithium Compounds*; Rappoport, Z., Ed.; John Wiley and Sons, 2006; Vol. 2.

(93) Durben, S.; Baumgartner, T. *Angewandte Chemie-International Edition* **2011**, *50*, 7948.

(94) Rang, A.; Engeser, M.; Maier, N. M.; Nieger, M.; Lindner, W.; Schalley, C. A. *Chemistry-a European Journal* **2008**, *14*, 3855.

(95) Makk, P.; Tomaszewski, D.; Martinek, J.; Balogh, Z.; Csonka, S.; Wawrzyniak, M.; Frei, M.; Venkataraman, L.; Halbritter, A. *ACS Nano* **2012**, *6*, 3411.

(96) Rauba, J. M. C.; Strange, M.; Thygesen, K. S. *Physical Review B* **2008**, *78*.

(97) Tada, T.; Kondo, M.; Yoshizawa, K. *J. Chem. Phys.* **2004**, *121*, 8050.

(98) Hou, S. M.; Zhang, J. X.; Li, R.; Ning, J.; Han, R. S.; Shen, Z. Y.; Zhao, X. Y.; Xue, Z. Q.; Wu, Q. *Nanotechnology* **2005**, *16*, 239.

(99) Ghilane, J.; Hapiot, P.; Bard, A. J. *Analytical Chemistry* **2006**, *78*, 6868.

(100)   Prasad, M. A.; Sangaranarayanan, M. V. *Tetrahedron* **2004**, *60*, 10967.

(101)   Amarego, W. L. F., Perrin, D. D *Elsevier* **1996**.

(102)   Burchat, A. F.; Chong, J. M.; Nielsen, N. *Journal of Organometallic Chemistry* **1997**, *542*, 281.

(103)   Zheng, S. J., Lan, J., Khan, S. I., Rubin, Y. *Journal of the American Chemical Society* **2003**, *125*, 5786.